UNIVERSITÉ CATHOLIQUE DE LOUVAIN
FACULTÉ DES SCIENCES, ÉCOLE DE GÉOGRAPHIE
EARTH AND LIFE INSTITUTE
GEORGES LEMAÎTRE CENTRE FOR EARTH AND CLIMATE RESEARCH

CONSTRAINING SPATIO-TEMPORAL SEDIMENT DYNAMICS IN LANDSLIDE-PRONE MOUNTAINOUS CATCHMENTS

From UAV-SfM-based earthflow reconstructions
to long-term catchment-scale sediment fluxes

DOCTORAL DISSERTATION PRESENTED BY

François CLAPUYT

*IN FULFILLMENT OF THE REQUIREMENTS
FOR THE DEGREE OF DOCTOR IN SCIENCES*

THESIS COMMITTEE

Prof. Veerle Vanacker (Supervisor)	Université catholique de Louvain
Prof. Kristof Van Oost (Supervisor)	Université catholique de Louvain
Prof. Marie-Laurence De Keersmaecker (Chair)	Université catholique de Louvain
Prof. Fritz Schlunegger	Universität Bern
Prof. Matthias Vanmaercke	Université de Liège
Prof. Bas van Wesemael	Université catholique de Louvain

LOUVAIN-LA-NEUVE
NOVEMBER 2018

ACKNOWLEDGEMENTS

L'idée de commencer un doctorat a tout d'abord été motivée par l'envie de devenir assistant à l'Ecole de Géographie, en apprenant que deux postes seraient vacants au département à l'issue de mes 5 ans d'études en géo. C'est suite à un appel lors du cours "Advanced Physical Geography" pour inciter les étudiants motivés à postuler, que je me suis donc décidé à envisager la voie du doctorat. Je me souviens très bien de cette entrevue avec vous, Veerle et Kristof, pour discuter de reconstruction de la topographie avec un drone, technique quasi inédite en géomorphologie à cette époque, et appliquée alors grâce à des cerfs-volants dans un article de Smith et al. (2009). Cette discussion se conclut 7 ans plus tard par la présente thèse de doctorat sur un sujet heureusement un peu plus abouti et complet à propos de la dynamique sédimentaire en milieu montagneux et l'impact des glissements de terrain sur celle-ci. A la base très fort investi dans mon métier d'assistant, je me suis petit à petit trouvé une envie de donner plus de place à mon métier de chercheur... Me voici donc à la veille d'obtenir le titre de docteur à penser à chacun et chacune, qui a contribué, de près ou de loin, à cette réussite...

Veerle, un immense merci de m'avoir fait confiance durant toutes ces années, en me laissant la liberté et l'indépendance nécessaires à ma manière de fonctionner dans mon travail, mais aussi d'avoir été présente pour me guider dans mes recherches avec des conseils toujours avisés, et d'avoir répondu à mes questions, révisé mes brouillons d'articles et de thèse... Ce fût aussi un plaisir d'être assistant pour le cours de "Tectonic Geomorphology", demandant chaque année son lot d'améliorations et de changements, pour que les étudiants se cassent la tête de manière de plus en plus exhaustive sur la géomorphologie des Ardennes et de la Campine.

Kristof, merci pour les challenging questions, et surtout pour l'aide durant les 3 jours passés à survoler le glissement du Schimbrig et à géoréférencer les points de contrôle (qui appartiennent maintenant quasi au passé...). Tu auras finalement été le seul à pouvoir comprendre réellement pourquoi survoler ces quelques hectares de montagne demandaient 15 jours de terrain! J'ai, par ailleurs, vraiment apprécié construire ce cours/TP "Advanced Geoprocessing" avec toi, c'est maintenant un réel atout dans le cursus des étudiants.

Fritz, thank you very much for sharing with us the Schimbrig area, as well as the data from your former PhD students, Fabian van den Berg, Marco Schwab and Sara Savi. Thanks to that, I spent fantastic and memorable moments in the middle of the beautiful Swiss landscapes to "play" with the drone and wander in the area. Your questions and comments were always valuable and challenging. It eventually helped me a lot to improve the chapters related to the Schimbrig earthflow. Here, I extend my thanks to Romain Delunel who helped me setting up this RTK GPS from Bern University.

I would also like to extend my acknowledgments to the other members of my thesis committee. Marie-Laurence, merci de l'avoir présidé. Matthias en Bas, dank u wel voor uw constructieve opmerkingen. Bas, merci aussi pour les traits d'humour et les randonnées à la découverte de calderas, cuevas, dolines, et autres curiosités géomorphologiques dans la région d'Almeria.

Marco, Pierre, Monique, Alice et Dominique, merci pour votre travail de l'ombre toujours efficace et précieux ! Tout roule au département, et c'est en très grande partie grâce à vous...

Merci à mes collègues de labo: Nicolas pour toutes ces années où tu m'as donné TP; Marie, pour ta bonne humeur ainsi que les discussions à propos des glissements de terrain pour mon mémoire notamment; Vincent, pour les bêtes blagues, les pommes vertes de 16h, et l'aide sur les corrections topographiques d'images Landsat; Jérôme, pour la transmission de ton expertise du labo Cosmo pour traiter les échantillons du Schimbrig, présentés dans le chapitre 4. Ta patience et ta méticulosité furent indispensables pour obtenir un blanc correct; Emilien, formellement pour les bricolages de drones et de câbles USB, et autres salons de drones, mais surtout moins formellement pour les afterworks "déjantés" ; Nathan, reconnaissance éternelle pour avoir sauvé mon chapitre 5 à 10 jours de la remise de ma thèse, mais aussi pour les discussions existentielles toujours matières à réflexion; Milu, tu buen humor y tu sonrisa han brillado siempre como un rayo de sol en los corredores del Mercator.

A tous mes collègues, avec qui j'ai, un jour, partagé un mot, une bière, ou davantage... merci pour tous ces moments inoubliables (ou oubliés, c'est selon ;-)). Toutes ces années de doctorat auraient été moins drôles et moins festives sans vous... Bien que l’ambiance soit toujours au top au fil des années (on ne se voit pas vieillir, c’est génial), mention spéciale pour les vieux de la vieille : Pierre-Yves, FoKo, Sylvain M., Antoine, Mathilde, Oli, Raphaël et Samuel.

Un grand merci à tous les étudiants qui ont "subi" mes séances de TP... Ils n'en n'ont sûrement pas conscience mais leurs questions et leur intelligence m’ont permis d'approfondir mes connaissances dans divers domaines et d'affûter mes capacités à enseigner. Source d’épanouissement, le métier d’assistant m’a réellement aidé dans l’aboutissement de ma thèse car cela m’a permis de varier les plaisirs, tout en rythmant ces 7 années de dur labeur. J’en profite d’ailleurs pour remercier toute l’équipe des assistants d’hier et d’aujourd’hui.

Isa, mon amie, la meilleure… avec qui j’aurai quasi tout fait durant ces 12 dernières années… Ces quelques lignes ne suffiront pas de te faire part de toute l'estime et la reconnaissance que j'ai pour toi. Donc simplement, merci, pour tout le temps de qualité passé en ta compagnie, pour ton soutien dans le bons comme dans les mauvais moments, pour nos discussions, ta franchise et ta sincérité.

Celia, tu es probablement la plus chouette rencontre de mes années de doctorat au département. Merci pour toutes nos discussions, les cafés (et les pâtes) de chez Fantasia (on devrait les nommer sponsor officiel), tes rires et ton soutien durant ces derniers mois. J’espère que notre amitié continuera en dehors des murs du Mercator.

Sophie, avec des hauts et des bas, notre histoire fût intimement liée à la géographie. Merci pour ton soutien indéfectible, et pour tous les moments inoubliables passés ensemble. Nous voilà tous les deux docteurs, à 4 jours d’intervalle, c’est cocasse quand même...

A tous les potes de la course d'orientation, merci pour tous ces moments partagés le dimanche, en stage ou en vacances. Thib', Benja, Nico, Margot, Gilles, SuperKantin, Elé, Bruno et les autres, la Lasko vivra encore longtemps grâce à nous!

Aux Géos de Namur, un énorme merci de m’avoir intégré dans votre groupe à votre arrivée à Louvain. Cela m’a permis de passer de nombreux moments géniaux depuis lors : soirées, voyages, réveillons, anniversaires, erasmus… J’espère qu’ils seront encore nombreux.

Et enfin, une pensée pour ma famille que je remercie pour le soutien, et sans qui mon caractère ne serait pas ce qu'il est aujourd’hui. Celui-ci s’est forgé en partie grâce à vous et il m’aura aidé, parfois subtilement, à arriver au bout de cette thèse de doctorat...

NOTICE

Parts of this thesis (2 chapters) are published in peer-reviewed journals, as indicated below:

- **Chapter II**

Clapuyt, F., Vanacker, V., Van Oost, K. (2016). Reproducibility of UAV-based earth topography reconstructions based on Structure-from-Motion algorithms. *Geomorphology*, 260, 4-15, doi:10.1016/j.geomorph.2015.05.011.

- **Chapter III**

Clapuyt, F., Vanacker, V., Schlunegger, F., Van Oost, K. (2017). Unravelling earth flow dynamics with 3-D time series derived from UAV-SfM models. *Earth Surface Dynamics*, *5*(4), 791–806, doi:10.5194/esurf-5-791-2017.

CONTENTS

LIST OF SYMBOLS AND ABBREVIATIONS

^{10}Be	Beryllium-10
2D	Two-dimension(al)
3D	Three-dimension(al)
a.s.l	Above sea level
ALS	Aerial laser scanning
CAIRN	Catchment-averaged denudation rates from cosmogenic nuclide
CPU	Central processing unit
CRN	Cosmogenic radionuclides
CSDMS	Community surface dynamics modeling system
DEM	Digital elevation model
DoD	DEM of differences
DSM	Digital surface model
DTM	Digital terrain model
EXIF	Exchangeable image file format
GCP	Ground control point
GPS	Global positioning system
GPU	Graphics processing unit
IMU	Inertial measurement unit
LGM	Last Glacial Maximum
LiDAR	Light detection and ranging
M3C2	Multiscale model to model cloud comparison
MVS	Multi-view stereopsis
RGB	Red-green-blue
RMSE	Root mean square error
RTK	Real time kinematic
SAR	Synthetic aperture radar
SfM	Structure-from-motion
SIFT	Scale invariant feature transform
SWE	Snow water equivalent
TIN	Triangulated irregular network
TLS	Terrestrial laser scanning
UAV	Unmanned aerial vehicle
UTM	Universal transverse Mercator

CHAPTER 1

INTRODUCTION

1. BACKGROUND

Landscape evolution results from complex interactions and feedbacks between tectonics, erosion and climate (e.g. Bishop, 2007; Roe, Whipple, & Fletcher, 2008). Earth's topography primarily reflects the balance between tectonics and erosion, while climate regimes subsequently control erosion intensity and processes (Figure 1.1). Convergent movements of lithospheric plates are driving plate subduction, and induce crustal thickening due to topographic load forces. The isostatic response to mass accumulation at convergence boundaries is the creation of highly elevated mountain ranges, e.g. the European Alps (Bernet et al., 2001).

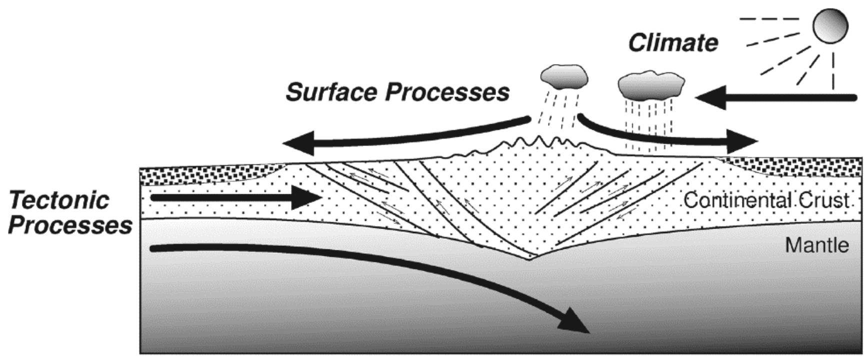

Figure 1.1: Simplified diagram depicting the processes involved in the dynamics of an active orogeny (Source: Roe et al., 2008).

In addition, the pace of tectonic rock uplift and exhumation of mass is controlled by slab load forces which can either maintain surface uplift low (Schlunegger and Kissling, 2015) or increase rock exhumation in case of slab detachment (Fox et al., 2015). In active mountain belts, tectonic uplift is often balanced by weathering and erosion processes that are limiting the elevation of peaks and ridges. Combined with biota, mechanical and chemical weathering on hillslopes primarily converts bedrock into regolith and soil particles that can be transported by gravity and water to river channels and sedimentary basins. These sedimentary particles, having a grain size from clay to boulders, subsequently serve as tools for incision into river bedrock (Riebe et al., 2015). Moreover, both the size and the flux of sediments in river channels drive channel incision (Sklar et al., 2017) which in turn, steepens adjacent hillslopes.

Models of fluvial landscape evolution often rely on the assumption that sediment transport on hillslopes scales with slope gradient (Roering et al., 1999), and that river erosion scales with the stream power or shear stress (Montgomery, 2003). However, field-based quantitative studies showed that landscape response is frequently thresholded, i.e. the mentioned relationships are not linear. Hillslopes adjust to river incision until they reach a threshold angle where hillslope erosion rate attains a critical value (e.g. Dibiase et al., 2012; Montgomery and Brandon, 2002; Ouimet et al., 2009; Vanacker et al., 2015). When the erosion rate continues to increase, hillslopes respond to further increase in base level lowering by increasing mass movement frequency. In this threshold condition, the hillslope gradients tend to be independent of the catchment-wide erosion rate (Binnie et al., 2007; DiBiase et al., 2010; Ouimet et al., 2009). Depending on the lithological setting, the reported slope threshold values usually range between 30° and 40° (e.g. Dibiase et al., 2012; Ouimet et al., 2009). Besides, topography and latitude drive large-scale climate patterns, which, in turn, control water availability for river incision and hillslope erosion, as well as glacial erosion in cold environments (e.g. Montgomery et al., 2001; Riebe et al., 2015).

Landslides as a dominant erosion process in mountainous terrain

In humid mountainous environments, river incision sets the pace of channel lowering and hillslope steepening (Whipple and Tucker, 1999). Hillslopes rapidly adjust to channel incision (e.g. Safran et al., 2005) by overland flow erosion, downslope creep of soil material, and mass wasting processes (e.g. Allen, 2009). Sediment transport by soil creep is often represented by non-linear diffusive models (Roering et al., 2001; Schlunegger et al., 2013) where the sediment flux does not increase linearly with slope gradient, which involves short adjustment time scales after changes in base level lowering or tectonic uplift rates. At regional scale, mass movements are stochastically delivering sediment to the river network (e.g. Hovius et al., 1997; Korup et al., 2004), and can profoundly influence the topographic evolution of mountainous catchments. At the hillslope scale, steepening of hillslopes adjacent to river valleys creates unstable conditions increasing mass movement probability (e.g. Roering et al., 2005). Mass movement occurrence reduces the hillslope gradient to reach a dynamic topographic steady state. At the catchment scale, mass movements primarily regulate the temporal variation in sediment production on hillslopes, and subsequently sediment delivery to the river network (e.g. Benda and Dunne, 1997).

Sediment transport by mass wasting is complex to integrate in landscape evolution models because of its stochastic behaviour and the feedbacks on hillslope adjustment and channel incision. Mass-movement related sediment accumulation in rivers has a twofold impact. (1) It might decrease sediment transport capacity and protect the river bed from further erosion (e.g. Korup et al., 2010). These transport-limited river systems are typical of environments affected by earthquakes where large volumes of sediments originating from co-seismic landslides enter the river network at once. The residence time of such landslide-derived material that is temporarily stored inside the catchments can reach thousands of years (Wang et al., 2015, 2017). Therefore, co-seismic landslides can have an influence on fluvial erosion processes on a millennial time scale. (2) The removal of mass movement material may lead to a situation where the river becomes supply-limited. This shift from transport-limited to supply-limited, is often the result of selective transport of fine sediment particles in the river channel. Once the river becomes depleted in fine sediment, that can easily be mobilised by the median river flow (Wang et al., 2015, 2017), the coarse material rich in fresh abrasive agents helps to accelerate fluvial incision (Whipple et al., 2000). The latter (abrasive effect of tools) might reinforce the supply-limited character of the channel network. The geomorphic efficiency of mass movements, i.e. their global contribution to the sediment budget of catchments, is still poorly constrained due to the variability of mass movement mechanisms and scales of sediment connectivity (e.g. Egholm et al., 2013; Hovius et al., 1997; Roering et al., 2005). In addition, the timing of sediment production and supply to the river network also needs to be spatially and temporally quantified to better constrain sediment transfer dynamics (e.g. Burt and Allison, 2010; Burtin et al., 2014; Korup et al., 2010).

Mass movements are discrete slope failures, both in space and time, which are initiated when the downslope component of the gravity force on a sediment mass exceeds the forces resisting the motion. Movement initiation occurs when (1) the gravity force increases, i.e. by mass accumulation on top of hillslopes or by slope steepening through undercutting of the foothills or tectonic uplift, when (2) the shear stress decreases, i.e. by soil weathering or by pore pressure increase (Bridge and Demicco, 2008), or when (3) earthquakes trigger strong ground motion (Meunier et al., 2007). This combination of a large number of controlling factors renders mass movement prediction complex, as they are stochastic phenomena. Mass movements or slope movements are typically classified into 5 main categories, i.e. falls, topples, slides, spreads and flows (Hungr et al., 2014; Varnes, 1978). We therefore acknowledge that strictly speaking, *landslides* encompasses only a fraction of the variety in mass wasting processes. However, for the sake of legibility and simplicity, we will use *landslide* as an all-inclusive term to name all the types of mass movements in this manuscript. When we refer to specific types of mass wasting processes, i.e. mainly *debris flow* and *earthflow,* we use the proper terms to describe them in detail.

For multi-annual landslide studies, one can construct magnitude-frequency distribution functions that characterise the number of landslides of a given magnitude that typically occur in a given period (Guzzetti et al., 2002; Hovius et al., 1997; Malamud et al., 2004). Based on regional remote-sensing landslide inventories, the inferred distribution is then modelled using either an inverse power law (Guzzetti et al., 2002; Hovius et al., 1997) or a parametric inverse-gamma (e.g. Guns and Vanacker, 2014; Malamud et al., 2004) probability distribution. In both cases, small landslides are more likely to occur than large landslides. Using the parametric inverse-gamma probability distribution, it is possible to model the exponential rollover of the distribution for small events: landslide inventories regularly highlight that the probability of medium-size landslides is greater than the one of small and large landslides.

The sediment cascade: a variety of sediment pathways from sources to sinks

Gravity and runoff water mainly control sediment production and mobilisation on hillslopes, transport to and along the river network, temporary storage, and eventually deposition. Besides, mass transfer is only possible when sediment connectivity between landscape compartments, i.e. sediment stores and sinks, is effective (Fryirs, 2013). Connectivity is physically expressed as linkages and blockages controlling sediment transfer within catchments. Three different types of linkages characterise connectivity (Figure 1.2). (1) Lateral linkages connect the channel network with the rest of landscapes, i.e. mainly hillslopes. (2) Longitudinal linkages depict the ability of the river network to transfer sediments downstream. (3) Vertical linkages mainly affect lower reaches of catchments and characterise surface-subsurface interactions of water and sediment. The variety of pathways from the primary sediment sources to the final depositional areas was initially described as the *sediment delivery problem* (Dietrich and Dunne, 1978; Walling, 1983) and the issue has been revisited with the *sediment cascade* concept (e.g. Bracken et al., 2015; Burt and Allison, 2010; Fryirs, 2013; Heckmann and Schwanghart, 2013).

Within the sediment cascade, landslides stochastically act as a major sediment source on hillslopes. They can mobilise soil and regolith material that can temporarily accumulate on the slopes and becomes available for further mobilisation and transport downstream. In configurations where hillslopes are physically linked to channels, mobilised sediments are directly available for transport in the river network (e.g. Berger et al., 2011; Sutherland et al., 2002; Wang et al., 2017). In decoupled hillslope-channel systems, sediments remain on hillslopes as landslide colluvial fans before being gradually depleted and transported to the river network by rainfall-induced and stochastic superimposed debris flows (e.g. Benda and Dunne, 1997b; Schwab et al., 2008).

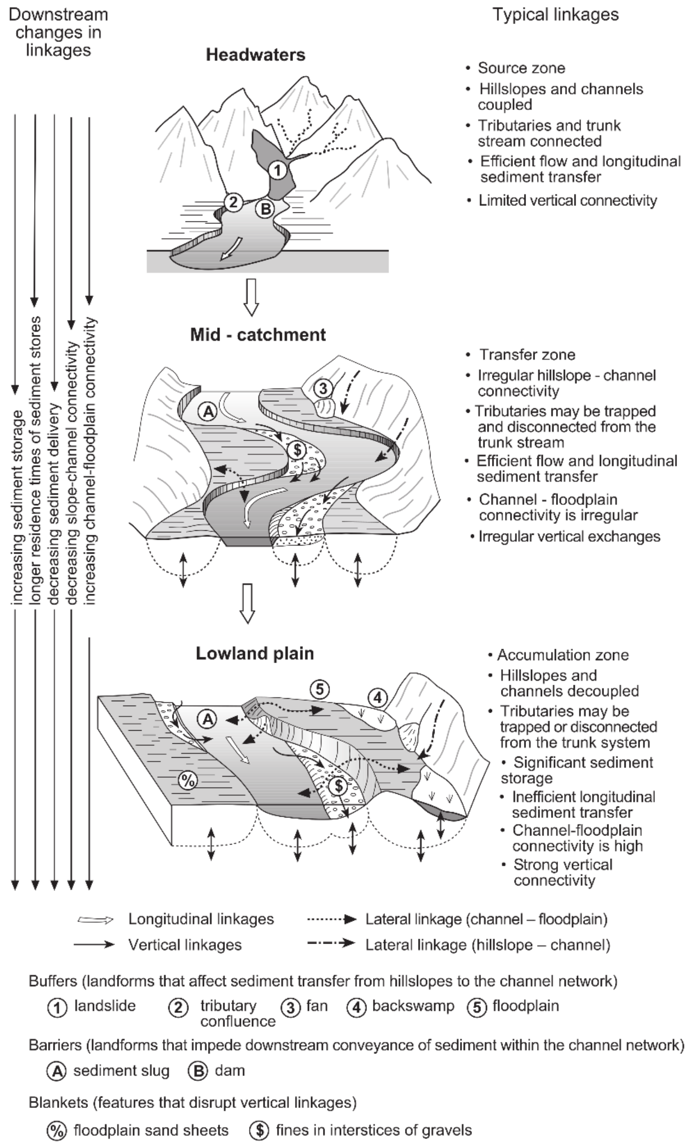

Figure 1.2: Idealized sediment cascade from sources to sinks, with longitudinal, lateral and vertical linkages between landscape compartments (Source: Fryirs, 2013).

Rainfall is a stochastic time-invariant process, which has a twofold control on mountainous environments (Benda and Dunne, 1997b; Fuller et al., 2003a; Hovius et al., 2000). On the one hand, precipitation regulates sediment supply from the hillslopes: it increases the overland flow erosion, and landslide probability as it decreases the shear stress within soil material and increases the gravity forces (Vanacker et al., 2003). On the other hand, the response of the fluvial network to enhanced sediment supply from the hillslopes depends on the discharge and river's transport capacity, i.e. its ability to transport sediments to lower reaches of the river channel. Therefore, the dual stochastic behaviour of sediment supply on the slopes and sediment transport in the river network gives the landscape a certain capacity to buffer sediment transfer within the sediment cascade (Gran and Czuba, 2017). The temporal scale of the buffering capacity can be highly variable, and vary from a number of years (e.g. Berger et al., 2011; Fuller and Marden, 2010; Sutherland et al., 2002), to decades (e.g. Bennett et al., 2013; Schwab et al., 2008), and millennia (e.g. Wang et al., 2017; West et al., 2014). The landscape response to sediment production and supply forcing is commonly assessed over one given time scale. Few studies attempted to integrate different spatial and temporal scales to assess landscape response to landslide sediment supply and transport. As such, the temporal dynamics of sediment cascades in landslide-affected alpine environments are poorly constrained (Delong et al., 2012; Kirchner et al., 2001; Mackey et al., 2009).

Quantifying pathways of the sediment cascade along with understanding the patterns and rates of these mechanisms is of crucial importance to assess long-term landscape evolution and potential feedbacks between tectonics, erosion and climate (Bishop, 2007; Burt and Allison, 2010; Fryirs, 2013; Korup et al., 2010). Furthermore, unravelling the fate of sediment production and transport in mountainous catchments can also help to constrain long-term biogeochemical cycles (e.g. Sklar et al., 2017). At the global scale, Earth's temperature is thought to be regulated by a negative feedback between atmospheric CO_2 levels, chemical weathering of silicate rocks and organic carbon burial over 10^6 years time scale (Maher and Chamberlain, 2014). In this context, rivers are seen to be important agents that are linking the biogeochemical cycles between continents, atmosphere and oceans (Aufdenkampe et al., 2011). As chemical weathering rates are not linearly related to physical erosion, the sensitivity of the climate-weathering feedback is still under debate (e.g. Gabet and Mudd, 2009; Maher and Chamberlain, 2014; Willenbring and von Blanckenburg, 2010). Recent studies have highlighted that the response of chemical weathering to climate can differ depending on the sensitivity of mountainous and low-relief areas to runoff, and it may vary depending on the distribution of erosional regimes and rock distributions (Maher and Chamberlain, 2014; Schoonejans et al., 2015). Therefore, properly constraining biogeochemical cycles eventually requires to quantify sediment source area dynamics and the impact of stochastic geomorphic events such as landslides, that are producing fresh minerals on hillslopes that becomes rapidly exposed to intense chemical weathering.

From a more applied point of view, quantifying rates of sediment propagation through the sediment cascade would also help to constrain rates of sediment retention behind dams along mountainous river courses. Indeed, their impact on the longitudinal connectivity of the sediment cascade is important, and often underestimated (Fryirs, 2013). As an example, only 45% of the sediments mobilised in the headwaters are exported out of the European Alps (Hinderer et al., 2013).

Bridging the different spatial and temporal scales over which geomorphic processes are typically assessed within the sediment cascade is a difficult task. Rates of geomorphic processes along with sediment connectivity are often highly variable in space and time due to their stochastic character. Moreover, landscapes that are in erosive or depositional phase over short time scales can either be at dynamic equilibrium, erosive or depositional phase at longer time scales. Consequently, upscaling discrete processes quantified over short time scales, e.g. landslides on hillslopes, will not necessarily properly depict the geomorphic system behaviour over longer time scales and spatial scales (Dietrich and Dunne, 1978; Sadler and Jerolmack, 2015; Schumm and Lichty, 1965).

Quantifying pattern and rates of the sediment cascade

Depending on the respective spatial and temporal scales of interest, various methodologies, tools and techniques are available for geomorphologists to assess erosion rates, sediment fluxes, sediment budgets, and more generally the pattern and rates of the sediment cascade (Brown et al., 2009; Passalacqua et al., 2015; Turowski and Cook, 2017).

On the one hand, surveying methods rely on repeated topographic measurements of a surface over time. Then, time series of measurements are used to quantify erosion or deposition of a given slope or catchment. These methods are applicable to monitor changes over 10^0-10^2 years. Over the last decade, recent advances in high-resolution topography representation techniques and acquisition platforms, combined with decreasing surveying costs, have led to an increasing availability of topographic datasets (Tarolli, 2014). The choice of the acquisition framework always results from the trade-off between (1) the spatial resolution needed and (2) the extent of the study area (Passalacqua et al., 2015). For repeated measurements of dynamic natural environments, e.g. landslide processes or volcanic eruptions, the following three parameters are narrowing down the possibilities of the acquisition framework: (3) the surveying cost, (4) the necessary return period for proper monitoring, and (5) the accessibility of the study area. Photogrammetry has long been used to derive digital surface models (DSM) from historical aerial photographs (e.g. Casson et al., 2003; Guns and Vanacker, 2014; Prokešová et al., 2010) and optical satellite imagery (e.g. Delacourt et al., 2004; Kääb, 2002; Stumpf et al., 2017). However, these data sources have become outdated with regard to the current standards for accurate topographic reconstructions, or became too expensive. The latter argument is mainly an obstacle for long-term monitoring of dynamic environments that requires frequent data acquisition and dense time series.

Surface deformation is now increasingly monitored using radar technology, that are synthetic aperture radar, i.e. SAR (e.g. Raucoules et al., 2013; Schlögel et al., 2015), and light detection and ranging, i.e. LiDAR (e.g. Blasone et al., 2014; Ventura et al., 2011; Wheaton et al., 2010). These techniques can be deployed on airborne and ground-based platforms (Figure 1.3) that have distinct inherent accuracies and ranges (Passalacqua et al., 2015). Moreover, in the recent years, the image-based structure-from-motion (SfM) algorithm arose as a major challenger to the other topographic techniques because of its ability to reconstruct three-dimensional (3D) surfaces at very high-resolution with standard and consumer-grade cameras (Westoby et al., 2012). Datasets can cover up to several km-wide study areas if the camera is carried by an unmanned aerial vehicle, i.e. UAV (Immerzeel et al., 2014; Lucieer et al., 2014; Rippin et al., 2015). Compared to other topographic acquisition techniques (such as SAR or LiDAR), the UAV-SfM framework is low-cost and flexible in its implementation, and particularly attractive for surveying campaigns in poorly accessible terrain (Eltner et al., 2016).

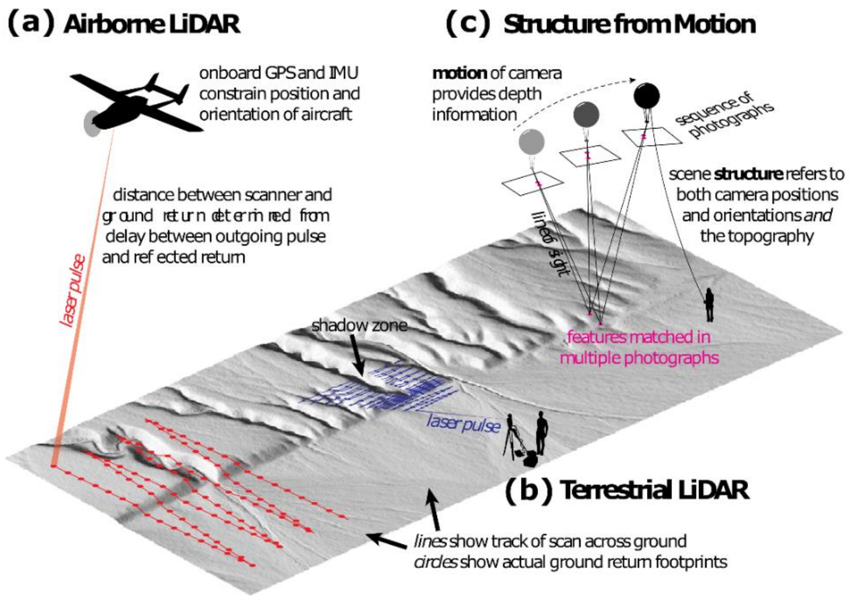

Figure 1.3: Principal high-resolution topographic techniques (Source: Johnson et al., 2014). (a) Airborne LiDAR. (b) Terrestrial LiDAR. (c) Structure-from-motion potentially combined with an UAV platform.

On the other hand, catchment-scale measurements of erosion consist of the quantification of the total volume of material that has been evacuated from the considered catchment over a given time period (Turowski and Cook, 2017). These methods usually allow covering regional to continental spatial scales, i.e. 10^1-10^4 km, over longer time scales, i.e. 10^0-10^7 years. Sediment budget at the catchment scale can be based on direct measurements of geometric changes in sediment accumulation within natural or human-made reservoirs (Bellin et al., 2011; Vanmaercke et al., 2011). Indirect measurements are based on the physical inference of geomorphic processes, i.e. sediment rating curves (Horowitz, 2003), cosmogenic radionuclides (Dunai, 2010) and thermochronology (Reiners and Brandon, 2006). Among these techniques, the quantification of terrestrial in-situ cosmogenic radionuclides (CRN) is widely used and provides catchment-averaged denudation rates over 10^3-10^6 years (e.g. Bierman and Nichols, 2004; von Blanckenburg, 2005; Gosse and Phillips, 2001). Cosmogenic nuclides are produced in target minerals, i.e. in quartz grains for ^{10}Be, at or near Earth surface. The production of such isotopes exponentially decays with depth, depending on the density of the material. Consequently, quartz grains accumulate ^{10}Be from the time sediment samples are near the surface. The isotopic clock continues to tick during erosion and transport into river streams, and only stops when burial occurs. Therefore, derived denudation rates are only representative for the integration time of samples. The faster the denudation rate, the shorter the time scale of the measure.

2. RESEARCH OBJECTIVES

Understanding the pattern and rates of the geomorphic mechanisms involved in the sediment cascade is of crucial importance to assess long-term landscape evolution, biogeochemical cycles and potential feedbacks between tectonics, erosion and climate. However, this task is difficult and poorly addressed in the literature because rates of geomorphic processes along with sediment connectivity are often highly variable in space and time due to their stochastic character.

Therefore, this PhD thesis aims to quantify geomorphic response and sediment transfer in landslide-prone mountainous environments by constraining spatio-temporal sediment dynamics from state-of-the-art geomorphic techniques: UAV-SfM derived 3D topographic reconstructions, and in-situ produced cosmogenic radionuclides. These methods were applied to a mountainous catchment in the foothills of the Central Swiss Alps to explore the spatio-temporal dynamics of sediment transfer systems and understand the processes controlling hillslope-coupling over 10^0-10^3 years. To constrain sediment fluxes, we compiled a robust database over annual, decadal and millennial time scales. At the annual scale, we assessed the sediment dynamics of an active earthflow using UAV-SfM derived very high-resolution topographic reconstructions. This methodology is convenient to perform monitoring of highly dynamic environments, such as landslides in mountainous environments, because of its flexibility, and its low-cost and lightweight characteristics. At the millennial time scale, we quantified in-situ ^{10}Be-derived denudation rates in the catchment draining from the earthflow and in adjacent rivers. In addition, we used published data on erosion and denudation rates at the decadal, centennial and at the millennial scales, respectively from Schwab et al. (2008), Savi et al. (2013) and Van den Berg et al. (2012).

Besides the geomorphic questions related to sediment cascades in mountainous terrain, this thesis also addressed more methodological questions related to the reproducibility of UAV-SfM topographic reconstructions and the sensitivity of in-situ produced cosmogenic radionuclide concentrations to stochastic geomorphic events.

In the recent years, the UAV-SfM framework became an increasingly popular tool to capture the earth's topography at very high-resolution (i.e. centimetric). Despite a relatively large amount of papers assessing the accuracy of the technique (e.g. Smith et al., 2015; Westoby et al., 2012), i.e. comparing the UAV-SfM 3D topographic reconstructions with independent topographic datasets, the reproducibility of the methodology was poorly discussed in the scientific literature. To fill this gap, we developed an experimental setup to: (1) assess the reproducibility of the UAV-SfM framework in itself, and (2) identify the parameters that influence the precision of 3D topographic reconstructions.

Landslide events have a stochastic nature, and can perturb the CRN signal in river sediments as shown by previous field-based studies (Savi et al., 2014; West et al., 2014) and numerical simulations (Niemi et al., 2005; Yanites et al., 2009). However, the impact of the stochasticity of landslides on CRN-derived denudation rates is still poorly constrained. Taking advantage of the numerical model of cosmogenic radionuclide dynamics in landslide-prone terrain by Yanites et al. (2009), we assessed the variability of CRN concentrations as a function of landslide magnitude-frequency distribution and landscape characteristics.

3. THESIS OUTLINE

The PhD dissertation is organised in six chapters (Figure 1.4), including this introduction (*Chapter I*).

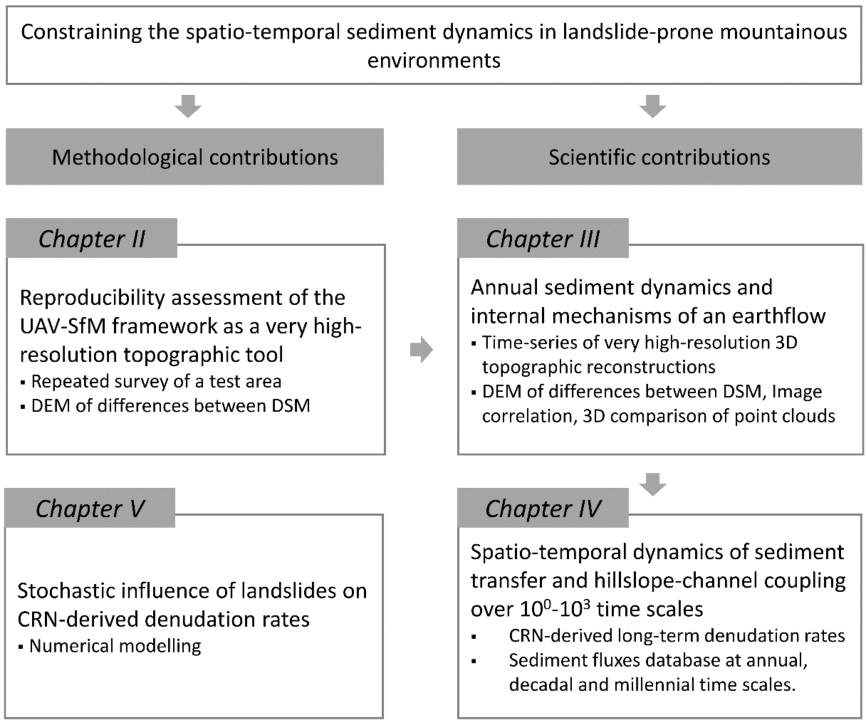

Figure 1.4: Flowchart depicting the links between the different chapters of the PhD thesis.

Chapter II focuses on the assessment of the reproducibility of earth surface topography reconstructions acquired using the UAV-SfM framework. We surveyed a study area characterised by gentle topography in the Belgian Loess belt with an UAV platform equipped with a standard reflex camera, and varied the focal length of the camera and the location of georeferencing targets between flights. We then compared the UAV-SfM digital surface models to assess the precision of the methodology, and the detection limit for topographic monitoring.

Chapter III consists in the application of the UAV-SfM framework on a very dynamic environment. Between October 2013 and October 2015, we acquired very high-resolution topographic datasets of the Schimbrig earthflow, located in the foothills of the Central Swiss Alps. A comprehensive 3D analysis of the landslide was conducted by combining three different analyses: (1) the sediment budget of the hillslope, (2) the horizontal and (3) the 3D surface displacements. The data allowed us to highlight the complex and highly dynamic structure of the earthflow.

In *Chapter IV*, we compiled sediment fluxes for three different time scales in the Entle catchment, which includes the Schimbrig earthflow. We quantified millennial-scale sediment dynamics of the Schimbrig catchment, which acts as a sediment source in the landscape. Then, we included annual data from *Chapter III*, and data from published researches on the same study area, i.e. additional data from long-term denudation rates and from classic photogrammetry at the decadal scale.

Chapter V explores the variability of CRN dynamics due to the stochastic behaviour of landslides using a two-dimensional (2D) numerical model. We iterated the stochastic model to assess the variability of final CRN concentrations and resulting erosion rates.

Finally, *Chapter VI* summarizes findings presented in this PhD dissertation and opens perspectives for further research.

CHAPTER 2

REPRODUCIBILITY OF UAV-BASED EARTH TOPOGRAPHY RECONSTRUCTIONS BASED ON STRUCTURE-FROM-MOTION ALGORITHMS

Based on:

Clapuyt, F., Vanacker, V., Van Oost, K. (2016), Reproducibility of UAV-based earth topography reconstructions based on Structure-from-Motion algorithms, Geomorphology, 260, 4-15, doi:10.1016/j.geomorph.2015.05.011.

ABSTRACT

Combination of unmanned aerial vehicle (UAV) based aerial pictures and structure-from-motion (SfM) algorithm provides an efficient, low-cost and rapid framework for remote sensing and monitoring of dynamic natural environments. This methodology is particularly suitable for repeated topographic surveys in remote or poorly accessible areas. However, temporal analysis of landform topography requires high accuracy of measurements and reproducibility of the methodology as differencing of digital surface models leads to error propagation. In order to assess the repeatability of the SfM technique, we surveyed a study area characterised by gentle topography with an UAV platform equipped with a standard reflex camera, and varied the focal length of the camera and location of georeferencing targets between flights. Comparison of different SfM-derived topography datasets shows that precision of measurements is in the order of centimetres for identical replications which highlights

the excellent performance of the SfM workflow, all parameters being equal. The precision is one order of magnitude higher for three-dimensional (3D) topographic reconstructions involving independent sets of ground control points, which results from the fact that the accuracy of the localisation of ground control points strongly propagates into final results.

1. INTRODUCTION

For the study of landslides or the monitoring of dynamic fluvial environments, an accurate and high-resolution representation of the earth surface is required. For these geomorphic applications, topographic surveys are typically conducted using a real-time kinematic (RTK) global positioning system (GPS; e.g. Brasington et al., 2000; Squarzoni et al., 2005), total stations (e.g. Fuller et al., 2003; Moss et al., 1999), terrestrial laser scanning (TLS; e.g. Brasington et al., 2012; Travelletti et al., 2008) and aerial laser scanning (ALS; e.g. Dewitte et al., 2008; McKean and Roering, 2004; Notebaert et al., 2009). While these acquisition techniques are increasingly used in geomorphology and result in rich observational datasets, they are often time-consuming and costly. Recent developments in image processing, with the application of computer vision algorithms as *structure-from-motion* (SfM), and the availability of reliable, low-cost and lightweight unmanned aerial vehicles (UAV), permit to overcome some of these drawbacks (e.g. Neitzel and Klonowski, 2011; Snavely et al., 2008).

During the last years, exploratory research has shown that UAV-based image acquisition is suitable for environmental remote sensing and monitoring (e.g. Bendig et al., 2013; Dandois and Ellis, 2010; Hugenholtz et al., 2013; Mancini et al., 2013; Westoby et al., 2012). Image acquisition with consumer grade cameras mounted on an UAV can be performed at very high spatial resolution (centimetre) and high temporal frequency in the most dynamic environments (D'Oleire-Oltmanns et al., 2012; Gomez, 2014; Immerzeel et al., 2014; James and Robson, 2012; Lucieer et al., 2014). Besides, the SfM technique allows reconstructing landform topography based on an unoriented set of pictures (i.e. without spatial orientation or georeferencing information) and taken with consumer grade uncalibrated cameras without having prior information on the location of the principal point, radial distortion, focal length or distance to the surveyed topography. Initially developed for building architecture and three-dimensional (3D) representations of objects, computer vision SfM algorithms aim to reconstruct simultaneously camera positions and orientations, as well as a 3D scene structure from a set of feature correspondences derived from overlapping pictures (Snavely et al., 2008). Scene structure is rendered as a 3D sparse point cloud generated in an arbitrary coordinate system, lacking spatial scale and orientation. This cloud is then projected in a real-world coordinate system using ground control points (GCPs) that are visible in the point cloud and were surveyed with a GPS in the field. To this end, a seven-parameter Helmert transformation, with a single factor of scale, three factors of translation and three of rotation, is computed based on the GCP coordinates in both arbitrary and real-world coordinate systems. Then, this similarity transformation is applied to the entire set of 3D point arbitrary coordinates in order to have a properly georeferenced output (Dandois and Ellis, 2010). Based on the sparse point cloud and camera parameters, densification of output can then be performed with a multi-view stereopsis (MVS) algorithm following a match, expand and filter procedure (Furukawa and Ponce, 2010).

Recently, the combination of image acquisition with UAVs and SfM-based topography reconstruction has been successfully applied on a broad range of landforms and landscapes (Table 2.1). The accuracy assessment has commonly been carried out by comparing the output with other very high-resolution acquisition techniques. Westoby et al. (2012) mapped an 80 m high coastal cliff and assessed the accuracy of the resulting digital surface model (DSM) using a terrestrial laser scanner. This study reported an overall absolute accuracy of less than 0.5 m for 86% of the area. James and Robson (2012) monitored a 3 m high coastal cliff over a year. A time series of seven topographic representations allowed them to derive erosion rates. Comparison of SfM- with TLS-derived data indicated that the root mean square error (RMSE) is about 0.07 m. Based on a similar comparison of datasets from an inaccessible wave-cut bench, Obanawa et al. (2014) obtained a maximum deviation of 0.1 m. Fonstad et al. (2013) surveyed a floodplain system and compared the SfM-derived output with ALS data for accuracy assessment. The mean difference between both topographic reconstructions was about 0.6 m. Tonkin et al. (2014) surveyed a formerly-glaciated cirque and assessed the accuracy of the UAV-SfM dataset based on points measured with a total station. They obtained a vertical RMSE of 0.52 m for the entire study area and a vertical RMSE of 0.2 m for less densely vegetated areas.

Turner et al. (2012) compared direct georeferencing of a point cloud, based on camera positions recorded by the internal GPS of the UAV, and a GCP extraction technique.

Table 2.1: Summary of accuracy assessments conducted in various published studies.

Authors	Reference dataset	Method	Accuracy	Georeferencing
Westoby et al., 2012	TLS data	DEM of difference	86% of the area between -0.5 and 0.5 m	Manual
James and Robson, 2012	TLS data	DEM of difference	Vertical RMSE of 0.07 m	Manual
Obanawa et al., 2014	TLS data	Not defined	Maximum deviation of 0.1 m	Not defined
Fonstad et al., 2013	ALS data	DEM of difference	Mean difference of 0.6 m	Manual
Tonkin et al., 2014	GCPs surveyed with total station (millimetre accuracy)	Discrete set of validation points	Vertical RMSE of 0.52 m	Manual
Turner et al., 2012	GCPs surveyed with dGPS (centimetre relative accuracy)	Discrete set of validation points	Mean absolute horizontal accuracy of 0.10 and 0.13 m	Direct georeferencing
Turner et al., 2012	GCPs surveyed with dGPS (centimetre relative accuracy)	Discrete set of validation points	Mean absolute horizontal accuracy of 0.66 and 1.25 m	GCP extraction
Harwin and Lucieer, 2012	GCPs surveyed with dGPS (centimetre relative accuracy)	Discrete set of validation points	Horizontal RMSE of 0.001 to 0.083 m Vertical RMSE of 0.04 to 0.06 m	GCP extraction
Ouédraogo et al., 2014	RTK GPS (centimetre accuracy)	DEM of difference	Mean absolute difference of 0.074 m	GCP extraction

Based on a discrete set of validation points, they assessed the horizontal accuracy of the generated ortho-mosaics and showed that the GCP technique is 5 to 10 times more accurate, even in absolute terms, than direct georeferencing, with accuracies of resp. 0.10 m to 0.13 m for the GCP technique compared to 0.66 m to 1.25 m for direct georeferencing. Harwin and Lucieer (2012) suggested that the combination of UAV and SfM could detect sub-decimetre absolute changes. In addition to nadir pictures, they also included oblique views in the SfM algorithm. By comparing the coordinates of GCPs in the georeferenced point cloud of a coastal estuary they reported horizontal accuracies of 0.001 to 0.083 m and elevation accuracy of 0.04 to 0.06 m. Lucieer et al. (2014) showed the use of orthomosaics and digital elevation model (DEM) derived from SfM and UAV to quantify relative landslide surface displacements. Ouédraogo et al. (2014) showed that accuracy of 3D topographic representations also depends on the software used to run the SfM algorithm, by comparing outputs with reference RTK GPS data where absolute mean differences are up to 0.1 m.

Either based on classic topographic surveys, i.e. RTK GPS, TLS or light detection and ranging (LiDAR), or on more recent image processing techniques, i.e. SfM reconstruction, very high-resolution DSMs can be used to quantify temporal changes in earth surface topography, based on differencing of DSMs taken at various moments in time. However, it is important to have both an accurate topographic representation and consistency between measurements over time, as DSM differencing automatically leads to error propagation (Wheaton et al., 2010). Previous studies explored workflows to produce 3D point clouds based on aerial photos taken by UAVs and assessed the accuracy for single topographic representations based either on discrete set of validation points or on independent digital terrain models (DTM). These studies showed that accuracies, i.e. the difference between measurements and ground truth, obtained with the SfM technique are in the same order of magnitude as those obtained with more traditional high-resolution topographic survey methods. However, the reproducibility of topographic measurements based on SfM algorithm, i.e. the repeatability of measurements, is poorly documented in the literature.

This paper specifically aims to assess the reproducibility of repeated reconstructions of earth surface topography using the SfM technique based on aerial photographs taken by an UAV. In the context of quantification of topographic changes over time, it is mandatory to account for errors that are inherent to the technology used to reconstruct surface topography at each time step. Spatial errors propagate when differences of DSMs (a so-called DEM of differences, DoD) are computed to quantify topographic change. In order to isolate and quantify the error that is associated with the topographic reconstructions, we repeatedly surveyed a test area which has not experienced topographic changes. Hence, the error associated with our UAV-SfM workflow will set the lower limit of detectable topographic changes for monitoring of dynamic environments.

While the quantification of the precision of measurements in itself is important, we also focus on parameters which can potentially affect the reproducibility such as the focal length of the camera and location of georeferencing targets. The focal length determines the resolution of the ground pixels for a given flight altitude. Other parameters being equal, a smaller focal length allows a wider viewing angle, i.e. larger surveyed areas during one flight, but results in coarser image resolution. The location and spatial structure of the GCPs is also a parameter of interest; as this is likely to vary between repeated surveys because of changes in topography. Here, we compare 10 digital surface models for one study area with gentle topography. Six DSMs are derived from independent datasets of aerial pictures taken from an UAV with different experimental parameters. Four DSMs are derived from one set of aerial pictures and georeferenced based on four different patterns of GCPs.

2. METHOD

2.1. STUDY AREA

The study area (Figure 2.1) is located in the Belgian Loess belt, about 40 km south of Brussels. Its centre is located at 52°32’30”N / 4°41’09”E. The study area is covered by pasture and arable fields. The altitude of the study area ranges between 125 m and 140 m a.s.l. and topography is characterised by gentle slopes up to 30° (mean slope: 5°). LiDAR topography is available for this area. This dataset was acquired by the regional public institution, i.e. the *Service Publique de Wallonie*, between 2000 and 2002 along waterways. Raw acquisition had an initial density of points of 5 to 8 points per square metre while the final product was delivered as a raster surface resampled at 1 m of resolution. The mean absolute altimetric accuracy of this dataset has been assessed to 0.11 m (Service Publique de Wallonie, 2004).

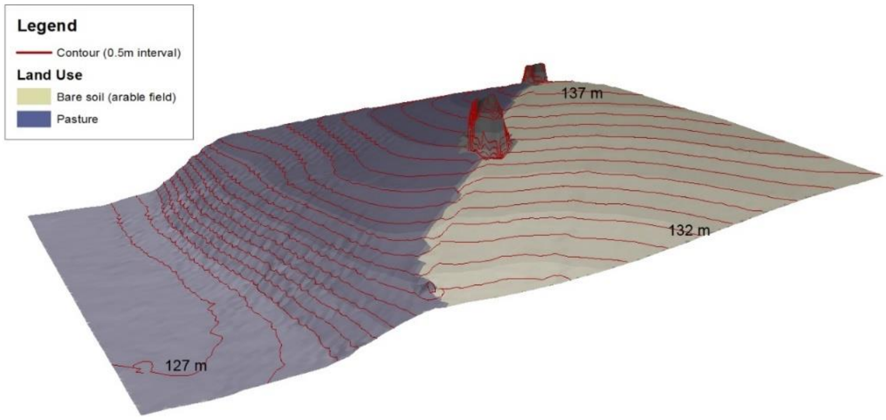

Figure 2.1: 3D view of the study area (Spatial extent: approx. 1 ha).

2.2. IMAGE ACQUISITION

The UAV platform used is a Mikrokopter Oktokopter XL, equipped with a stabilized camera mount. The maximal payload is about 1.5 kg with an associated autonomy of 5 to 6 min for a single battery. The Oktokopter has an on-board navigation system composed of an inertial measurement unit (IMU), i.e. the Mikrokopter FlightCtrl ME 2.1, and a low-cost global positioning system (GPS) receiver, i.e. u-blox LEA 6S which has an accuracy of 2.5 m (U-blox AG, 2012). This setup allows autonomous flights through predefined waypoints, after manual take-off and landing. To acquire the aerial images, we used a standard small format reflex camera (Canon EOS 550D) and two different fixed-focal-length lenses: a low-cost and lightweight Canon EF 50 mm f/1.8 II, i.e. *F50*, and a wide-angle Canon EF 28 mm f/2.8 IS USM equipped with an optical image stabilizer and a high-speed autofocus motorisation, i.e. *F28*. Both lenses were calibrated with the help of the lens calibration software Agisoft Lens. The parameters were then used to constrain the bundle adjustment with a fixed camera model in the SfM algorithm (see below). The camera is mounted on a two-axis gimbal which compensates tilt and roll movements of the UAV, in order to maintain the nadir orientation of the camera. In order to obtain sharp pictures in usual photogrammetry, camera parameters should be set to maximize depth of field by minimizing lens aperture, i.e. using the aperture priority mode, the shutter speed being automatically defined to obtain well-exposed pictures. However, in UAV-based photogrammetry, due to movements and vibrations of the UAV-platform, images should be acquired at a predefined high shutter speed (shutter priority mode) depending on the light conditions, i.e. quicker than 1/1600 s, in order to avoid motion blur, the aperture being automatically set by the camera. Besides, the ISO parameter is also dependent on light conditions during flights and typically set as low as possible to avoid a grainy texture on the pictures, i.e. ISO 100 to 400. The acquisition frequency is predefined directly within the camera setup at 1 Hz, i.e. one image per second, in order to have high redundancy needed for good performance of the SfM algorithm. In practice, the time interval between two images is slightly longer because of the intrinsic image acquisition capacity of the camera, and depends on the autofocus rapidity and time necessary to write picture files on the memory card. However, overlap between successive pictures is still sufficient due to the low UAV flight speed of ca. 2 m s^{-1}. The latter is slightly slower for flights with the 50 mm lens than with the 28 mm lens because of the smaller ground coverage of the pictures taken with the 50 mm lens (Table 2.2).

Table 2.2: Picture characteristics for 50 m of altitude flights.

Focal (mm)	Resolution (mm)	Length Image Ground (m)	Width Image Ground (m)	Distance between two flight lines (m)
28	7.70	39.82	26.61	13.27
50	4.31	22.30	14.90	7.43

The experimental setup was designed to assess the reproducibility of 3D topography reconstructions based on UAV and SfM algorithm, with varying focal length and georeferencing target locations (Figure 2.2). For each focal length, i.e. *F28* and *F50*, a flight plan was determined to survey 1 ha at a constant flight altitude of 50 m above ground level of take-off location. Each flight plan ensures that there is sufficient overlapping (66%) between pictures of adjacent flight lines (Table 2.2; Figure 2.3a).

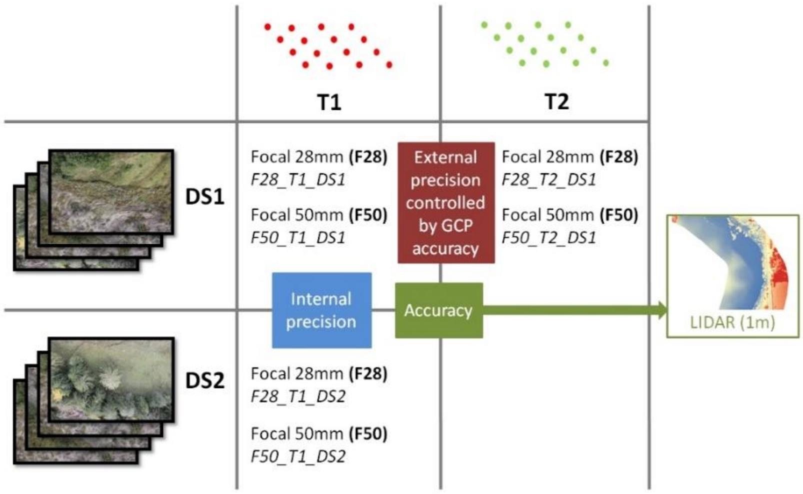

Figure 2.2: Parameters of derived SfM datasets. Accuracy is assessed by comparing each SfM dataset with LiDAR data. Internal precision is quantified by comparing identical replications, i.e. with two different aerial pictures datasets, DS1 and DS2, with the same GCP set *T1*. External precision on georeferencing is computed by comparing replications with independent GCP sets (same amount and pattern), i.e. *T1* and *T2*.

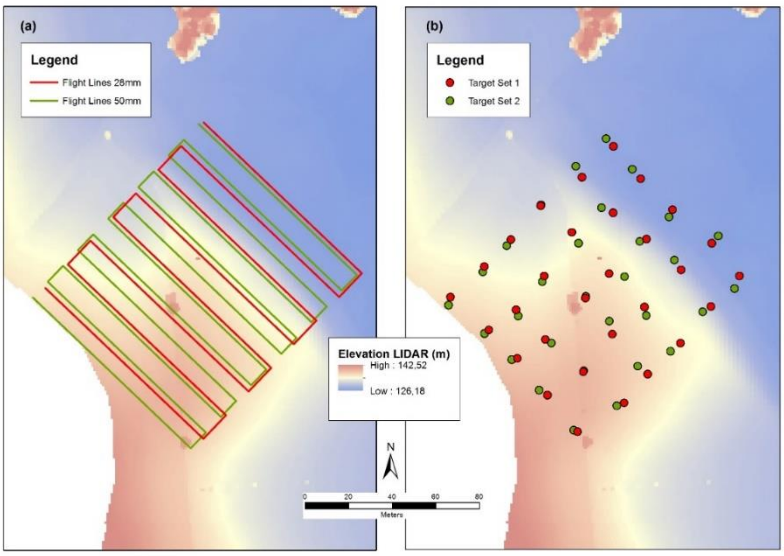

Figure 2.3: (a) Flight lines for each focal length at 50 m of altitude. (b) Locations of georeferencing targets for both sets.

Thirty georeferencing targets were scattered regularly every 20 m over the area. Each target consists of a 30 cm side white square that contrasts sharply with surrounding features and that allows automatic detection based on red-green-blue (RGB) values. Each flight plan was performed three times: two repetitions, i.e. *DS1* and *DS2*, with the same set of georeferencing targets, i.e. set *T1*, and one repetition, i.e. *DS1*, with a second set of target locations, i.e. set *T2*. Figure 2.3b depicts both sets of georeferencing targets. From this experimental setup, six independent datasets of pictures are constructed (Table 2.3).

Table 2.3: Characteristics of datasets resulting from the experimental setup.

Dataset	Focal Length (mm)	Target Set	Number of pictures	Number of points	Targets detected for georeferencing	Area (m^2)	Average density of points m^{-2}
F28_T1_DS1	28	1	288	368782	29	18882	19.53
F28_T1_DS2	28	1	291	360825	28	18847	19.14
F28_T2_DS1	28	2	352	378299	24	17448	21.68
F50_T1_DS1	50	1	643	767831	27	16452	46.67
F50_T1_DS2	50	1	454	546509	18	11702	46.70
F50_T2_DS1	50	2	597	738821	27	16073	45.97

Table 2.4: Summary of GCP differential correction.

Target Set	T1	T2
Number of targets	30	30
Correction method	Code-corrected	Code-corrected
Solution type	Float	Float
Minimum vertical precision (m)	0.500	0.600
Mean vertical precision (m)	0.520	0.613
Maximum vertical precision (m)	0.700	0.700
Minimum horizontal precision (m)	0.400	0.600
Mean horizontal precision (m)	0.463	0.610
Maximum horizontal precision (m)	0.700	0.700

Dataset names explicitly mention parameters used, e.g. *F28_T1_DS1* or *F50_T2_DS1*. Georeferencing targets, i.e. ground control points, are surveyed with a

GPS receiver, the Trimble GeoXT handheld from Geoexplorer 2008 Series, which provides sub-metre accuracy after post-processing differential correction (Table 2.4). Finally, each picture dataset was processed following the steps described below.

2.3. STRUCTURE-FROM-MOTION ALGORITHM

To derive 3D point clouds from a set of unoriented overlapping pictures, the structure-from-motion algorithm is composed of three basic steps: keypoint detection, image matching and bundle adjustment, implemented in a fully-automated free software named VisualSFM (Wu, 2011; Wu et al., 2011). The first step is the extraction of distinctive features from images that are invariant to image scale and rotation and partially invariant to change in illumination and 3D camera viewpoint, using the scale invariant feature transform (SIFT) algorithm (Lowe, 2004). A database of keypoint features is then created for each image, containing the keypoint descriptors, i.e. localisation, orientation and scale. The SIFT algorithm is implemented in SiftGPU, a component of VisualSFM, which efficiently combines the use of the graphics processing unit (GPU) and central processing unit (CPU) of the computer to increase processing time (Wu, 2007). Based on keypoint features detected on each image, the second step is the keypoint feature matching for each pair of images in the dataset (Snavely et al., 2008), including a pre-emptive feature matching reducing time processing (Wu, 2013). In addition to the pre-emptive feature matching, image matching is only performed on pairs of images that potentially have common keypoint features, i.e. images which overlap. Pairs are determined by geotagging aerial photos based on the GPS camera points recorded during flights and exchangeable image file format (EXIF) data. The procedure then selects images that are within a given radius, which is defined based on the ground coverage of the image and depends on flight altitude and focal length.

The third step of the SfM algorithm is the incremental bundle adjustment (Snavely et al., 2008; Wu, 2013) which permits the reconstruction in 3D of locations of keypoint features and camera parameters, i.e. interior orientation (focal length, principal point and pixel size) and exterior orientation (translation and rotation) parameters. In photogrammetry, bundle adjustment is the process of simultaneously refining 3D point coordinates based on two-dimensional (2D) coordinates of points from different viewpoints. This optimisation of parameters is done by minimizing the re-projection error between the location of keypoints on the image and their predicted position, which can be expressed as a non-linear least square problem (Snavely et al., 2008). Instead of simultaneously computing all parameters for the entire point cloud at once, which could lead to poor optimisation for large scale 3D representations, the SfM algorithm implemented in VisualSFM has an incremental approach. First, the estimation of parameters is done based on the pair of images which has the largest number of keypoint feature matches. Then, a third image, which shares the largest number of matches with the 3D points, is included in the optimisation. This incremental addition of pictures continues until any picture can be added to model. The output of the bundle adjustment is a 3D sparse point cloud of keypoint features in an arbitrary coordinate system, with associated RGB values for each point.

2.4. GEOREFERENCING AND DSM PRODUCTION

Point cloud georeferencing can be achieved either by direct georeferencing, i.e. using camera locations to geotag images, or by GCP extraction from the point cloud. Turner et al. (2012) showed that GCP extraction method provides a better accuracy of the output compared to direct georeferencing. Furthermore, direct georeferencing is not suitable in this study because of the relatively low quality of the Oktokopter on-board GPS receiver (reported accuracy range: 2.5 to 4 m). We therefore applied the GCP extraction method based on RGB values. As targets are white, a threshold of 250 for the three bands is set to properly detect points representing georeferencing targets (almost) without false positive points. In most cases, a cluster of points is representing a single target within the point cloud. As a consequence, the arbitrary coordinates of cluster centroids for each target were computed and matched with real-world coordinates of the targets, measured by the GPS receiver in universal transverse Mercator (UTM) coordinate system, zone 31 N (European Petroleum Survey Group geodetic parameters: EPSG:32631). This list of point pairs was then used to compute the Helmert transformation parameters, i.e. translation vector, rotation matrix and scaling factor, that are applied to the entire point cloud. Georeferencing errors associated with this transformation are computed by comparing the coordinates measured with GPS receiver and SfM coordinates of targets after georeferencing. Simple linear regression is applied, and the resulting R^2 and root mean square errors will be compared. Extractions of GCPs, computation of Helmert transformation parameters and georeferencing of point clouds were automatized using a script written in R software. Finally, each georeferenced point cloud was converted into a triangulated irregular network (TIN) and then linearly interpolated into a raster surface with a pixel resolution of 0.1 m, in order to avoid the use of complex statistical interpolation methods to transform 3D points to raster format. All raster outputs are aligned with each other.

2.5. ASSESSMENT OF ACCURACY AND PRECISION

In order to assess the absolute accuracy of the different point clouds (Figure 2.2), we compared the generated topography with the independent LiDAR dataset described previously, by calculating a DEM of differences. Mean absolute differences and RMSEs are then quantified based on the DoDs. Precision of the SfM-derived topography reconstructions can be split into internal and external precision. The internal precision evaluates the error that is associated with the SfM algorithm. As all other parameters are equal, i.e. focal length and GCP dataset, only the dataset with input pictures changes because the image acquisition with the UAV platform is repeated. Internal precision is here assessed by comparing pairs of identical replications: *F28_T1_DS1* and *F28_T1_DS2* datasets for the 28 mm focal length, *F50_T1_DS1* and *F50_T1_DS2* datasets for the 50 mm focal length. The external precision quantifies the error associated either with GCP location which is limited by the accuracy of the GPS receiver used to survey GCPs or with the quantity (and location) of ground control points used to compute the georeferencing step. To quantify the effect of ground control point location, the datasets that were taken with the same focal length but different GCP sets, i.e. *T1* and *T2*, are compared by DEM of differences. With regard to the external precision controlled by the amount of GCPs, it is quantified by comparing the output georeferenced with the entire set of GCPs with outputs georeferenced with different patterns and numbers of GCPs. The latter assessment is based on the unoriented and unscaled point cloud *F28_T1_DS1*. From it, we derived four new point clouds with different ground control point patterns and locations (Figure 2.4), which will be compared to the reference dataset *F28_T1_DS1*: (1) two point clouds are georeferenced with two different sets of 15 GCPs regularly scattered over the study area, i.e. *F28_15GCP_A* and *F28_15GCP_B*, (2) one point cloud with 9 GCPs, i.e. *F28_9GCP*, and (3) one point cloud with only 4 GCPs, i.e. *F28_4GCP*. As for accuracy, reproducibility is also assessed by a DEM of difference between the different datasets (Figure 2.2). In addition, the density of points, topographic slope and distance to nearest GCP are also calculated for each dataset in order to analyse whether accuracy and reproducibility are statistically correlated with specific variables. Spatial data manipulations were carried out in ArcGIS 10.1 while statistics and graphs were computed in R.

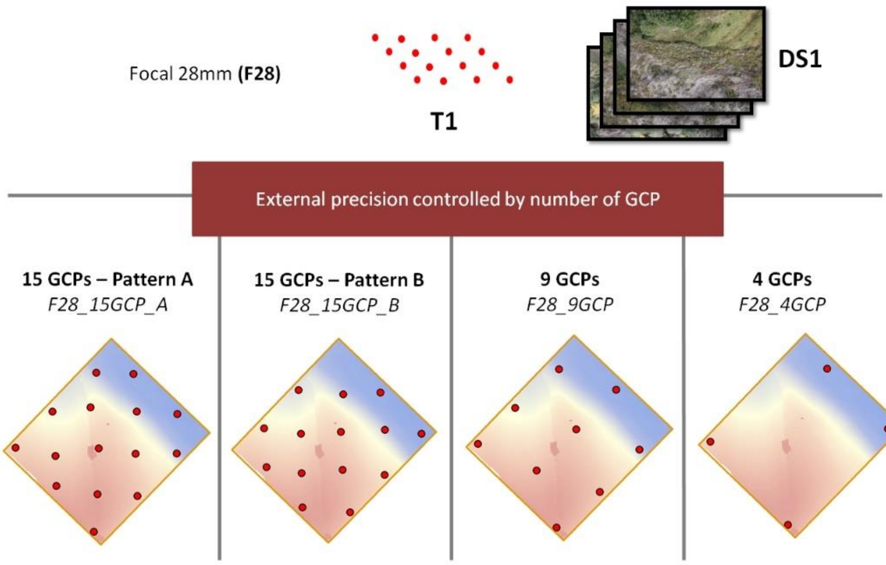

Figure 2.4: Datasets derived from the reference F28_T1_DS1 in order to assess the external precision controlled by the number of GCPs taken into account in the georeferencing step.

3. RESULTS

Six point clouds are constructed with SfM algorithm based on six independent sets of aerial pictures according to the experimental setup designed to test our hypotheses (Table 2.3). Four other DSMs are derived from one unoriented point cloud and successively georeferenced based on different patterns and numbers of GCPs.

3.1. GEOREFERENCING ASSESSMENT

Regarding the errors associated with the georeferencing of the point clouds (Table 2.5), the RMSE values are generally smaller in x and y than in z. The errors in z-values that are associated with georeferencing range between 0.22 and 0.37 m, with one outlier at 0.57 m for dataset *F50_T1_DS1*.

Table 2.5: Accuracy assessment of Helmert transformation for point clouds georeferencing.

Dataset	R^2 (GPS vs SfM)			RMSE (m)		
	x	y	z	x	y	z
F28_T1_DS1	1	1	0.990	0.156	0.109	0.323
F28_T1_DS2	1	1	0.992	0.145	0.092	0.309
F28_T2_DS1	1	0.999	0.996	0.136	0.231	0.223
F50_T1_DS1	1	1	0.973	0.151	0.142	0.570
F50_T1_DS2	1	1	0.983	0.107	0.114	0.368
F50_T2_DS1	1	0.999	0.994	0.161	0.222	0.248

These errors are mainly related to the sub-metre accuracy of the GPS receiver, where smaller errors in x and y values compared to z values are due to intrinsic lower precision of the GPS-derived altitude values. Also, not all targets are systematically detected for each point cloud, which could potentially explain a lack of accuracy in areas without targets. For each focal length, point clouds are consistent in terms of pictures taken into account in the SfM processing steps, points constituting point clouds, and average point density per square metre (Table 2.3). Only the dataset *F50_T1_DS2* has a smaller spatial extent because of an operational problem during the flight. However, it has the same point density than the other two point clouds constructed based on the 50 mm lens. A drawback of the Helmert transformation for georeferencing is that point clouds are not subjected to heterogeneous deformation or statistical interpolation. As a consequence, georeferencing errors increase proportionally with distance from georeferencing targets. For subsequent analyses of accuracy and precision of the datasets, the study area was reduced to a subarea of 1.14 ha, of which the borders extended no more than 10 m from the outermost GCPs.

3.2. ACCURACY ASSESSMENT

Comparison of DSMs derived from point clouds with LiDAR data provides an accuracy assessment of the different datasets over the entire study area (Table 2.6; Figure 2.5). The results show that the accuracy is similar for the six experimental settings that we tested. Importantly, the accuracy is of the same order of magnitude as the errors associated with georeferencing. Statistics of replications for each focal length are coherent within each other.

Table 2.6: Accuracy assessment of 3D topographic reconstructions. Summary statistics of absolute differences of elevation between LiDAR data and each point-cloud-derived DSM (metres).

Dataset	Minimum	1st Quartile	Median	Mean	3rd Quartile	Maximum
F28_T1_DS1	0	0.053	0.116	0.166	0.212	4.621
F28_T1_DS2	< 0.001	0.055	0.116	0.162	0.205	4.801
F28_T2_DS1	0	0.09	0.187	0.205	0.275	4.493
F50_T1_DS1	< 0.001	0.142	0.258	0.332	0.439	4.827
F50_T1_DS2	< 0.001	0.125	0.276	0.337	0.463	4.765
F50_T2_DS1	0	0.094	0.184	0.232	0.313	4.481

Both identical replications with a 28 mm lens and GCP set *T1* have a mean absolute difference of 0.16 m while the replication with GCP set *T2* has a mean absolute difference of 0.20 m in comparison with the LiDAR reference data. Even if the accuracies based on the mean absolute error are similar with only a difference of 0.04 m, it has to be noted that there is an offset between 3D surfaces derived from GCP set *T1* and GCP set *T2* datasets in comparison with the LiDAR reference surface. In fact, the mean difference of *F28_T1_DS1* (Figure 2.5a) and *F28_T1_DS2* (Figure 2.5b) datasets compared to LiDAR data is 0.12 m while this value is negative and equals 0.13 m for the *F28_T2_DS1* (Figure 2.5c). The accuracy of the data acquired with the 50 mm lens is lower with mean absolute differences for identical replications with *T1* that are twice as large as those obtained with the 28 mm focal length, i.e. 0.33 and 0.34 m, and 0.23 m for the replication with GCP set *T2*. Figure 2.5 also shows that elevation differences for the 28 mm lens replications are distributed more closely around the mean, as standard deviation values are lower in comparison with 50 mm lens replications. The higher accuracy of dataset *F50_T2_DS1* is coupled with a smaller standard deviation around the mean error. Spatially, the highest values of elevation differences are found where isolated trees are present, and are explained by the time interval between acquisition date of the LiDAR and the UAV-based aerial photos, during which the landowner harvested several high trees.

By analysing simple linear regressions between the LiDAR dataset and each one of the SfM-derived datasets (Figure 2.6), it becomes clear that the observations are properly spread around the line of equality, i.e. the 1:1 line, that the amount of outliers is small, and that they occur at higher elevations. The errors are mainly associated with the two isolated trees that are located at higher elevations in the study area. Importantly, root mean square errors of the different regressions are constant within datasets for each focal length. Again, datasets derived from aerial pictures taken with the 28 mm lens show systematically lower RMSE values than for 50 mm-derived datasets. The high statistical correlations between the accuracies of the different datasets strongly suggest a non-random spatial pattern of the errors of topographic representations (Table 2.7; Figure 2.7).

Table 2.7: Statistical correlations (Pearson coefficient) between accuracies of each SfM dataset compared to LiDAR data.

	F28_T1_DS1	F28_T1_DS2	F28_T2_DS1	F50_T1_DS1	F50_T1_DS2	F50_T2_DS1
F28_T1_DS1	1	0.922	0.880	0.531	0.705	0.836
F28_T1_DS2		1	0.864	0.505	0.712	0.834
F28_T2_DS1			1	0.502	0.663	0.866
F50_T1_DS1				1	0.703	0.504
F50_T1_DS2					1	0.749
F50_T2_DS1						1

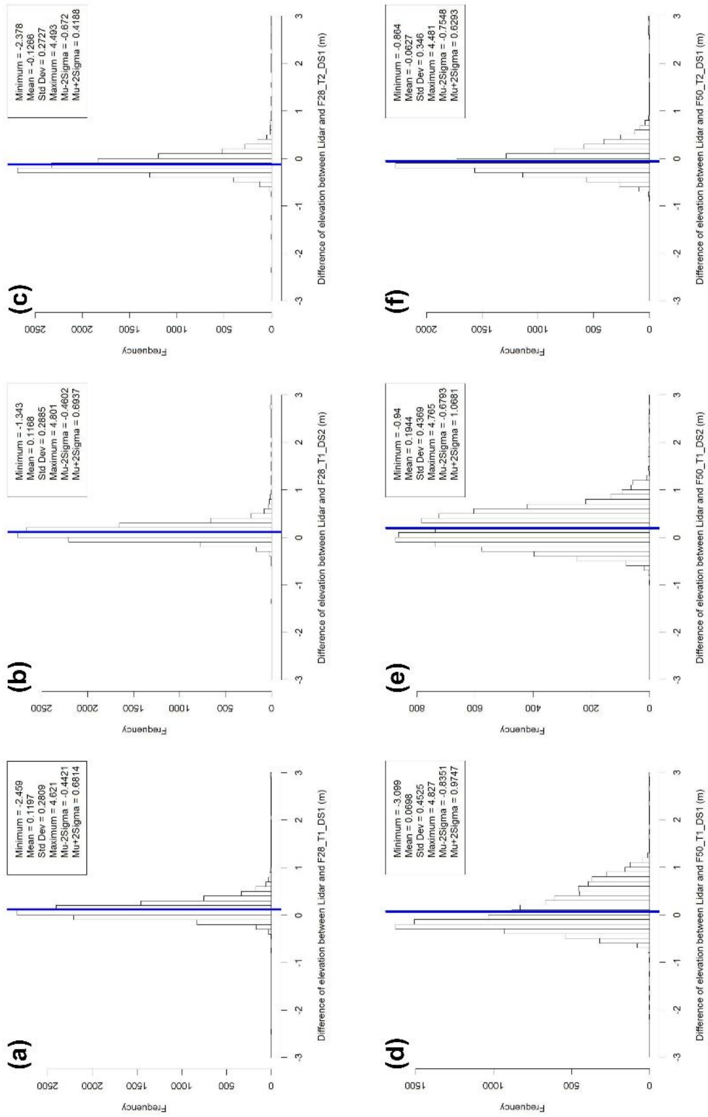

Figure 2.1: Accuracy assessment by DEM of difference between LiDAR and each DSM derived from point clouds. Histograms (a), (b) and (c) show elevation differences between LiDAR and 28 mm-focal-length datasets. Histograms (d), (e) and (f) show elevation differences between LIDAR and 50mm-focal-length datasets.

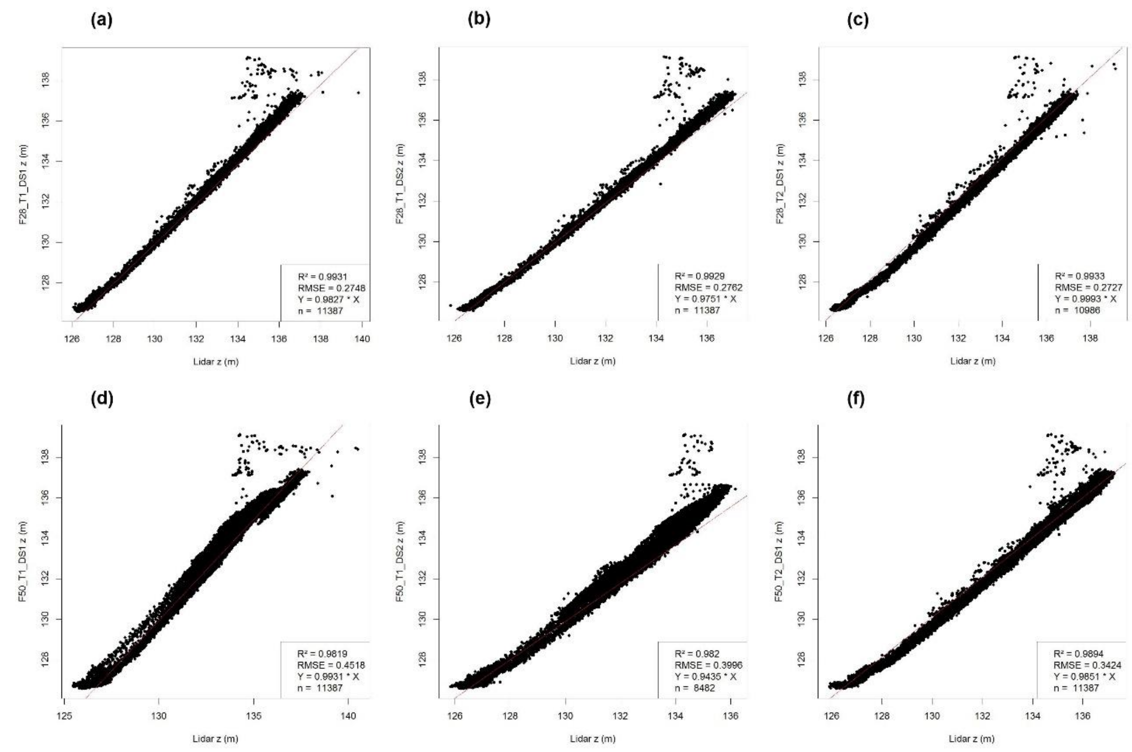

Figure 2.2: Simple linear regressions of LiDAR dataset versus SfM datasets. Graphs (a), (b) and (c) are comparisons of 28 mm-derived datasets with LiDAR. Graphs (d), (e) and (f) are comparisons of 50 mm-derived datasets with LiDAR. The red line represents the line of equality, i.e. the 1:1 line.

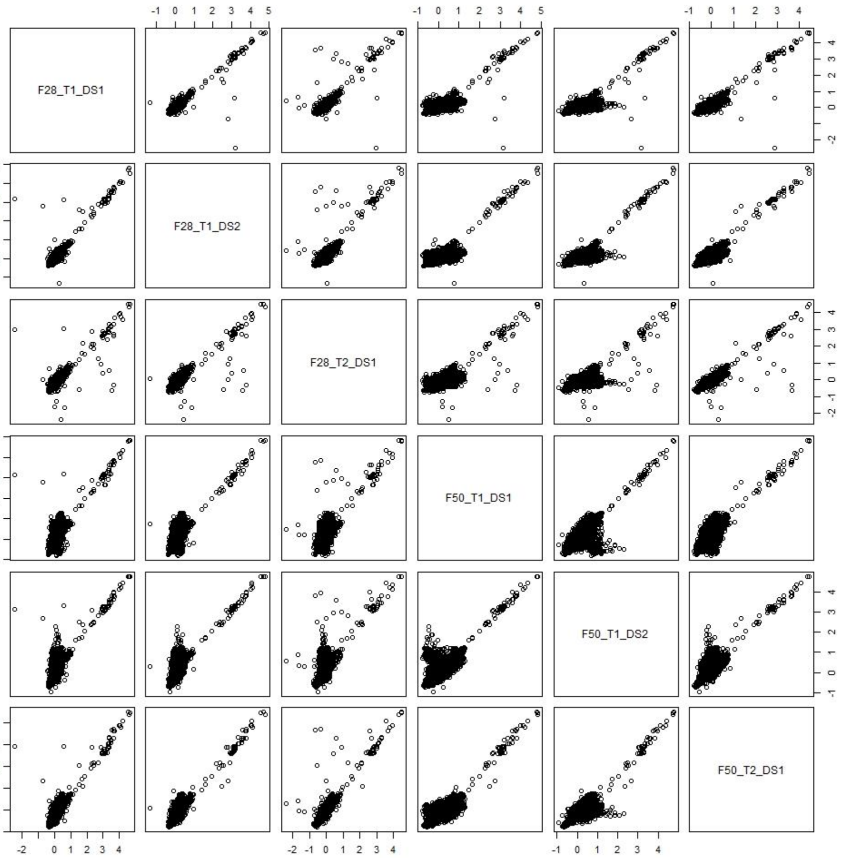

Figure 2.7: Correlations between accuracy of each SfM dataset compared to other replications.

Accuracies of the 28 mm-lens-derived datasets are highly correlated with each other, showing Pearson coefficients greater than 0.85. While identical replications with the 50 mm focal length, i.e. *F50_T1_DS1* and *F50_T1_DS2*, show lower accuracy in comparison with other datasets, the accuracy of *F50_T2_DS1* dataset is highly correlated with the 28 mm-focal-length-derived datasets. Finally, when comparing datasets with independent LiDAR data, the use of the 28 mm lens produces more accurate topographic reconstructions than the standard 50 mm lens. The location of the georeferencing targets, i.e. sets *T1* and *T2*, has no clear influence on the total accuracy of datasets compared to LiDAR data.

3.3. INTERNAL PRECISION ASSESSMENT

In order to assess the internal precision of topographic representations based on SfM point clouds, differences between identical replications were computed (Table 2.8; Figure 2.8). For the GCP set *T1*, identical replications with the wide angle lens provide a better reproducibility, i.e. a mean absolute difference of 0.06 m, with the smallest observed standard deviation (Figure 2.8a), in comparison with identical replications with the 50 mm lens, which has a mean absolute difference of 0.28 m and a higher dispersion of errors (Figure 2.8b). All other parameters being equal, the use of the 28 mm lens leads to higher internal precision of repeated topographic representations. The simple linear regression between the two 28 mm-derived datasets with the GCP set *T1* (Figure 2.9a) shows that observations are closely distributed along the line of equality with few outliers, which confirms the very high internal precision of the procedure. The associated RMSE value is only 0.12 m.

Table 2.8: Internal and external precision of 3D topographic reconstructions. Summary statistics of absolute differences of elevations between point-cloud-derived DSMs referred as Dataset 1 and Dataset 2 (metres).

Dataset 1	Dataset 2	Minimum	1st Quartile	Median	Mean	3rd Quartile	Maximum
F28_T1_DS1	F28_T1_DS2	0	0.022	0.047	0.063	0.081	6.261
F28_T1_DS1	F28_T2_DS1	0	0.181	0.243	0.239	0.295	6.056
F28_T1_DS2	F28_T2_DS1	0	0.162	0.243	0.237	0.306	5.812
F50_T1_DS1	F50_T1_DS2	0	0.116	0.247	0.284	0.387	3.021
F50_T1_DS1	F50_T2_DS1	0	0.142	0.293	0.349	0.516	12.06
F50_T1_DS2	F50_T2_DS1	0	0.116	0.255	0.341	0.535	2.854

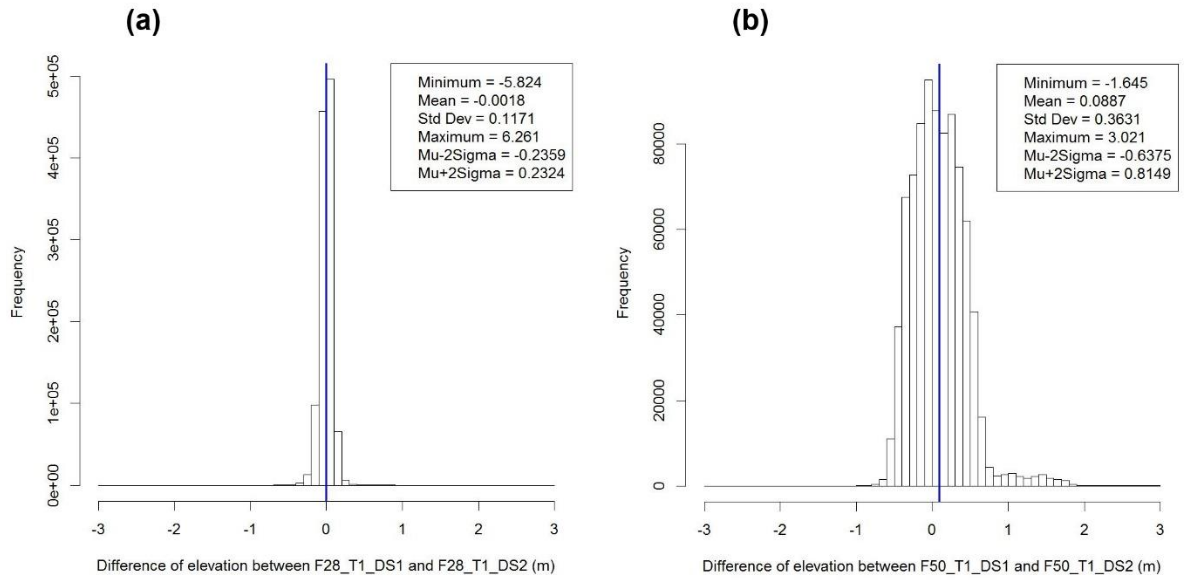

Figure 2.3: Internal precision assessment of 3D topographic reconstructions based on SfM workflow. Histograms (a) show differences of elevation for identical replications and aerial images acquired (a) with a 28 mm focal length and (b) with a 50 mm focal length.

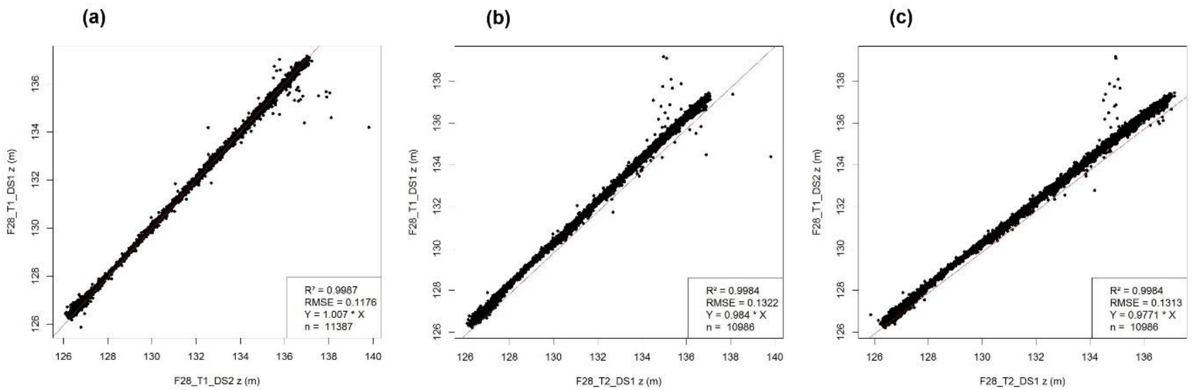

Figure 2.4: Simple linear regressions of SfM datasets derived from 28 mm focal length datasets. (a) Internal precision. (b) and (c) External precision controlled by GCP survey accuracy. The red line represent the line of equality, i.e. the 1:1 line.

3.5. EXTERNAL PRECISION ASSESSMENT

The external precision controlled by the accuracy of GCP georeferencing is here assessed by comparing datasets that are based on independent GCP sets, i.e. *T1* and *T2*. Considering only 28 mm-focal-length datasets, differences between replication with GCP set *T2* and the two datasets with GCP set *T1* show a mean absolute error of 0.24 m and low dispersion of values (Table 2.8; Figure 2.10a; 2.10b). In this case, the accuracy of GCP survey has a clear influence on the precision of topographic representations as the mean absolute error value is multiplied by four in comparison with error associated with identical replications (0.06 m), i.e. internal precision. A similar test with the 50 mm datasets shows higher absolute errors of 0.34 and 0.35 m (Table 2.8) and higher standard deviation values (Figure 2.10c; 2.10d). Simple linear regressions between 28 mm-derived datasets from independent GCP sets (Figure 2.9b; 2.9c) confirm good external precision as few outliers are observed. The fact that observations are slightly above the regression line (Figure 2.9b; 2.9c) is due to the systematic offset between 3D surfaces, induced by propagation of errors on the GCP survey. When changing the number of ground control points that are taken into account for georeferencing, our analysis shows that errors increase when the amount of ground control points decreases (Table 2.9).

Table 2.9: Assessment of external precision controlled by GCP location. Summary statistics of absolute differences between reference dataset F28_T1_DS1 and each dataset (metres).

Dataset	Minimum	1st Quartile	Median	Mean	3rd Quartile	Maximum
F28_15GCP_A	0	0.004	0.009	0.014	0.017	0.979
F28_15GCP_B	0	0.006	0.013	0.018	0.023	1.629
F28_9GCP	0	0.047	0.093	0.102	0.150	1.759
F28_4GCP	0	0.180	0.310	0.309	0.438	3.677

The mean absolute differences between reference dataset *F28_T1_DS1* and derived datasets range between 0.01 for 15 GCPs and 0.31 m for 4 GCPs. The two datasets with 15 GCPs at different locations show similar mean absolute differences, with values of 0.014 and 0.018 m respectively. As a consequence, all other parameters being equal, the pattern of GCPs has no influence on the precision of the 3D topographic representation if the number of GCPs is similar and sufficiently high, and if they are equally distributed over the study area.

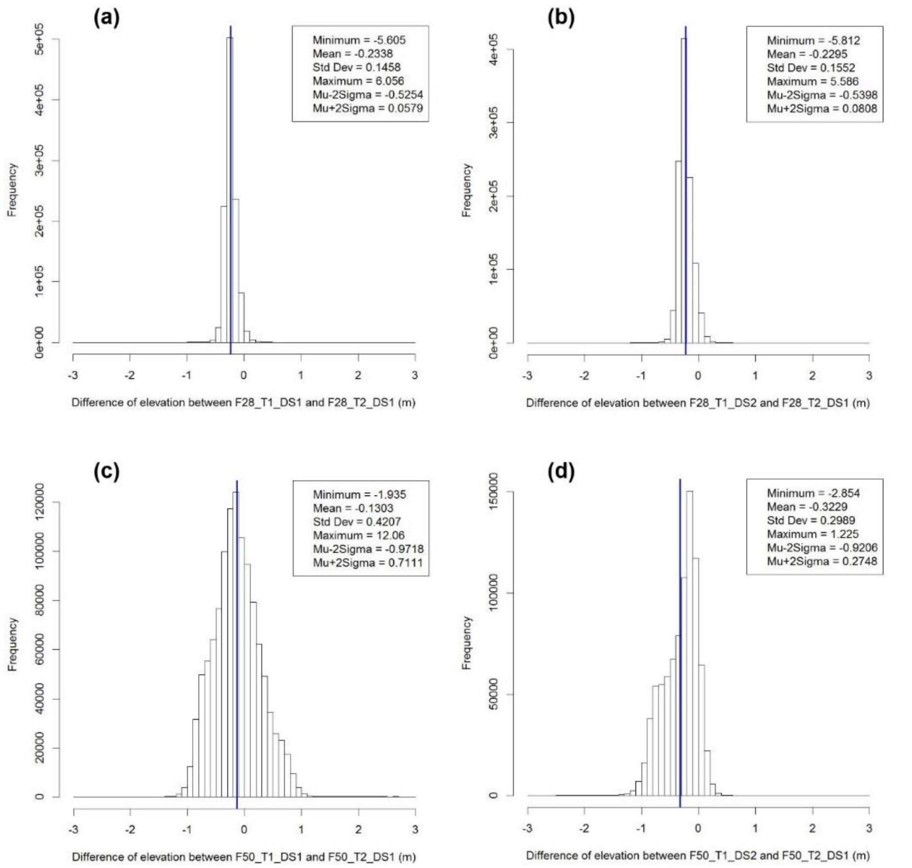

Figure 2.10: External precision of georeferencing assessment by DEM of differences between point-cloud-derived DSMs. Histograms (a) and (b) show comparisons between 28 mm-focal-length datasets with independent GCP sets. Histograms (c) and (d) show comparisons between 50mm-focal-length datasets with independent GCP sets.

4. DISCUSSION

By comparing 10 digital surface models of one particular study area, we attempted to assess the reproducibility of the UAV-SfM workflow. By focusing on a study area without major topographic changes, we were able to isolate the error terms that are associated with (1) the SfM algorithm itself, (2) the focal length of the lens, (3) the independent sets of GCPs, and, (4) the number and spatial pattern of GCPs. For operational monitoring of dynamic environments, these error terms have to be known to distinguish real changes in the topography from errors that rise from methodological considerations. Both accuracy and precision are here quantified over the entire surface covered by the point clouds. The measures that we present here are not based on a discrete set of points only. The LiDAR dataset was only available at a spatial resolution of 1 m and was acquired between 2000 and 2002. Major topographic changes between the acquisition dates of the LiDAR dataset and our UAV-SfM survey are not likely as the area is not subject to rapid soil erosion or landslide. However, the LiDAR data can only serve as a reference dataset and, strictly speaking, not as a ground truth dataset. To assess the absolute accuracy, ground truth data with higher spatial resolution are necessary, but not (yet) available for this study area.

Our results show that the accuracy of 3D topographic reconstructions is controlled by the camera lens, i.e. focal length and intrinsic quality of the components (image stabilizer and autofocus), and the set of georeferencing targets. Also, datasets derived from the 28mm focal length lens show better accuracies than those derived from the 50mm lens. The accuracy of datasets has clearly an influence on the precision of repeated measures. As a consequence, 50mm-derived datasets are generally characterised by lower precision than 28mm-derived datasets. We distinguished internal precision from external precision of 3D topographic reconstructions. Internal precision, i.e. reproducibility of the structure-from-motion workflow, is very high with a mean absolute error of 0.06 m for 28mm focal length. This suggests that the SfM algorithm in itself has very low impact on 3D topographic measurements. Moreover, this value captures the impact of multiple parameters influencing the quality of the aerial pictures, i.e. meteorological conditions, solar azimuth and zenith angles. In fact, wind speed may influence the flight path and stability of the UAV which can induce additional motion blur on the pictures. The interaction between clouds and the sun position may also create shadows on the aerial pictures that affect the automatic detection of invariant keypoint features. During operational flights for temporal analyses of topographic changes, these parameters should be maintained as constant as possible.

Besides, analysis of external precision shows that the accuracy of the GCP localisation clearly affects 3D topographic representations. In fact, the external precision is four times higher (one order of magnitude higher) than the internal precision for 28 mm-derived datasets. However, for the 50 mm lens, the external precision is of the same order of magnitude than the error for replications. This is mainly due to the lower accuracies of the replications with the 50 mm lens. The previous observation cannot be supported by any systematic statistical correlation between the accuracy of datasets compared to LiDAR and reproducibility between topographic measurements.

Even if the theoretical spatial resolution at a given altitude is finer with the 50 mm lens compared to the 28 mm lens, our UAV-SfM workflow generally shows better reproducibility with the use of the 28 mm lens. This result may seem to be counterintuitive, but can be explained by the higher quality of the 28 mm lens. In fact, the Canon EF 28 mm f/2.8 IS USM has an image stabilizer and a high-end autofocus, in contrast to the Canon EF 50 mm f/1.8 II low-end lens. With the Canon EF 28 mm f/2.8 IS USM lens, UAV-induced motion blur is reduced which permits to obtain a large majority of sharp images. However, we did not properly isolate the impact of components quality from the one of the focal length on the accuracy of topographic reconstructions. For both lenses, the constant and wide aperture is a clear advantage to obtain sharp pictures as it allows high shutter speeds which also help to counteract the UAV-induced vibrations. Moreover, the theoretical resolution provided by the 28 mm lens at 50 m above ground, i.e. 7.7 mm, is sufficient for many applications in geomorphology. Importantly, the image resolution is not the limiting factor to high reproducibility as we showed that it is mainly controlled by the GPS used to survey the GCPs, for which errors are an order of magnitude larger.

Finally, the spatial structure and the number of GCPs taken into account for georeferencing also play an important role on topographic reconstructions. Compared to other UAV-SfM based topographic reconstructions (e.g. Fernández et al., 2016;

Peternel et al., 2017; Stumpf et al., 2014), the density of GCPs in this particular study can be considered to be very high, i.e. ca. 30 pts ha^{-1}. It therefore provides highly accurate and precise measurements. However, a dense and regular distribution of GCPs is time-consuming and not always possible in rough or inaccessible terrains, e.g. glaciers or volcanoes. Assessing the influence of the amount of GCPs on the precision of the topographic reconstructions remains recommendable when one is obliged to decrease the number of GCPs below this optimal GCP density. Our study showed that using 15 instead of 30 ground control points only leads to a mean absolute difference of 0.01 m. The associated error increases by an order of magnitude when only 9 GCPs are used. These results can be explained by the rigidity of the Helmert 3D transformation that is here applied to the raw point cloud. Although this similarity transformation is easy to use, the main drawback is that georeferencing errors increase proportionally with the distance to ground control points. As a consequence, irregularly scattered GCPs, i.e. dataset with 9 GCPs, or large areas without GCPs, i.e. dataset with only 4 GCPs, might lead to large errors and weak reproducibility.

Although the results on reproducibility are encouraging for further geomorphic applications, several parameters can be modified to enhance the accuracy and precision of the measurements. First of all, the main limiting factor is the GPS used to survey the georeferencing targets. Because of the rigid Helmert 3D transformation applied to point clouds for georeferencing, the errors on GPS measurements propagate to final results. Besides, automatic extraction of georeferencing targets within point clouds based on RGB values is not perfectly efficient (Table 2.3). In fact, automatic extraction could be complemented by manual extraction on aerial pictures, such as the method implemented in the *sfm_georef* MATLAB toolbox developed by Westoby et al. (2012), in order to use all information available from the targets as to better constrain the parameter of the Helmert transformation.

In this setup, the density of GCPs used for georeferencing topographic reconstructions is very high in comparison to existing literature. Recent recent technological advances in the miniaturization of RTK GPS devices render the georeferencing of UAV-SfM point clouds using GCPs less crucial. Small RTK GPS systems can now be embedded on the UAV system and directly record its position when images are acquired. The RTK GPS is connected to a single-board computer that controls image acquisition by the camera and synchronizes it with the coordinates of the UAV. This setup eventually enables the user to perform direct georeferencing of topographic datasets and can allow one to overcome some of the limitations of using GCPs.

5. CONCLUSION

In order to assess the reproducibility of 3D topographic reconstructions based on aerial images acquired by an UAV platform and structure-from-motion algorithms, we repeatedly surveyed a study area characterised by gentle slopes, with varying parameters as independent sets of ground control points and focal length. Based on the different image datasets, earth topography representations were reconstructed with SfM algorithms and compared with each other. Our data show that best performances of 3D topographic representations are achieved based on datasets acquired with a 28 mm focal length lens equipped with an image stabilizer and a high speed autofocus motorisation. For these datasets, internal precision, i.e. mean absolute error controlled by SfM workflow only, is only 0.06 m, which shows that all other parameters being equal, reproducibility of topographic measurements based on our methodology is very high. Our data also show that the GPS survey accuracy of ground control points plays an important role on reproducibility as the mean absolute error between measurements derived from independent sets of GCPs is increasing by an order of magnitude in comparison with identical replications based on the same set of GCPs. Nevertheless, this external factor can easily be improved by using a very high-resolution (centimetre) RTK GPS for field measurements.

CHAPTER 3

UNRAVELLING EARTH FLOW DYNAMICS WITH 3D TIME SERIES DERIVED FROM UAV-SFM MODELS

Based on:

Clapuyt, F., Vanacker, V., Schlunegger, F., Van Oost, K. (2017), Unravelling earth flow dynamics with 3-D time series derived from UAV-SfM models, Earth Surface Dynamics, 5(4), 791–806, doi:10.5194/esurf-5-791-2017.

ABSTRACT

Accurately assessing geo-hazards and quantifying landslide risks in mountainous environments are gaining importance in the context of the ongoing global warming. For an in-depth understanding of slope failure mechanisms, accurate monitoring of the landslide topography at high spatial and temporal resolutions remains essential. The choice of the acquisition framework for high-resolution topographic reconstructions will mainly result from the trade-off between the spatial resolution needed and the extent of the study area. Recent advances in the development of unmanned aerial vehicle (UAV)-based image acquisition combined with structure-from-motion (SfM) algorithm for three-dimensional (3D) reconstruction make the UAV-SfM framework a competitive alternative to other high-resolution topographic techniques. In this study, we aim at gaining in-depth knowledge of the Schimbrig earthflow located in the foothills of the Central Swiss Alps, by monitoring ground surface displacements at very high spatial and temporal resolution using the efficiency of the UAV-SfM framework. We produced distinct topographic datasets for *three acquisition dates between 2013 and 2015 in order to conduct a comprehensive 3D analysis of the landslide. Therefore, we computed (1) the sediment budget of the hillslope, and (2) the horizontal and (3) the three-dimensional surface displacements. The multitemporal UAV-SfM based topographic reconstructions allowed us to quantify rates of sediment redistribution and surface movements. Our data show that the Schimbrig earthflow is very active with mean annual horizontal displacement ranging between 6 and 9 m. Combination and careful interpretation of high-resolution topographic analyses reveal the internal mechanisms of the earthflow and its complex rotational structure. In addition to variation in horizontal surface movements through time, we showed that the configuration of nested rotational units changes through time. Although there are major changes in the internal structure of the earthflow in the 2013-2015 period, the sediment budget of the drainage catchment is nearly in equilibrium. As a consequence, our data show that the time lag between sediment mobilisation by landslides and enhanced sediment fluxes in the river network can be considerable.*

1. INTRODUCTION

The northern Alpine border and particularly the foothills of the Central European Alps of Switzerland are prone to slope instabilities, with 6% of its surface area affected by landslide hazards (Lateltin et al., 2005). The widespread outcrops of Flysch and Molasse bedrock have thick interbedded mudstones, which increase conditions for landslide occurrence. This has led local authorities to draw particular attention to georisk management by identifying and assessing landslide hazards (Raetzo et al., 2002) to minimize socio-economic impacts through loss of human life and damage to infrastructure. Climate change is likely to increase landslide hazards in the near future (Crozier, 2010; Huggel et al., 2012). The ongoing global warming is characterised by higher mean, minimum, and maximum air temperatures and more frequent precipitation events (Cubasch et al., 2013), which in turn has an influence on pre-conditions and triggering mechanisms for landslides (Bennett et al., 2013; Crozier, 2010). The increasing trend in intense precipitation reported for the northern part of Switzerland is likely to change soil moisture conditions at the Alpine foothills during autumn and spring (Seneviratne et al., 2010).

The recent advances in high-resolution topography representation techniques and acquisition platforms, combined with decreasing surveying costs, have led to an increasing availability of topographic datasets over the last decade. High-resolution topographic reconstructions of the earth's landforms are nowadays used for accurate topographic representation and modelling in soil science, volcanology, glaciology, river and coastal morphology (Tarolli, 2014). The study of geo-hazards benefits from these technological advances for proper monitoring of surface displacements and topographic deformation (Caduff et al., 2015; Jaboyedoff et al., 2012; Joyce et al., 2009; Metternicht et al., 2005; Scaioni et al., 2014). Measurements of surface deformation can be retrieved from chronological sequences of sub-metre resolution topography. The choice of the acquisition framework for topographic representations will always result from the trade-off between (1) the spatial resolution needed and (2) the extent of the study area (Passalacqua et al., 2015). In the specific case of repeated measurements of landslide and hillslope processes in mountainous environments, the following three parameters are narrowing down the possibilities for the acquisition framework: (3) the surveying cost, (4) the necessary return period for proper monitoring, and (5) the accessibility of the study area.

In the past, the evolution of landslides was studied based on aerial photographs, which were used for either visual interpretation or photogrammetric reconstruction of digital elevation models (DEM), characterised by an accuracy of up to several metres over regional spatial extents (e.g. Casson et al., 2003; Guns and Vanacker, 2014; Hervás et al., 2003; Prokešová et al., 2010; Vanacker et al., 2003; van Westen and Lulie Getahun, 2003). Historical aerial photographs allow for reconstructing surface displacements over the last 50 years when data availability is optimal (Prokešová et al., 2010; van Westen and Lulie Getahun, 2003). However, the use of aerial photographs for monitoring dynamic environments is often limited by the relatively large time interval between flight campaigns along with accuracy and resolution, which does not match current standards for topographic representations. Optical satellite images, i.e. from ASTER, Quickbird or Pléiades, have successfully been used for landslide monitoring with decimetre accuracy by applying optical image correlation techniques on time series of satellite images (e.g. Delacourt et al., 2004; Kääb, 2002; Stumpf et al., 2017). Even though sub-metre resolution images such as from Pléiades are now used, the price of very high-resolution optical satellite imagery might remain an obstacle for long-term monitoring of dynamic environments that require frequent monitoring and dense time series. Surface deformation is now increasingly monitored using radar technology, that is synthetic aperture radar (SAR), and light detection and ranging (LiDAR). These techniques can be deployed on airborne and ground-based platforms that have distinct inherent accuracies and ranges (Passalacqua et al., 2015). Terrestrial or satellite SAR and airborne LiDAR (ALS) can cover areas ranging in size from one to thousands of kilometres for spacecraft-embedded SAR, at a metric spatial resolution. Ground-based LiDAR, i.e. terrestrial laser scanning (TLS), can provide topographic data of areas ranging in size from 0.01 to a few square kilometres at centimetre spatial resolution. For complex topography, multiple laser scans from different viewpoints are often required to cover the surface with reasonable overlap. In hummocky topography, the viewpoint's visibility fields can be particularly narrow. Spacecraft-embedded SAR data, e.g. TerraSAR-X and ALOS/PALSAR images, enable tracking displacements of landslides characterised by important variations in vegetation cover and soil surface between the acquisition dates (e.g. Raucoules et al., 2013; Schlögel et al., 2015). Aerial and ground-based LiDAR datasets have mainly been used for landslide monitoring using DEM differencing (e.g. Blasone et al., 2014; Ventura et al., 2011; Wheaton et al., 2010) and image correlation (Travelletti et al., 2014). The spatial or temporal resolution and/or high acquisition cost have so far limited the applicability of traditional photogrammetric reconstructions, high-resolution optical satellite imagery and aerial- and satellite-based laser scanning for multi-temporal three-dimensional (3D) analyses of landslide-prone areas.

A recent technique to reconstruct very high-resolution topography is the image-based structure-from-motion (SfM) algorithm. Based on pictures taken from a standard camera, 3D topographic reconstructions can cover up to several-kilometre-wide study areas if the camera is carried by an unmanned aerial vehicle (UAV; Immerzeel et al., 2014; Lucieer et al., 2014; Rippin et al., 2015). UAV-SfM has similar performance to TLS data, i.e. decimetre to centimetre accuracy output (*Chapter II*). Compared to other topographic acquisition techniques, the UAV-SfM framework is low-cost and flexible in its implementation and is particularly attractive for survey campaigns in poorly accessible landslide-prone terrain. The UAV-SfM technique is now widely applied for single 3D topographic reconstructions and mapping of natural environments (Eltner et al., 2016). However, the potential of the SfM algorithm and the derived 3D dense point clouds is not yet fully exploited for landslide monitoring. Time series of topographic data derived from UAV-SfM data are mainly used to compute DEMs of differences (DoD) from temporal pairs of topographic representations (Fernández et al., 2016; Huang et al., 2017; Peternel et al., 2017; Tanteri et al., 2017). DEM differencing has been combined with image correlation techniques (COSI-Corr) to assess horizontal displacements and determine landslide dynamics (Lucieer et al., 2014; Turner et al., 2015). Recent UAV-based landslide studies included the assessment of point-based horizontal displacements from displacement vectors between corresponding features on pairs of orthophotos (Fernández et al., 2016; Peternel et al., 2017), and cross-section profiles to get an insight into the landslide's internal structure (Tanteri et al., 2017). Using ground-based images, Stumpf et al. (2014) assessed the seasonal dynamics of the Super-Sauze landslide over a 2-year period, by using a 3D change detection algorithm, i.e. multiscale model to model cloud comparison (M3C2).

This paper aims to take benefit from time series of UAV-SfM-derived topographic representations at very high spatial resolution and evaluate the application of low-cost and lightweight methods to infer internal landslide dynamics in mountainous environments. As such, UAV-SfM models can complement data on the internal structure and landslides' dynamics that are commonly derived from geophysical and/or geotechnical methods (e.g. Fressard et al., 2016; Merritt et al., 2014; Perrone et al., 2014).

This study differs from previous work that applied the UAV-SfM framework on landslide-prone areas. First, the accuracy and reproducibility of the UAV-SfM-based topographic representations is directly accounted for in the change detection. Second, the landslide kinematics and dynamics are reconstructed based on information from hillslope sediment budgets, image correlation techniques and 3D point cloud analyses. We hypothetize that UAV-derived datasets provide essential data to improve our understanding of landslide kinematics and dynamics and of the hillslope soil residence time in landslide-prone catchments, improving landslide hazard assessments. The UAV-SfM framework was applied to a study site in the Central European Alps of Switzerland where three distinct topographic datasets were generated for 2013, 2014 and 2015.

2. METHOD

2.1. STUDY AREA

The study area is the Schimbrig landslide located in the northern foothills of the Central Swiss Alps, between Bern and Lucerne (Figure 3.1; Figure 3.2). This landslide is categorized as an earthflow, composed of centimetric to decimetric large clasts embedded in a matrix of silt and mud. The landslide is located in the small, i.e. 4 km² large, Rossloch River catchment, which is part of the Entle River drainage system (Schlunegger et al., 2016a, 2016b). The centre of the earthflow is located in 46°56’38”N / 8°05’56”E.

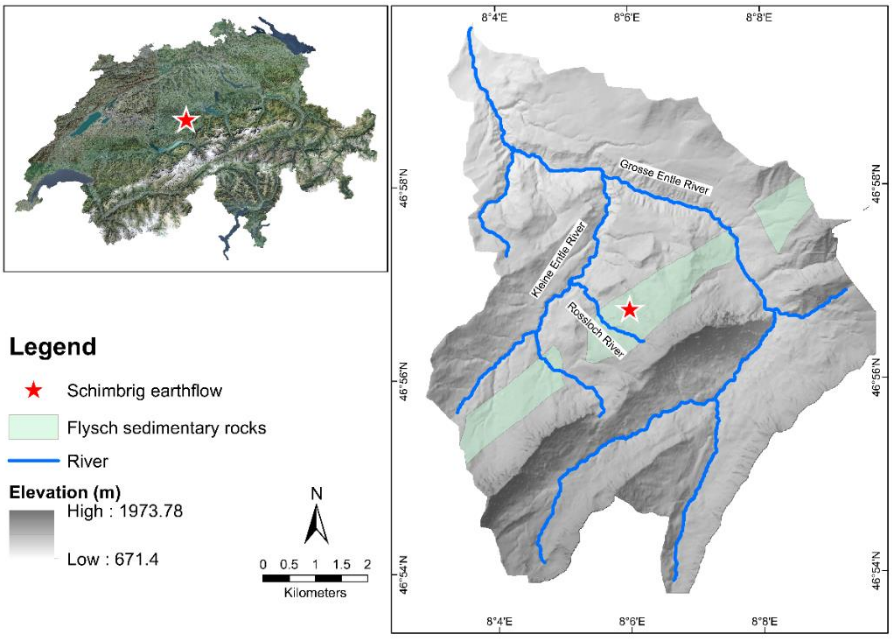

Figure 3.1: Location of the Schimbrig landslide in Switzerland (inset) and in the Entle river catchment.

Previous studies on the Schimbrig earthflow cover a broad temporal surveying scale from decades (Schwab et al., 2008) to one century (Savi et al., 2013). Our survey complements earlier work in the sense that we will substantially improve the temporal and particularly the spatial resolution of monitoring. The catchment area is composed of three litho-tectonic units, oriented SW-NE. The upper part, including the Schimbrig ridge culminating at ca. 1,800 m a.s.l., is formed by a Late Cretaceous to Eocene suite of limestones, marls and quartzites, exposed in the Helvetic thrust nappes. The limestones form steep slopes, which are subject to rockfalls (Schlunegger et al., 2016b). Subalpine Flysch deposits are dominant in the intermediate part of the catchment between 1,100 and 1,400 m a.s.l., where the earthflow is situated. This landslide covers an area of ca. 45 ha, with a central active part where bare soil is exposed. Whereas the earthflow lies on the lower parts of the Schimbrig hillslopes, it is geomorphically decoupled from the adjacent Rossloch River (Figure 3.1). The lower part of the catchment is covered by conglomerate bedrock knobs of the subalpine Molasse, which form small resistant conglomerates ridges and constrain the flow direction of the earthflow in its lower segment (Schlunegger et al., 2016b).

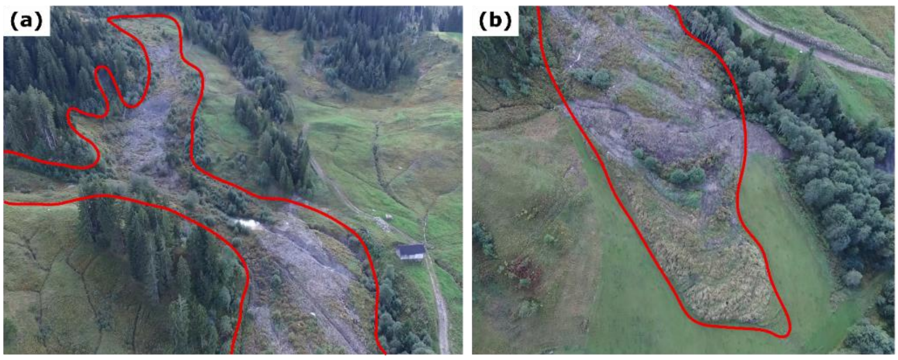

Figure 3.2 : Aerial views of the Schimbrig earthflow. (a) Upper part of the earthflow. (b) Frontal lobe of the earthflow.

Seasonal slip rate variability of the area has been determined by Schwab et al. (2007) based on global positioning system (GPS) measurements over a period of 14 months between 2004 and 2005. Slip rates were more intense in early spring and late summer and ranged between 0.1 and 0.25 m month^{-1}. During the other periods, slip rates were much lower and ranged between 0 and 0.1 m month^{-1}. This displacement pattern has been related to seasonality in soil moisture content. The same authors have not identified an immediate response of this earthflow to rainfall rates. On the decadal scale, volumetric changes of the Schimbrig flow were quantified using classic photogrammetry based on aerial photos from 1962 to 1998 by Schwab et al. (2008). They showed that extreme and episodic changes in slope morphology do not affect the long-term sediment transport to the channel network. Based on dendrogeomorphic analyses, Savi et al. (2013) qualitatively assessed the spatial pattern of geomorphic activity within the Schimbrig area over the last 150 years. Their analyses showed that the earthflow is a source of sediment, and the material mobilised by gravity is slowly supplying material to the drainage network by slow ground movements.

2.2. DATA ACQUISITION AND DATA PROCESSING

In order to provide a spatial analysis of surface deformation through time, a time series of very high-resolution datasets of the Schimbrig area is necessary. Given the high geomorphic activity in the area (Schwab et al., 2008), yearly surveys were planned to accurately capture earthflow movements at high temporal resolution. Three image acquisition campaigns were organised in October 2013, June 2014 and October 2015. Early autumn and late spring periods were chosen in order to minimize the effects of vegetation growth. Image acquisition is done using a UAV platform, i.e. a custom Y6 multirotor with embedded DJI controllers. It is equipped with a stabilized camera mount, which compensates for tilt and roll movements to maintain the fixed orientation of the camera. The used camera is a standard small-format (i.e. 18.0 effective megapixel CMOS APS-C sensor) reflex camera (Canon EOS 550D). The lens is a fixed-focal-length lens (Canon EF 28mm f/2.8 IS USM), equipped with an optical image stabilizer and a high-speed autofocus motorization. The ground surface is surveyed both with nadir-oriented and with a 45°-tilted camera, as the inclusion of oblique images in the SfM algorithm has been shown to decrease systematic errors in topographic reconstruction and to better capture complex 3D structures (*Chapter II*; James and Robson, 2014). Given a mean speed of 2 m s^{-1} to avoid motion blur induced by the UAV platform, the acquisition frequency is set at a rate of one image per 2 s in order to have a high overlap between consecutive images at ca. 60 m above ground, i.e. above 70%, because high redundancy improves the performance of the SfM algorithm. Adjacent flight lines are separated by 15 m to maintain high lateral overlap of aerial images (Figure 3.3). Even though image acquisition has been performed in diverse light conditions depending on the hour of the day and cloud coverage during flights, the bottom line has always been to shoot in shutter speed priority mode and maintain a high value to avoid motion blur. Camera, flight and imaging parameters are summarized in Table 3.1 (O'Connor et al., 2017).

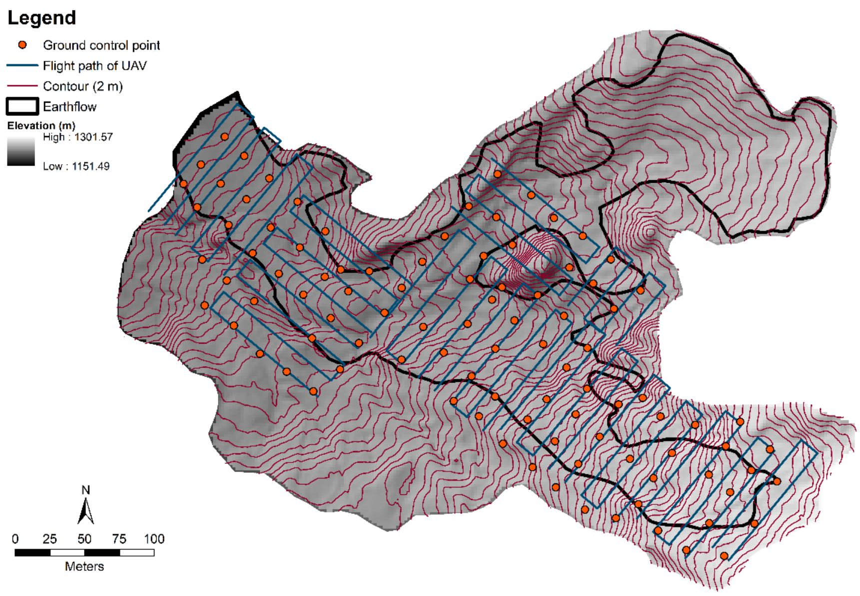

Figure 3.3: Settings of the UAV flights and GCP location (example from the October 2015 survey).

The point clouds are generated from overlapping optical images using the SfM algorithm. Structure-from-motion is a computer vision algorithm that uses the set of unoriented overlapping pictures to reconstruct the 3D scene structure without additional a priori information (Snavely et al., 2006, 2008). The output 3D point cloud is computed in a relative image-based coordinate system, and then georeferenced by matching the real-world coordinates of the georeferencing targets with those expressed in the image-based coordinate system. Based on the list of point pairs, the Helmert transformation parameters, i.e. translation vector, rotation matrix, and scaling factor, are computed and applied to the entire point cloud. The output point clouds were georeferenced in post-processing based on ground control points (GCP), i.e.

georeferencing targets, that were regularly scattered over the fly zone (Figure 3.3), and surveyed with a centimetric accuracy GPS receiver (*Chapter II*). Despite the rough topography of the earthflow, a regular grid having 25 m distance between GCPs was possible. A limited number of measurements were not used in the final georeferencing as their associated error was abnormally high due to poor GPS signal reception.

Table 3.1: Camera and imaging characteristics for all the surveys.

Camera model	Canon EOS 550D
Lens model	28mm f/2.8 IS USM
Image resolution	5184 * 3456 pixels
Crop factor	1.6
Approximate sensor size	22.3 * 14.9 mm
Pixel pitch	4.3 µm
Mean shutter speed	1/1250
Mean ISO	388
Mean f number	3.49
Flight velocity	2 m/s (idealized)
Flight height	60 m (idealized)
Ground sample distance	9.2 mm

The georeferenced point clouds were filtered in order to statistically remove outliers. The root mean square error (RMSE) between the GPS coordinates and the position of the georeferencing targets in the point cloud serves as a measure of the accuracy of the 3D topographic reconstruction. These accuracy values are subsequently used to infer the error that is associated with the topographic representations and they define the detection limits for the multitemporal analyses. Finally, 3D point clouds are interpolated into digital surface models (DSM), which are then aligned. Both datasets serve as input for the analyses of the hillslope sediment budget and horizontal displacements. The resolution of the outputs was set based on the average density of 3D point clouds and standardized for all the datasets.

To quantify internal deformation of the Schimbrig earthflow, three distinct and complementary analyses are realized on the time series of 3D point clouds. First, the sediment budget is evaluated by computing DoD between DSMs, using the Geomorphic Change Detection software (Wheaton et al., 2010). Uncertainties associated with each surface representation, i.e. the accuracy values of 3D point clouds, are considered to be uniform over the entire study area. We subsequently analyse thresholded DSMs. The errors on the topographic representations are then propagated in the calculations of the DoD and quantities of erosion and deposition. By computing differences between DSMs, the mass balance of the earthflow is derived from the difference between the total eroded volume and the total deposited volume of sediments. Additionally, the average net thickness difference in elevation is computed by dividing the net volume difference by the surface area of the earthflow.

Then, horizontal surface displacements are computed using the COSI-Corr image correlation algorithm (Ayoub et al., 2009; Leprince et al., 2007). Correlation is computed based on a moving window that scans dataset pairs. We used pairs of shaded relief surfaces to detect horizontal displacements. This method is particularly suitable for monitoring slow deformation processes, like the Schimbrig earthflow, with clearly distinguishable surface deformation structures, such as cracks, fissures, and scarps. The COSI-Corr algorithm results in horizontal displacements expressed as two layers, i.e. the north-south component and the east-west component, which are combined to compute the intensity and direction of ground movements. The horizontal displacement analysis is complementary to the above-mentioned 3D analysis of point clouds: the presence of micro-topography and vegetation in the 3D point clouds facilitates the quantification of lateral earth movements using the COSI-Corr algorithm. As such, the complexity of the earthflow including erosion and accumulation areas and horizontal displacements of the earthflow body is better represented. For each time interval, descriptive statistics, i.e. minimum, mean, median, quartile and maximum, are computed for the distribution of horizontal displacement values.

Finally, 3D distances between point clouds are computed to measure the 3D topographic evolution through time by highlighting zones of erosion, scarp retreat, surface subsidence, and zones of bulging and sediment accumulation. The multiscale model-to-model cloud comparison is used to compute 3D distances between point clouds because it directly operates on point clouds without meshing or gridding and provides a confidence interval associated with each distance measurement (Lague et al., 2013), in contrast to other cloud, mesh or raster distance computation techniques. For a set of core points, i.e. either the entire point cloud or a subsample, the method first computes surface normals in 3D. Then, along these normals, the local distance between clouds is the difference between the projection of core points on each cloud. Finally, a spatially variable confidence interval, i.e. a level of detection of local distance between clouds at 95%, is computed based on the registration error, i.e. the accuracy of point cloud georeferencing, and the local roughness of each core point projection along the normals. This confidence interval allows distinguishing statistically significant changes between two point clouds (Lague et al., 2013). Again, simple descriptive statistics are computed on the distribution of local distances between point clouds for each time interval.

The SfM processing and 3D point cloud georeferencing are performed using the Agisoft Photoscan® software. Sediment budgets were computed with the Geomorphic Change Detection software (Wheaton et al., 2010) implemented in ArcGIS. COSI-Corr algorithm has been used as a software module integrated in ENVI. Point cloud handling has been done with CloudCompare, using the M3C2 plugin. All other data manipulations were carried out with R software, CloudCompare and ArcGIS 10.

3. RESULTS

3.1. 3D TOPOGRAPHIC RECONSTRUCTIONS

The three topographic reconstructions are not covering the same spatial domain (Table 3.2; Figure 3.4). The flight campaign of June 2014 allowed us to survey the entire Schimbrig earthflow. The 2013 and 2015 flight campaigns are centred on the most active part of the earthflow but do not cover the entire earthflow due to operational problems encountered during the flight. Due to these spatial limitations, results are presented: (1) over the spatial intersection of the three datasets ($T_{2013} \cap T_{2014} \cap T_{2015}$), i.e. area of interest named *intersection*, to allow the comparison of absolute values of displacement and volumetric changes over the entire time period (2013-2015), and (2) over the spatial intersection of each time interval ($T_{2013} \cap T_{2014}$ and $T_{2014} \cap T_{2015}$), i.e. area of interest referred to as *interval*, in order to get the most information of each pair of datasets.

Table 3.2: Characteristics and accuracy assessment of 3D point cloud reconstructions. Root mean square errors (RMSE) are the standard deviation of differences between the coordinates of the ground control points, i.e. georeferencing targets, measured by GPS and the coordinates of these points within the 3D point clouds after georeferencing. Horizontal RMSE is computed by taking the horizontal components of the point coordinates, while the vertical RMSE is computed by taking only the z component of point coordinates.

		October 2013	**June 2014**	**October 2015**
Point cloud characteristics	**No. of pictures**	1143	4519	2501
	No. of GCPs	49	108	99
	Area (ha)	5.86	17.69	15.59
	Point density (pts m^{-2})	**1456**	**1270**	**1080**
RMSE (m)	**Horizontal**	0.23	0.20	0.20
	Vertical	0.06	0.05	0.08
	Total error	**0.24**	**0.20**	**0.22**

The 3D point cloud reconstructions of the Schimbrig earthflow result in a large dataset, with a very high point density of ca. 1,000 to 1,450 points per square metre, which allows accurate tracking of ground deformation through time. The three topographic reconstructions have similar accuracies, i.e. RMSE (Table 3.2), with horizontal accuracies of 0.23 and 0.20 m, and vertical accuracies of 0.06, 0.05, and 0.08 m.

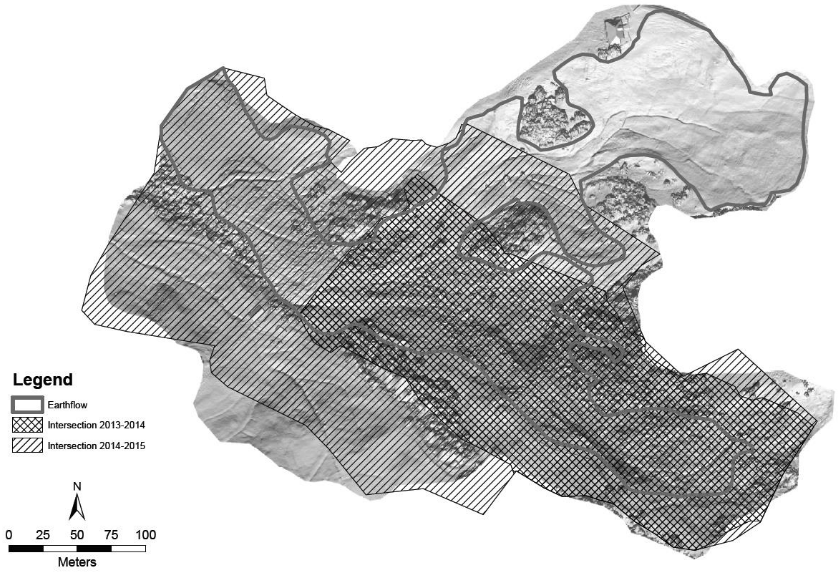

Figure 3.4: Intersections of point cloud datasets for the 2013-2014 and 2014-2015 time intervals.

The total error on the topographic reconstructions ranges between 0.20 and 0.24 m. The overall detection limits for ground movements and deformations are derived from error propagation of the RMSE values on the individual topographic constructions given in Table 3.2. The detection limits are similar for the two time intervals (Table 3.3), with a value of 0.31 m for 2013-2014 and 0.30 m for 2014-2015. For further analyses, changes which are smaller than the detection limit of our UAV-SfM framework are not reported.

Table 3.3: Limit-of-detection values for temporal analyses (metres).

		2013 - 2014	**2014 - 2015**
Limit of detection (m)	**Horizontal**	0.30	0.28
	Vertical	0.08	0.09
	Total	**0.31**	**0.30**

3.2. GEOMORPHOLOGICAL MAP

Based on the time series of very high-resolution DSMs, their associated shaded relief surfaces, slope maps, and field observations, a geomorphological map (Figure 3.5) of the Schimbrig area is produced following Seijmonsbergen (2013) and the landslide classification by Varnes (1978). Field observations consist of GPS measurements of the scarp, flow lines and boundaries of the earthflow. Identification of stable ridges and visual analysis of geomorphic units are based on expert knowledge.

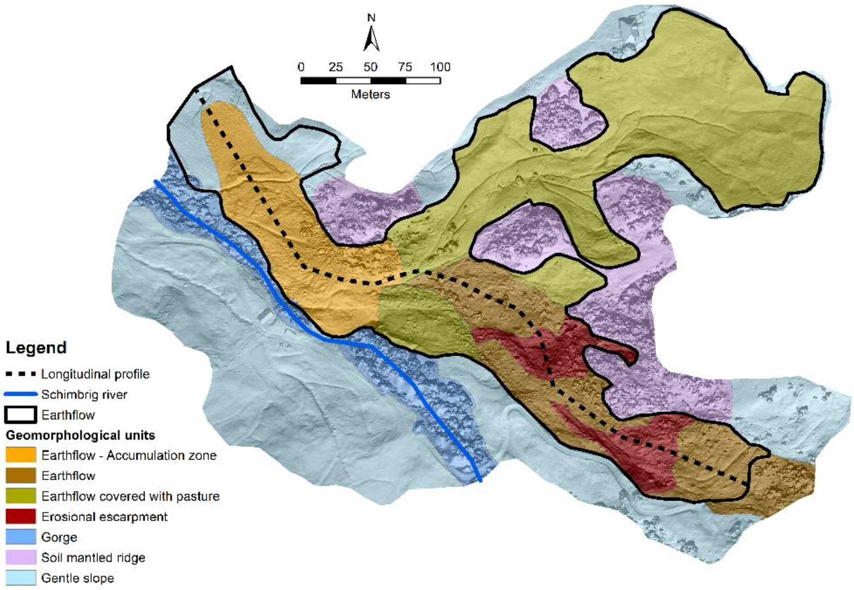

Figure 3.5: Geomorphological map of the study area. The black dashed line locates longitudinal profiles displayed in Figure 3.11.

The Schimbrig earthflow is constrained by stable bedrock ridges covered by trees on the northeastern part, and by relatively stable grasslands on the southwestern part. The main track of the earthflow is from the southeast to the northwest, and it contains two scarps in the upper part that expose up to 25 m. The earthflow is characterised by a rough surface and a patchwork of vegetated surfaces covered by herbs and small shrubs and bare surfaces where wet and bare soil (silt and mud with embedded clasts) is exposed. The secondary track flows from the northeast to southwest and joins the main track upslope of its accumulation zone.

3.3. SEDIMENT BUDGET

Inputs for the sediment budget are the DSMs interpolated from 3D point clouds at the best spatial resolution possible, i.e. 0.04 m, based on the density of point clouds. To account for uncertainties related to the UAV-SfM reconstructions, a spatially uniform detection limit has been applied to each input dataset as defined in Table 3.2. Over the intersection of the surveyed areas, the estimated volume of deposited material is 6,012 ± 1,919 m³, for the first period of interest, i.e. between October 2013 and June 2014 (Table 3.4; Figure 3.6).

Table 3.4: Volumetric (cubic metres) and depth (metres) sediment budgets. Errors on volumetric measurements account for limits-of-detection for each time interval defined in Table 3.3.

Area of interest	Intersection				Interval	
Time interval	2013-2014		2014-2015		2014-2015	
	Estimate	Error (±)	Estimate	Error (±)	Estimate	Error (±)
Total volume of erosion (m³)	-11,345	3,118	-9,054	2,329	-15,093	4,098
Total volume of deposition (m³)	6,012	1,919	8,293	2,546	17,005	4,533
Total net volume of difference (m³)	-5,333	3,661	-762	3,450	1,912	6,111
Average net thickness difference (m)	-0.22	0.15	-0.03	0.14	0.05	0.15

The volume of eroded material is larger, with an estimate of -11,345 ± 3,118 m³. For the first period, there is a net negative change in volume indicating that the removal of material is larger than the accumulation of sliding material for the surveyed surfaces. On average, there is lowering of the surface of 0.22 ± 0.15 m (Table 3.4). Field observations reveal a similar pattern. It is important to note that the lower part of the earthflow, where the debris is accumulating in a frontal lobe, is not included in the topographic analyses. Field observations indicate that only a minor part of the sliding material might have been transported to the river network via the Rossloch River.

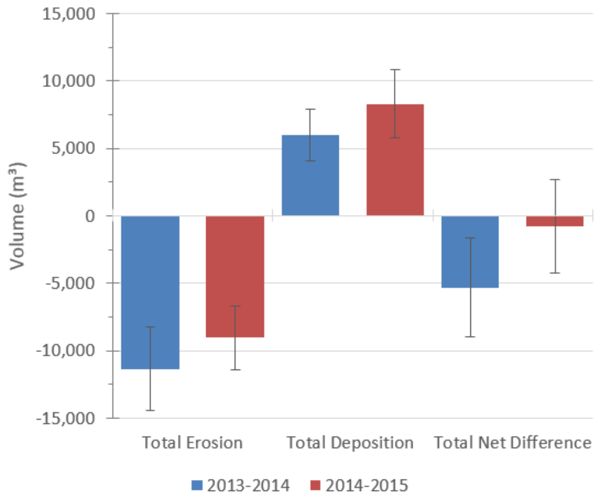

Figure 3.6: Volumetric sediment budget computed for the spatial intersection (*intersection* dataset) of the three datasets (see Table 3.4 for details on values and associated error bars).

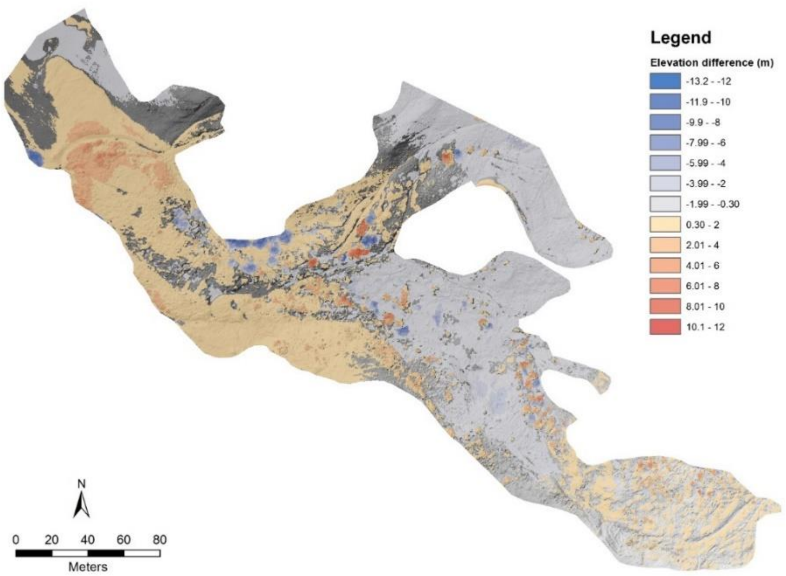

Figure 3.7: Elevation difference between two topographic reconstructions for the time interval June 2014 - October 2015.

The sediment budget computed over the second time interval, i.e. between June 2014 and October 2015, for the area of intersection is nearly at equilibrium (Table 3.4; Figure 3.6) with a net volume of difference of -762 m^3 ± 3,450 m^3. This suggests that the sliding material that is mobilised by the earthflow accumulated within the area of intersection. When analysing the internal flow dynamics of the larger sliding area (*interval*) over the second time interval, it is clear that the sediment budget is slightly positive (Table 3.4). This analysis now also captures the frontal lobe of the landslide that bulged and advanced during this time interval. Figure 3.7 also shows that the upper and lower part of the earthflow are bulging areas, while the intermediate zone is experiencing surface subsidence.

3.4. HORIZONTAL DISPLACEMENTS

The COSI-Corr image correlation algorithm uses pairs of single-band input to quantify horizontal displacement. A north-directed illumination on the DSMs allows for highlighting topographic features and ground deformation properly, as well as the presence of low vegetation. Shaded relief surfaces derived from the 3D point clouds (with a spatial resolution of 0.2 m) provided the best results for the correlation analyses. It is important to mention that input data with smaller spatial resolution generated incoherent displacement results, associated with high signal-to-noise ratio. In fact, under 0.2 m resolution, image correlation led to false positive correlation between features due to the very complex topography of the earthflow. Pixels characterised by a signal-to-noise ratio lower than 0.9 or by displacement vectors that are smaller than the detection threshold are discarded for further analyses. To allow comparison between the two time intervals that have a different duration, i.e. 8 versus 17 months, the displacement values are here represented as mean annual displacement values (Table 3.5).

For the period between October 2013 and June 2014, the fluxes are relatively high and well confined by stable morphologic ridges surrounding the earthflow (Figure 3.8). The displacement pattern is rather uniform over the entire length of the earthflow, suggesting that the earthflow body is moving downslope between stable bedrock ridges.

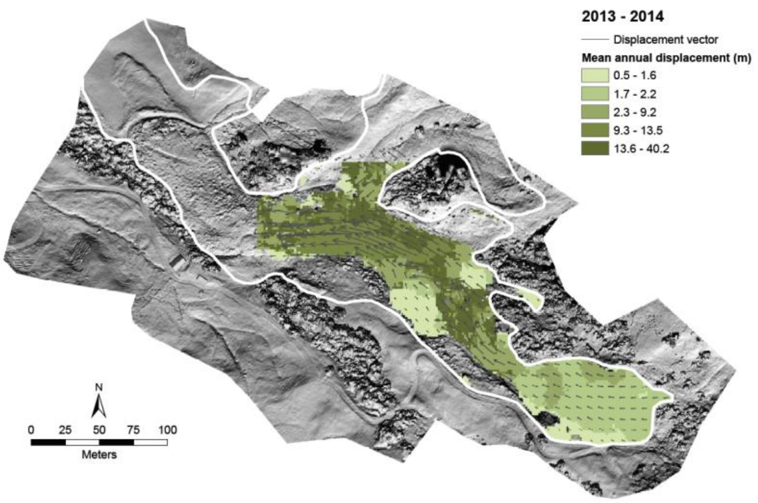

Figure 3.8: Surface displacements for 2013-2014 using the COSI-Corr algorithm. Displacement vectors are indicative of relative magnitude and direction of movement and do not reflect true ground displacements.

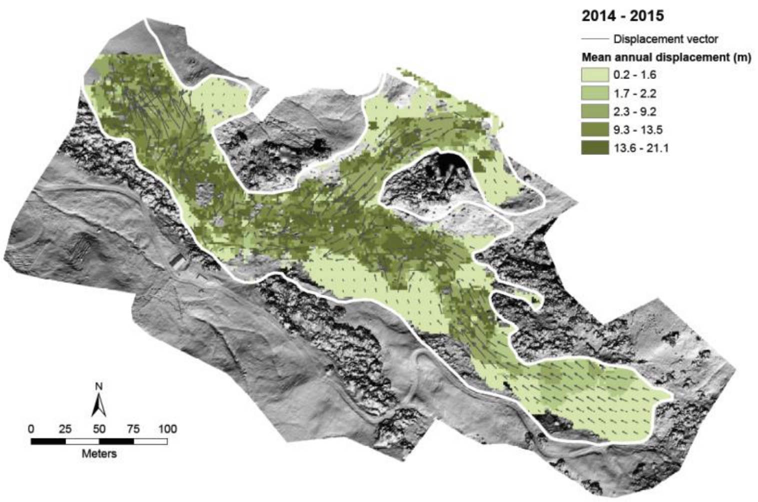

Figure 3.9: Surface displacements for 2014-2015 using the COSI-Corr algorithm. Displacement vectors are indicative of relative magnitude and direction of movement and do not reflect true ground displacements.

Table 3.5: Mean annual horizontal displacement (metres) computed using the COSI-Corr algorithm applied on shaded relief surfaces.

Area of interest	Intersection		Interval
Time interval	**2013-2014**	**2014-2015**	**2014-2015**
Min.	0.47	0.23	0.23
1st Q.	1.81	0.89	0.89
Median	3.74	2.20	3.62
Mean	8.91	5.74	6.30
3rd Q.	13.06	11.25	11.84
Max.	40.16	21.06	21.06

The zones that show higher sliding activity are the lower scarp of the earthflow and its adjacent flat slope. The mean annual horizontal displacement for this first period is about 8.9 m. The output from the measurements during the second period of interest (2014-2015) shows a slightly different pattern of surface displacements (Figure 3.9). The areas with highest displacements are located in the surroundings of the two scarps in the upper part, in the secondary track of the earthflow, and in the lower accumulation zone where the frontal lobe spectacularly advanced downslope. In the flatter area between the two scarps, the horizontal movement is less pronounced and the direction of movement is rather diffuse. When comparing the surface displacements for the two time periods over the same study area, it is clear that the magnitude of the horizontal displacements is lower in the second period with a mean annual displacement of 5.7 m.

A comparison with field measurements realized during the flight campaigns in 2013, 2014, and 2015 indicates that the spatial pattern of the horizontal movements that were automatically extracted by the correlation algorithm are generally coherent with field observations: the stable morphologic ridges constrain the direction of the earthflow movement. Although the spatial pattern is highly consistent, the absolute displacement of the frontal lobe of the earthflow is not properly captured, as the frontal lobe advanced by ca. 55 m (Figure 3.10).

Figure 3.10: Aerial images illustrating the advance of the frontal lobe of the earthflow between June 2014 and October 2015.

3.5. 3D COMPARISON OF EARTH TOPOGRAPHY

Distances between 3D point clouds are computed using the M3C2 algorithm. For each pair of point cloud datasets, a subsample of the first 3D point cloud is taken as the set of core points, with a minimum distance of 0.5 m between points, to avoid extensive computation time. Descriptive statistics are computed on the point cloud distances (Table 3.6) which were filtered from values under the detection threshold.

Table 3.6: Descriptive statistics of the distances between 3D point clouds (metres).

Area of interest	Intersection		Interval
Time interval	**2013-2014**	**2014-2015**	**2014-2015**
Min.	-20.72	-27.56	-28.83
1st Qu.	-1.06	-1.00	-0.89
Median	-0.60	-0.49	-0.43
Mean	-1.04	-0.69	-0.38
3rd Qu.	0.47	0.66	0.79
Max.	20.36	26.96	26.96

The dominance of negative values can be interpreted as predominance of ground subsidence in flat parts or scarp retreat in steeper areas of the earthflow. Contrariwise, positive values are zones of surface bulging in the zones of accumulation or accumulation of debris at the frontal lobe.

4. DISCUSSION

4.1. APPLICATION OF UAV-SFM FRAMEWORK FOR LANDSLIDE MONITORING

Using the UAV-SfM framework, three very high-resolution topographic datasets were obtained over a 2-year period that allowed us to accurately quantify the internal dynamics of the earthflow and the sediment redistribution within the study area. First of all, the study confirms the efficiency of the UAV-SfM framework to perform natural hazard monitoring at very high spatial resolution. In comparison with other high-resolution topographic methods (Passalacqua et al., 2015; Smith et al., 2015), the UAV-SfM technique, along with terrestrial laser scanning technology, provides the highest spatial resolution of surface reconstructions. Two main advantages of the UAV-SfM framework are its flexibility and its low-cost and lightweight, which are convenient for repeated measurements of dynamic environments, and more particularly when deployed to acquire aerial imagery in remote and poorly accessible areas. Similar to terrestrial laser scanning, which has similar spatial accuracy and range, the UAV-SfM framework requires careful setup and planning of georeferencing targets and image acquisition to adequately and accurately capture the 3D scene of complex topography (*Chapter II*; Caduff et al., 2015; James et al., 2017b). Being an airborne acquisition platform, the UAV-SfM has the advantage of configuring a dense network of optimal viewpoints independent of terrain complexity and access difficulties.

The workflow applied for the research is based on our previous work on reproducibility of the technique (*Chapter II*). The use of ground control points is time-consuming for large areas, as it requires a sufficient number of observations that are well distributed around the study area. However, both criteria were fulfilled in our surveys. Only some GCPs, i.e. less than 5%, were discarded from the analysis because of the important associated error on the GPS measurement. Consequently, the use of the GCP georeferencing technique does not significantly affect our results, as observations were not included in the bundle adjustment step. However, we are confident that direct georeferencing technique for UAV-SFM framework will soon become a standard procedure as compact and low-cost real-time kinematic (RTK) receivers are now available and suitable to be embedded on UAV platforms. Performance of direct georeferencing has recently been assessed and showed to be at least similar to GCP georeferencing (Carbonneau and Dietrich, 2017; James et al., 2017a). In fact, this technique increases the field survey efficiency as the amount of GCPs can be significantly reduced and more importantly, it will increase the accuracy of topographic reconstructions where accessibility to place GCPs is drastically limited, e.g. volcanic terrains and glaciers. For further surveys of the Schimbrig earthflow, our workflow has to be adapted to include direct georeferencing. In this case study, a 1-year time interval between surveys was suitable to capture the internal dynamics of the earthflow (Schwab et al., 2007). With respect to this, our 3D temporal database is considered as dense. We recognize that other natural hazards may require a higher frequency of measurements, which can easily be achieved using UAVs. Even though our results about landslide structure and dynamics need to be viewed against geophysical or geotechnical field investigations, this study shows the potential of time series of UAV-SfM topographic reconstructions to provide complementary data on internal landslide dynamics in complex terrain.

One of the main drawbacks of the UAV-SfM framework is the need for the UAV platform to acquire aerial pictures. The use of UAVs is now increasingly subjected to more stringent regulations, including a pilot license, UAV registration, and insurance certificates (Stöcker et al., 2017b). Moreover, UAV flights are only possible under optimal meteorological conditions, and wind and rain may be a limiting factor in mountainous areas.

4.2. SCHIMBRIG EARTHFLOW MONITORING

Post-processing of the time series of DSMs provides sediment budgets, horizontal displacements and 3D comparisons of surfaces that allow us to monitor the internal dynamics of the landslide at very high spatial and temporal resolution. By qualitatively combining quantitative single results, which may initially seem redundant, it is possible to quantify the magnitude and rate of sediment redistribution and surface movements within the area affected by the Schimbrig earthflow and more importantly to capture the internal mechanisms of the earthflow (Figure 3.11).

As such, the very high-resolution topographic reconstructions allow analysis of the spatio-temporal evolution of earthflow-prone terrain, as well as going beyond conventional survey methods and expert knowledge (Savi et al., 2013; Schwab et al., 2007, 2008). Savi et al. (2013) provide a historical insight into the Schimbrig sliding activity based on dendrochronology over the last 150 years. These qualitative data on hillslope processes provide information on surface displacements that extends beyond the time span of photogrammetric techniques, but the temporal information has its limits regarding quantitative and continuous data on displacement rates. A first attempt to quantify slip rates of the earthflow was carried out by Schwab et al. (2007), who tracked control points using GPS measurements. However, we are now able to compute slip rates over the entire extent of the earthflow at very high temporal resolution applying image correlation algorithms to very high-resolution aerial images. Schwab et al. (2008) complemented their topographic analysis of the earthflow using classic photogrammetry and aerial photographs spanning the last 50 years. Independent of the spatial resolution of the output and price of data acquisition, photogrammetric analyses are very valuable as they allow for capturing surface displacements at larger scales and over longer time periods than data derived from the UAV-SfM framework, even though the time interval between the data sets may be a limiting factor (e.g. Prokešová et al., 2010; van Westen and Lulie Getahun, 2003). In the Rossloch catchment (Figure 3.1), Schwab et al. (2008) emphasized that sediment fluxes in the trunk streams are not directly controlled by the production of loose material through landsliding on the hillslopes. Consequently, the time lag between sediment production on the hillslopes and sediment evacuation in the river network highlights the intermittent coupling between hillslopes and channels. This is confirmed by our high-resolution topographic analysis and the computed hillslope sediment budget.

For the estimation of the annual volumetric sediment yield, potential variations in material bulk density were neglected. We acknowledge that this abstraction might introduce some bias in our assessments, although it is probably minimal. (1) The Schimbrig earthflow is exclusively located within homogenous Flysch deposits (Schwab et al., 2008). Even though some carbonate boulders originating from the Schimbrig ridge are embedded in the Flysch matrix, we hypothesise that these small variations do not lead to significant changes in the sediment budget computation. (2) Given the extent of the study area, i.e. 6 to 18 hectares, it was out of the scope of the current study to realise very high-resolution bulk density assessments for the area.

The UAV-SfM framework allows one to go a step further in the interpretation of the earthflow's internal structure and dynamics. When superimposing the temporal series of the three sets of topographic analyses and interpreting it in a very detailed way, we were able to show the complex rotational structure of the earthflow (Figure 3.11). Our data show that the entire body of the earthflow is sliding but that there exist strong differences in internal deformation and flow velocities within the sliding material. By combining the results from the 3D comparison between the point clouds and the DoD, it is possible to map the succession of ground surface subsidence and bulging areas over the 3-year period. Notwithstanding the short monitoring interval, the pattern of internal deformation of the earthflow changed its configuration (Figure 3.5). Between October 2013 and June 2014, the earthflow had a succession of three nested rotational units. In the upper part of the study area, two steep scarps are present. These active scarps control the downward movement of two tilted blocks (see Figure 3.5). The location of the two main scarps advances by ca. 8 m during the 2013-2014 period. A third rotational unit is larger: it is defined by the lower steep scarp located in the middle part of the earthflow and extends over the lower and flatter part of the earthflow down the frontal lobe. During the second period of monitoring, i.e. between June 2014 and October 2015, two rotational units can clearly be distinguished, i.e. a small upper block that is confined above the upper active scarp and a larger heterogeneous sliding mass that extends down to the frontal lobe of the earthflow. Unlike the first period of interest, the lower erosional scarp is not active, and there is no distinction between the second and third part of the sliding mass.

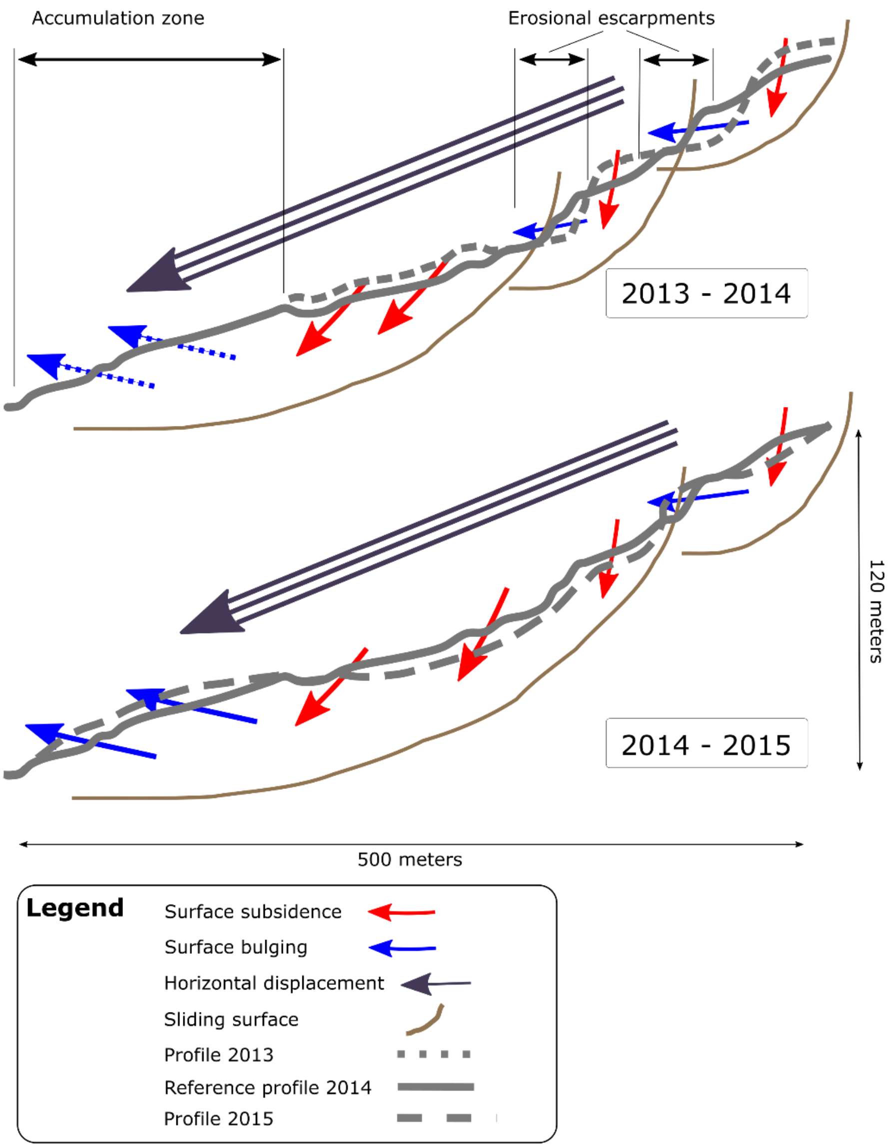

Figure 3.11: Schematic summary of the internal dynamics of the Schimbrig earthflow based on very high-resolution monitoring using the UAV-SfM framework. Longitudinal profiles depicting the surface of the earthflow are based on topography datasets from this study. Figure 3.5 locates them in the Schimbrig area.

The very high-resolution spatio-temporal analyses demonstrate that the Schimbrig earthflow was very active over the monitoring period. Results from the image correlation algorithm highlight the strong internal redistribution of sliding material within the earthflow, as well as rapid changes in the spatial pattern of displacement vectors. The mean annual horizontal displacements are large, with values of ca. 9 m between October 2013 and June 2014 and ca. 6 m between June 2014 and October 2015. This is partly explained by the fact that the central part of the earthflow is advancing toward the foot of the earthflow between October 2013 and June 2014, and this advance is accompanied by surface subsidence along the main track. This phase is followed by bulging in the accumulation zone, and a strong advance of the frontal lobe of the landslide over a distance of ca. 55 m.

Notwithstanding the strong internal deformation of the sliding material, there is no net effect on the sediment flux at the outlet of the Rossloch River. Our data show that the overall sediment budget of the earthflow is nearly in equilibrium and is spatially very consistent with the results on the displacement vectors and distances derived from the point clouds. After the major surge that occurred in 1994, the earth surface lowered by ca. 12 m in the central track of the earthflow (Schwab et al., 2008). More than 20 years later, the earthflow shows strong internal deformation that is related to the re-adjustment and self-reorganisation of the sliding material after the 1994 surge event. This suggests that phases of enhanced earthflow kinematics are not necessarily leading to enhanced sediment export to the fluvial system, as a result of the time delay between successive phases of earthflow reactivation and the sediment export from the catchment.

5. CONCLUSION

The UAV-SfM framework is increasingly applied in geomorphology to accurately capture the topography of given scenes. As it is low-cost and flexible in its implementation, and particularly suitable for surveying dynamic environments in poorly accessible terrain, we used this methodology to quantify ground surface displacements of the Schimbrig earthflow, located at the foothills of the Central Swiss

Alps, at very high spatial and temporal resolution. Based on three topographic reconstructions between autumn 2013 and 2015, we were able to conduct a comprehensive 3D analysis of the landslide by combining the sediment budget of the hillslope, and the horizontal and the three-dimensional surface displacements.

Combination and careful interpretation of the three topographic analyses of this study allow reconstructing the internal dynamics of the earthflow and highlight its complex rotational movement. In addition to variation in horizontal surface movements through time, we interestingly showed that the rotational structure of the earthflow is also varying from year to year. Additional field surveys will be required to increase the temporal series of topography reconstructions and confirm our findings. Results also confirm that the Schimbrig earthflow was very active, with mean annual horizontal displacements between 6 and 9 m. Besides, we showed that the sediment budget of the hillslope is nearly at equilibrium. In fact, the earthflow experienced a major sediment pulse more than 20 years ago and is still re-adjusting to this new setting. Therefore, our very high spatial and temporal resolution analysis supports the findings of Schwab et al. (2008) about the time lag between sediment production on hillslopes and fluvial processes, i.e. enhanced sediment fluxes, in trunk streams, based on lower spatial and temporal resolution time series of DEMs.

CHAPTER 4

SPATIO-TEMPORAL DYNAMICS OF SEDIMENT TRANSFER SYSTEMS IN LANDSLIDE-PRONE ALPINE CATCHMENTS

ABSTRACT

Tectonic and geomorphic processes drive landscape evolution over different spatial and temporal scales. In mountainous environments, river incision sets the pace of landscape evolution, and hillslopes respond to channel incision by e.g. gully retreat, bank erosion and landslides. Sediment produced during stochastic landslide events leads to mobilisation of soil and regolith on the slopes that can later be transported by gravity and water to the river network. Quantifying sediment storage and conveyance requires an integrated approach accounting for different space and time scales. To better understand mechanisms and spatial and temporal scales of geomorphic connectivity in mountainous environments, we characterised the sediment cascade of the Entle River catchment located in the foothills of the Central Swiss Alps. We quantified sediment fluxes over annual, decadal and millennial time scales using respectively UAV-SfM techniques, classic photogrammetry and in-situ produced cosmogenic radionuclides. At the annual scale (2013-2015), the sediment budget of the Schimbrig earthflow is roughly in equilibrium, despite the fact that we measured intense sediment redistribution on the hillslopes. At the decadal scale (1962-1998), Schwab et al. (2008) reported episodes of sediment export that were not directly related to increased geomorphic activity on the hillslopes. At the millennial scale, catchment-wide denudation rates show a positive relationship with downstream

distance or drainage area, when ignoring landslide-affected catchments. The latter are characterised by a negative relationship between denudation rates and downstream distance, along with high variability in denudation rates. The high denudation rates that we measured in the earthflow-affected Schimbrig catchment are illustrative for its high rates of geomorphic activity in comparison to adjacent areas. Our data show that the elevated denudation rates of the landslide-affected catchments are not necessary traceable when analyzing long-term sediment fluxes of the wider geographic area, as the landslide-affected catchments are often only a small fraction of the total catchment. The multi-temporal assessment of sediment fluxes indicates that (1) landslides can provide local sediment pulses, and mobilise material that becomes available for further mobilisation and transport when hillslopes and channels are connected. (2) Connection and disconnection cycles occur at decadal time scale. (3) Phases of high geomorphic activity at the catchment scale are episodic over thousands of years. Consequently, one single landslide has not necessarily an impact on the long-term sediment budget of first-order catchments. Rather, it is the cumulated effect of multiple landslides which are intermittently connected to the channel network at the decadal scale that may regulate sediment fluxes at the regional scale over the millennial time scale.

1. INTRODUCTION

The cascade of sediment is a widely used concept to describe the routing of sediment particles from sources to sinks throughout the landscape (Walling, 1983). Among other factors, e.g. topography, lithology, climate or tectonic activity (e.g. Aalto et al., 2006; Montgomery and Brandon, 2002; Whipple and Tucker, 1999), the geomorphic coupling and sediment connectivity control the pathways of sediment transfer in geomorphic systems, and eventually landscape evolution (Bracken et al., 2015; Fryirs, 2013; Harvey, 2001; Heckmann and Schwanghart, 2013). Geomorphic coupling is commonly seen as the linkage between individual landforms by sediment transport (e.g. Harvey, 2001; Heckmann and Schwanghart, 2013) while sediment connectivity was recently defined as the transfer of sediments between all the potential sources and sinks within a system, controlled by the geomorphic coupling between distinct landscape units (Bracken et al., 2015).

At global scale, the sediment delivery to continental margins is not spatially uniform nor steady. Mountainous rivers are particularly efficient conveyors of sediment to coastal regions (Larsen et al., 2014), but processes of erosion, transport and deposition do not occur at a constant rate in space and time. This makes the behaviour of geomorphic systems complex and sometimes difficult to assess, model and predict (Burt and Allison, 2010). In mountainous environments, landslide processes are a dominant source of sediments (Korup et al., 2010), with the amount of sediment displaced being a function of their magnitude and frequency (e.g. Crozier and Glade, 1999; Hovius et al., 1997; Malamud et al., 2004). The contribution of landslides to the overall sediment budget is still poorly constrained, as their geomorphic efficiency varies according to mechanisms and scales of sediment connectivity (Burtin et al., 2014; Korup et al., 2010).

Landslides stochastically supply sediment to the river network: the regolith displaced by landslides on the hillslopes is transported downslope, remobilised and evacuated to the channel network as sediment. The time lag between the onset of displacement on the slopes and the supply of landslide-derived material to the river channel is driven by the occurrence of superimposed landslides, gully channels or surface runoff evacuating colluvial material from temporarily sediment sinks on the slopes (e.g. Benda and Dunne, 1997; Bennett et al., 2014). Field studies have shown that the landscape buffering capacity can strongly vary: from several years (Berger et al., 2011; Fuller and Marden, 2010) to decades (e.g. Bennett et al., 2013; Schwab et al., 2008) using photogrammetrically-derived digital elevation models, and millennia (e.g. Wang et al., 2017) using cosmogenic radionuclides. In particular, sediment dynamics related to co-seismic landsliding are extensively studied. Earthquakes such as the Chi-Chi or Wenchuan events in Asia, trigger widespread and simultaneous sediment pulses that can be tracked over time using remote sensing techniques (e.g. Parker et al., 2011), gauging stations (e.g. Dadson et al., 2004), or geochronological dating techniques (e.g. Wang et al., 2017). These observational datasets are valuable to disentangle scales and patterns of sediment connectivity, and calibrate long-term landscape evolution models. However, the inherent stochastic nature of sediment production and transport prohibits linear upscaling of small-to-medium scale geomorphic process assessments, as well as extraction of a particular erosion mechanism from the entire sediment cascade using long-term/large-scale methods (Bennett et al., 2014; Bracken et al., 2015).

Few studies have attempted to unravel spatio-temporal patterns of the sediment cascade in landslide-affected catchments. Mackey et al. (2009) compared decadal measurements of surface displacement velocities of an earthflow derived from historical airphotos with millennial transport rates for the transport zone, derived from meteoric ^{10}Be inventories. Their study highlighted that the displacement rate of the Eel earthflow (northern California) was highly episodic in time, as the earthflow acted as a source of sediments over the last 150 years with an erosion rate that was more than 20 times faster than the millennial sediment transport rate. In a similar study by Delong et al. (2012), surface displacement rates derived from light detection and ranging (LiDAR) data were compared with ^{10}Be-derived denudation rates of two adjacent catchments. In this study of the Mill Gulch earthflow, the denudation rates computed between 2003 and 2007 were similar to long-term denudation rates. While field-based mono-temporal studies remain important to elucidate sediment transport mechanisms and rates, a spatio-temporal approach is needed to assess the sediment dynamics and the mechanisms of sediment connectivity in landslide-prone environments. This requires one to go beyond the time integrative approach used by Mackey et al. (2009) and DeLong et al. (2012), by quantifying the geomorphic processes rates over a confined spatial extent at different time scales. Spatial consistency requires that the spatial extent and scale of the datasets is similar, so that the geomorphic process rates can be quantified for a given area at different time scales.

The aim of this study is to quantify the spatio-temporal dynamics of sediment transfer systems, and elucidate the processes controlling hillslope-channel coupling over 10^0-10^3 years. Integrating sediment dynamics in landslide-prone environments over different time scales enables us to capture the stochastic character of geomorphic processes, e.g. landslides, and assess the propagation of sediment pulses from the hillslopes to the channels. Our analysis is based on a multi-temporal assessment of sediment dynamics in a small mountainous catchment. The Schimbrig catchment, located in the foothills of the Central Swiss Alps, was selected for this study. First, we quantified millennial-scale sediment fluxes from the Schimbrig catchment. Then, we discuss the spatial variability in millennial denudation rates for the Entlebuch region, by integrating our new ^{10}Be-derived denudation rates with previously published data on the Entle catchment by Van den Berg et al. (2012). Finally, we analyze the temporal variability in sediment fluxes, by comparing the millenial scale sediment fluxes with decadal (Schwab et al., 2008) and annual sediment flux data (*Chapter III*).

2. CONCEPTUAL FRAMEWORK

It is now widely acknowledged that soil and regolith transport on hillslopes and transfer of this material to and in river channels are stochastic processes (*Chapter I*). To include the stochastic character of the geomorphic processes in sediment routing systems, we need quantitative data on the occurrence and frequency of the processes, and on their impact on the sediment dynamics of mountainous catchments. Here, we propose a conceptual framework of hillslope connectivity that enables us to capture the occurrence and periodicity of geomorphic events, and to assess the propagation of sediment pulses from hillslopes to river channels by integrating different time scales (Figure 4.1).

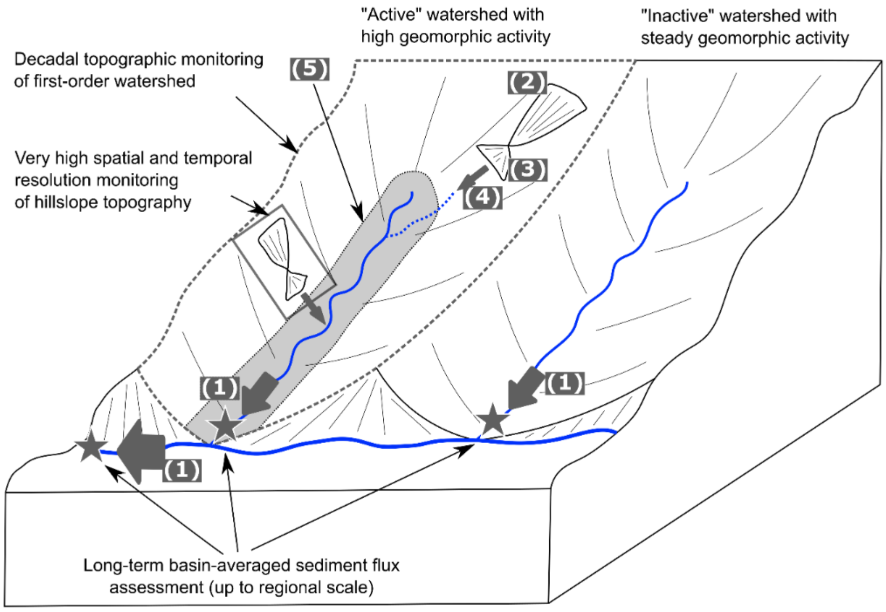

Figure 4.1: Conceptual framework of the sediment dynamics in alpine landslide-affected first-order catchments. (1) Long-term sediment flux from first-order catchments. (2) Sediment production and mobilisation on hillslopes, i.e. stochastic sediment pulses driven by landslide processes. (3) Temporal sediment storage on hillslopes, i.e. landslide colluvial fans. (4) Hillslope-channel connectivity-driven sediment flux. (5) Zone of geomorphic coupling between adjacent hillslopes and channels, through e.g. slope failures induced by river undercutting.

In the proposed model, we focus on the sediment routing system at the hillslope and catchment scales for landslide-prone catchments, and make abstraction of mass losses by e.g. deep weathering or wind erosion. Sediment connectivity controls the geomorphic coupling between the slopes and river channels over different temporal scales. On the hillslopes, landslides act as sediment factories and initiate the mobilisation of regolith, leading subsequently to stochastic sediment pulses. After landslide initiation, an important fraction of the landslide-derived material is not directly transferred to the river network, and accumulates on the slopes as landslide colluvial fans when hillslopes are not coupled to the channel network. The local accumulation of landslide deposits often goes along with an intense sediment reorganisation on the slopes to reach a new state of equilibrium (*Chapter III*). Subsequently, superimposed debris flows, surface creep or gully channels control the transfer of sediment from colluvial deposits to the river network, during short periods of geomorphic coupling between hillslopes and channels (Schwab et al., 2008). These episodes of geomorphic coupling are often triggered by extreme precipitation or seismic events. In upstream mountainous catchments, the fluvial network is often sediment supply-limited and the sediment is then effectively transported by the river to downstream reaches (Van den Berg et al., 2012).

Besides the spatial connectivity between hillslopes and channels described above, the following temporal aspects condition the propagation of a landslide-driven sediment pulse along the sediment cascade. When using direct observations, typically collected over several decades, only few high-magnitude low-frequency landslide occurrences can be observed in a given geomorphic setting. When active, the landslides mobilise a large amount of regolith on the hillslopes and can have a significant impact on the sediment dynamics. When inactive, other geomorphic processes like e.g. water erosion and soil creep are contributing sediment to the river system, resulting in a lower than average sediment supply to the river network. The pattern and rate of episodic landsliding can be quantified at annual and decadal time scale using direct measurements, and their frequency will control the long-term sediment mobilisation in the hillslope domain. Because sediment transport acts as a nonlinear filter that destroys environmental signals (Jerolmack and Paola, 2010), the signal of the landslide-driven sediment pulse is dampened along the sediment cascade. Hence, the high geomorphic process rates that we can observe in the landslide-affected hillslope domain are not necessarily transmitted to the river system. Figure 4.1 illustrates this concept of stochastic sediment pulses being dampened at larger spatial and temporal scale.

Attempting to capture sediment pulse propagation along the sediment cascade inherently implies integrating different spatio-temporal scales: from the annual and decadal to millennial time scale, and from the hillslope domain where landslides occur to the colluvial and fluvial domains where sediments are transported downstream. The time scale dependency of geomorphic processes is known as the Sadler effect. Initially suggested to highlight the completeness of stratigraphic records, it outlines that an inverse linear relationship exists between one-dimensional sedimentation rates and the time span of measurements, because of the unsteady and discontinuous character of sedimentation (Sadler, 1981). This time scale dependency has also been associated with periods of stasis or inactivity which occur episodically over long time scales and decrease measured rates (Paola et al., 2018). When assessing sediment dynamics at the hillslope-channel domains, the time scale dependence which might compromises one-dimensional rates becomes less evident to assess (Sadler and Jerolmack, 2015). At the landscape scale, the catchment-wide rates of denudation or deposition can capture a range of geomorphic processes that all contribute in different proportions to the measured denudation rates and integrate periods of activity and inactivity. Moreover, Sadler and Jerolmack (2015) showed that there is no compelling dependence between upland denudation rates and averaging time, except at time scales shorter than a month.

The framework outlined in Figure 4.1. allows us to evaluate the spatio-temporal dynamics of the sediment routing system. To do so, a dataset of denudation rates and sediment fluxes was established. At the annual scale, the geomorphic processes in the hillslope domain (10^0-10^1 km²) were monitored using very high-resolution topographic reconstructions. At the decadal scale, the sediment dynamics of first-order catchments were quantified from time-series of digital elevation models using classic photogrammetry. Finally, catchment-averaged cosmogenically radionuclide (CRN)-derived processes rates integrated geomorphic process rates over the millennial time scale. The framework was applied to the Entle River catchment where the Schimbrig earthflow is located. We analysed the sediment cascade in terms of spatio-temporal patterns in denudation rates (L T^{-1}), and sediment fluxes (L^3 T^{-1}). The catchment-scale denudation rate quantifies the surface lowering per unit of time ($L\ T^{-1}$) and is scale-invariant. The sediment flux ($L^3\ T^{-1}$) is the volume of sediment material exported or evacuated from a given area per unit of time, and quantifies the rate of sediment transfer between landscape units, i.e. between hillslopes and channels. In addition, it enables us to track the internal sediment dynamics within a given catchment.

3. MATERIAL AND METHODS

3.1. THE ENTLE AND THE SCHIMBRIG CATCHMENTS

The Entle catchment is a 64 km² river catchment located in the northern foothills of the Central Swiss Alps, between Bern and Lucerne. Its elevation is ranging between 680 m at the outlet located near the Entlebuch village and 1,815 m a.s.l. on top of the Schimbrig summit. The study area lies on the intersection between the Swiss Plateau, i.e. the Molasse Basin, and the frontal thrusts of the Alpine orogeny (Schlunegger et al., 2016a). The Molasse layer, covering the lower reaches of the catchment is composed of Oligocene to Miocene conglomerate bedrock knobs, forming erosion-resistant low ridges. The intermediate part of the catchment is covered by subalpine Flysch, while the higher SW-NE-oriented ridge is composed of carbonate rocks (Figure 4.2). The Entle catchment is dissected by a 7 km-long central inner gorge with two tributaries, i.e. the Grosse and the Kleine Entle, that are deeply incised into a more than 100 m thick unconsolidated glacial till. The inner gorge contains knickzones in its longitudinal profile, and several cut terraces are visible. A ^{10}Be-based sediment budget highlighted that erosion rates in the inner gorge are more than 4 times higher than in the non-incised reaches over the last 2,000 years (Van den Berg et al., 2012). Therefore, the river system is supply-limited, and eroded sediments are efficiently transported to downstream reaches. Lateral and terminal moraines deposited by the Entle glacier during the Last Glacial Maximum (LGM) are present on both sides of the inner gorge, and in the headwaters of the Grosse and Kleine Entle rivers (Figure 4.2). The glacial till was deposited during repetitive and extensive glaciations during the Pleistocene. Sidewalls of river valleys are subject to widespread rotational and translational landslides. Flysch-covered areas are mainly affected by landslide processes categorized as earthflows.

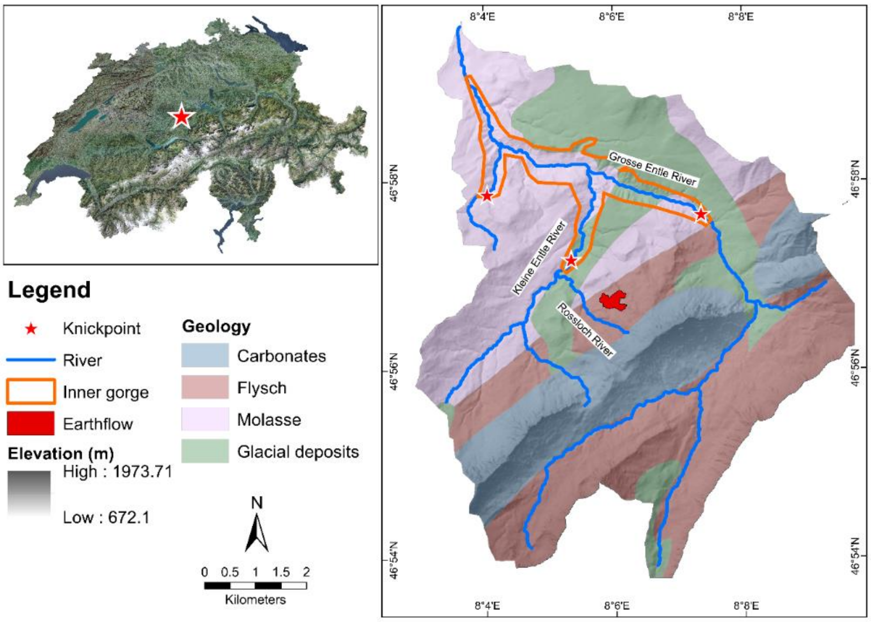

Figure 4.2: Simplified geological and geomorphological settings of the Entle river catchment (after Van den Berg et al., 2012; Schlunegger et al., 2016b). Inset: Location of the study area in Switzerland.

Within the Entle river catchment, the Schimbrig earthflow is particularly active over the last 150 years (*Chapter III*; Lopez-Saez et al., 2017; Savi et al., 2013; Schwab et al., 2008). It is located in the first-order Schimbrig catchment, the latter draining successively into the Rossloch River and the Kleine Entle, before entering the trunk river, i.e. the Grosse Entle. The earthflow occurs on the hillslopes of the Schimbrig ridge and is not physically connected to the Schimbrig stream, except during short episodes when superimposed debris flows occur. The Schimbrig earthflow consists of a fine-grained matrix of silt and mud, with centimetric to decimetric large clasts. The internal structure of the earthflow is complex with nested rotational units. Field observations revealed that a major earth slide with an up-to-12-m surface lowering occurred in the summer of 1994 after a succession of heavy precipitation events, followed by debris flows until March 1995 (Schwab et al., 2008). The intensity and spatial pattern of sediment redistribution, as well as the internal structure of the earthflow rapidly evolve at the annual and decadal scale (*Chapter III*).

3.2. ANNUAL SEDIMENT FLUXES

The annual sediment fluxes of the active part of the Schimbrig earthflow were derived from time series of very high-resolution topographic datasets from *Chapter III*. The 3D topographic reconstructions were computed using the structure-from-motion algorithm (SfM) based on aerial photographs acquired by an unmanned aerial vehicle (UAV). Point clouds were subsequently interpolated into digital surface models (DSM) at a spatial resolution of 0.04 m, defined based on the density of the point clouds. The accuracy of the time series is ranging between 0.20 m and 0.24 m. Acquisition dates are October 2013, June 2014 and October 2015. As part of this sediment flux assessment, only the dataset of the 2014-2015 time interval was used because it spatially covers the entire Schimbrig earthflow. The sediment budget was quantified by a digital elevation model of differences (DoD) between DSMs, using the Geomorphic Change Detection software (Wheaton et al., 2010). It spatially assesses surface *lowering*, i.e. decrease in ground elevation, and *bulging*, i.e. increase in ground elevation, within the earthflow. Subsequently, the net difference between the volume of landslide deposits, i.e. *bulging* and eroded material, i.e. *lowering*, gives a first estimate of the net flux of landslide-derived material that is evacuated between June 2014 and October 2015. In this chapter, values are eventually reported on an annual basis instead of over the entire period of interest (as in *Chapter III*). Detailed methodology and extended results are available in the *Chapter III*. Errors reported at the annual scale were computed based on a uniform limit-of-detection applied on each topographic surface. Therefore, the associated error to the annual sediment fluxes should be seen as a maximum value. It is likely that spatializing the error on very high-resolution topographic measurements would lead to an increase of the signal-to-noise ratio.

3.3. DECADAL SEDIMENT FLUXES

The sediment fluxes at decadal scale were derived from Schwab et al. (2008), who assessed sediment yields of the Schimbrig earthflow and associated slopes, i.e. the *Schimbrig catchment*, and linked it with sediment loads in the trunk stream, i.e. the *Waldemme River*. They based their analysis on a time series of DEMs derived from classic photogrammetry of aerial photographs acquired in 1962, 1986, 1993 and 1998. The associated volumetric errors of the photogrammetric workflow ranged between 2% for the 1986-1993 time interval and 29% for the 1962-1986 time interval. For this study, we converted the average sediment fluxes that were published in tons per year into cubic metre per year, using a material density of 2.70 g cm^{-3} following a study by Gong (2005) on similar flysch units in Switzerland. Detailed methodology and results are available in the original paper of Schwab et al. (2008).

3.4. MILLENIAL SEDIMENT FLUXES

The geomorphic process rates at millennial scale were assessed from catchment-averaged denudation rates derived from *in-situ* produced cosmogenic radionuclides in river-borne sediments. In order to get a comprehensive dataset on spatial variation in denudation rate in the Entle catchment, we collected river sand on eight locations in and around the Schimbrig catchment (Figure 4.3) and combined them with earlier work by Van den Berg et al. (2010). The new samples were processed in a similar way as the sample preparation and processing described in Vanacker et al. (2007) and are similar to Van den Berg et al. (2010). After washing and sieving to the 0.25-1.00 mm fraction size, grains were separated using a Frantz Isodynamic Magnetic Separator. The remaining non-magnetic fraction was leached several times with 10% hydrochloric acid to remove organic, calcium and carbonate components. Then, samples were treated up to four times with 5% hydrofluoric acid in order to dissolve anything but quartz and also remove any meteoric ^{10}Be left. After the leaching step, 157.8 µg of ^{9}Be carrier was added to the clean quartz samples containing ca. 25 g of material. The purified quartz was subsequently dissolved in concentrated HF, from which beryllium is stepwise extracted using anion/cation exchange column chemistry. Remaining precipitates were oxidized and pressed into copper targets. Finally, $^{10}Be/^{9}Be$ ratios were quantified using the 500 kV Tandy facility at ETH Zürich (Christl et al., 2013). These values were normalized with the in-house standard SN2007N and corrected with a blank $^{10}Be/^{9}Be$ ratio of $4.06 \pm 0.23 \times 10^{-15}$. Catchment-wide denudation rates were then computed from the in-situ produced ^{10}Be concentrations, i.e. from this study and from earlier data published by Van den Berg et al. (2010), using the catchment-averaged denudation rates from cosmogenic nuclide (CAIRN) method (Mudd et al., 2016). This open source calculator uses the topography to weight the ^{10}Be production rate and shielding. A 1-metre digital terrain model (DTM) resampled to 30 m resolution was used to compute topographic shielding. Snow shielding was averaged for each catchment individually. Snow cover is estimated using an elevation-dependent mean annual snow cover database for Switzerland (Auer, 2003). Following Jonas et al. (2009), an empirical relationship is used to derive the snow water equivalent thickness (SWE, g cm^2).We kept the default parameters from Mudd et al. (2016) to run the CAIRN model, including the sea-level high-latitude production rate of 4.30 at g^{-1} yr^{-1} (based on Braucher et al., 2011). Long-term denudation rates obtained by the CAIRN calculator were converted into sediment fluxes (m^3 yr^{-1}), by multiplying them with the catchment area.

4. RESULTS

4.1. SCHIMBRIG EARTHFLOW SEDIMENT DYNAMICS AT THE ANNUAL SCALE

When focusing on the unstable part of Schimbrig earthflow, we obtained a net mass flux of 1,350 ± 4,314 m^3 yr^{-1} for the 2014-2015 period (Table 4.1; *Chapter III*). Although this value is slightly positive, the mass flux is not significantly different from zero. The sediment budget for the 2013-2014 time interval supports this finding. In the eroding sites, the average denudation was 0.773 ± 0.210 m yr^{-1}, and smaller than the accumulation of 0.787 ± 0.210 m yr^{-1} that was observed in the bulging areas (Table 4.1). For the Schimbrig earthflow, we reported a mean horizontal displacement of ca. 6.30 m yr^{-1} in the downslope direction (Table 3.5 in *Chapter III*). The UAV-

SfM derived data suggest that the earthflow was in dynamic equilibrium over the 2014-2015 period, with landslide-derived material being temporarily stored on the slopes during the period of interest.

Table 4.1: Sediment fluxes for the 2014-2015 time interval from the Schimbrig earthflow (Modified from Table 3.4 in *Chapter III*, to provide sediment fluxes reported on an annual basis).

	Estimate	Error (±)
Total area of surface bulging ($m^2\ yr^{-1}$)	10763	-
Total area of surface lowering ($m^2\ yr^{-1}$)	9730	-
Average depth of surface bulging ($m\ yr^{-1}$)	0.787	0.210
Average depth of surface lowering ($m\ yr^{-1}$)	0.773	0.210
Average net depth of difference ($m\ yr^{-1}$)	0.046	0.149
Sediment flux ($m^3\ yr^{-1}$)	1350	4314

Notwithstanding the state of dynamic equilibrium, our data suggest large internal movements with a complex pattern of sediment redistribution along slope (Figure 3.9 in *Chapter III*). A succession of areas with terrain lowering and bulging characterised the earthflow along its longitudinal axis. The earthflow was re-adjusting to a new state of equilibrium after a massive failure that occurred in 1994. The sediment redistribution on the slopes was not associated with an increased sediment export downstream. Between 2013 and 2015, the hillslope domain was disconnected from the fluvial domain.

4.2. SEDIMENT BUDGET OF THE SCHIMBRIG CATCHMENT AT DECADAL SCALE

Sediment fluxes were computed from 1962 to 1998 over the first-order catchment affected by the earthflow, down to the confluence with the Rossloch River (Table 4.2; Schwab et al., 2008). The average sediment flux per year, evacuated from the catchment, is varying over time, from 4,000 ± 4,000 $m^3\ yr^{-1}$ for the 1962-1986 period, to 850 ± 20 $m^3\ yr^{-1}$ for 1986-1993 to 24,000 ± 4,000 $m^3\ yr^{-1}$ for the 1993-1998 time interval. The data from Schwab et al. (2008) indicate that there is no clear link between the sediment fluxes exported from the Schimbrig catchment and the landslide dynamics on the hillslopes. This is evident from the fact that the proportion of the mass evacuated from the study area to the total displaced mass varies largely between 6% and 89% (Table 4.2).

Table 4.2: Sediment fluxes between 1962 and 1998 (after Schwab et al., 2008).

Time interval	Average sediment flux evacuated (m^3 yr^{-1})	Error Sediment flux (m^3 yr^{-1})	Percentage of mass evacuated compared to the displaced mass (%)
1962-1986	14,000	4,000	89
1986-1993	850	20	6
1993-1998	24,000	4,000	34
1962-1998	13,000	2,000	78

During the 1962-1986 period, about 89% of the displaced mass was evacuated from the catchment, suggesting that sediment storage during this period was not significant. In contrast, during the following periods (1989-1993, 1993-1998) when the major earthflow event occurred in 1994, only 34% of the landslide material was evacuated.

4.3. LONG-TERM DENUDATION RATES OF THE ENTLE CATCHMENT

Overall, the CRN-derived denudation rates (Table 4.3; Van den Berg et al., 2010) ranged from 160 ± 30 mm kyr^{-1} in the upper part of the Entle catchment, i.e. the Rothbach River (*E-9*), and 5000 ± 1000 mm kyr^{-1} in the upper part of the Schimbrig earthflow (*CH-ENT-3*). Importantly, measurements from Van den Berg et al. (2010) and from this study are spatially and quantitatively consistent with each other (Figure 4.3). As the ^{10}Be concentrations of the landslide-affected area were low, relatively high errors were reported for the ^{10}Be concentrations of landslide-derived sediment material (Table 4.3). The errors subsequently propagated on the denudation rates, particularly for the samples from the Schimbrig stream draining the earthflow, i.e. *CH-ENT-1*, *CH-ENT-5* and *CH-ENT-8*.

Our data show two opposite patterns of denudation rates and sediment fluxes in relation to drainage area and downstream distance, which are driven by the landslide occurrence (Table 4.3; Figure 4.4; Figure 4.5).

Table 4.1: Denudation rates and sediment fluxes for the Schimbrig catchment and other first-order rivers, i.e. samples *CH-ENT-, from this study and re-computed denudation rates and sediment fluxes for the Entle River catchment, i.e. samples *Ent** and *E-**, from Van den Berg et al. (2010).**

Sample	Drainage area (km^2)	Altitude (m)	Latitude (dd)	Longitude (dd)	^{10}Be concentration ($\times 10^3$ at g^{-1})	Production scaling	Topographic shielding	Snow shielding	Denudation rate (mm kyr^{-1})	Sediment flux (m^3 yr^{-1})
CH-ENT-1	0.20	1451	46.945	8.098	0.62 ± 0.45	3.306	0.954	0.904	1000 ± 2000	300 ± 400
CH-ENT-2	1.96	1264	46.951	8.086	2.94 ± 0.28	2.965	0.974	0.917	260 ± 60	500 ± 100
CH-ENT-3	0.16	1500	46.943	8.104	0.15 ± 0.53	3.427	0.937	0.900	5000 ± 1000	900 ± 200
CH-ENT-5	0.35	1373	46.946	8.097	2.32 ± 0.58	3.208	0.961	0.909	300 ± 100	120 ± 40
CH-ENT-6	3.25	1306	46.942	8.077	4.12 ± 0.28	3.069	0.950	0.914	180 ± 40	600 ± 100
CH-ENT-7	4.54	1336	46.942	8.076	2.57 ± 0.27	3.112	0.960	0.912	300 ± 70	1400 ± 300
CH-ENT-8	0.51	1325	46.947	8.092	1.34 ± 0.27	3.033	0.970	0.913	600 ± 200	290 ± 80
CH-ENT-9	1.07	1287	46.946	8.092	3.53 ± 0.28	2.983	0.977	0.915	210 ± 50	230 ± 50
Ent3-1	3.32	1076	46.956	8.062	1.94 ± 0.11	2.434	0.979	0.954	340 ± 70	1100 ± 200
Ent4-1	54.60	1323	46.937	8.105	2.43 ± 0.12	3.007	0.965	0.948	320 ± 70	17000 ± 4000
E-5	26.53	1482	46.924	8.116	3.11 ± 0.17	3.357	0.956	0.937	270 ± 60	7000 ± 1000
E-7a	63.56	1274	46.941	8.100	2.46 ± 0.13	2.922	0.967	0.951	310 ± 60	20000 ± 4000
E-8	8.05	1547	46.907	8.107	4.60 ± 0.24	3.635	0.959	0.933	200 ± 40	1600 ± 300
E-9	7.83	1537	46.916	8.088	5.28 ± 0.26	3.369	0.967	0.933	160 ± 30	1300 ± 300
E-10	3.13	1445	46.942	8.153	4.70 ± 0.21	3.326	0.975	0.935	180 ± 40	600 ± 100
E-11	16.01	1231	46.939	8.081	2.27 ± 0.13	2.871	0.969	0.949	330 ± 70	5000 ± 1000
E-12	11.71	1280	46.934	8.076	3.53 ± 0.25	2.989	0.964	0.946	220 ± 50	2500 ± 500
E-13	16.64	1534	46.913	8.099	5.22 ± 0.24	3.511	0.960	0.934	170 ± 30	2800 ± 600

Ignoring samples from landslide-affected catchments, long-term denudation rates correlate positively with downstream distance, with values ranging from 160 ± 30 mm kyr^{-1} (*E-9*) to 340 ± 70 mm kyr^{-1} (*Ent3-1*). Characterised by a low variability, these values are similar to other denudation rates found in the similar alpine tectonic settings (e.g. Norton et al., 2008).

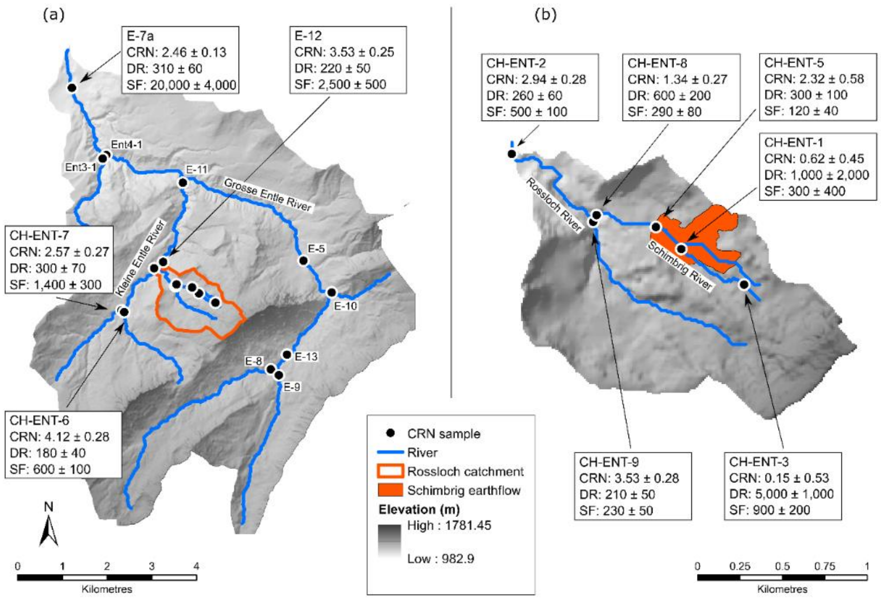

Figure 4.3: Location of CRN samples in the Entle catchment. CRN concentrations (CRN; ×10^3 at g^{-1}), denudation rates (DR; mm kyr^{-1}) and sediment fluxes (SF; m^3 yr^{-1}) values displayed are discussed in the text. Other values are available in (Table 4.3). (a) Entle River and (b) Rossloch River catchments.

This increase in denudation rates with downstream distance is triggered by the ongoing relief rejuvenation and incision of the inner gorge after the LGM (Van den Berg et al., 2012). The data also indicate that the river network effectively evacuates sediments that are supplied to the river channel. Accounting for the drainage area at each sample location, long-term sediment fluxes (Table 4.3; Figure 4.5) show the same positive correlation with downstream distance as denudation rates. The sediment fluxes range from 600 ± 100 m^3 yr^{-1} in upper first-order catchments (*CH-ENT-6* and

E-10) to 20,000 ± 4,000 mm kyr^{-1} at the outlet of the Grosse Entle River (*E-7a*). This two-order-of-magnitude increase in sediment fluxes downstream corroborates the efficiency of sediment evacuation by the fluvial system.

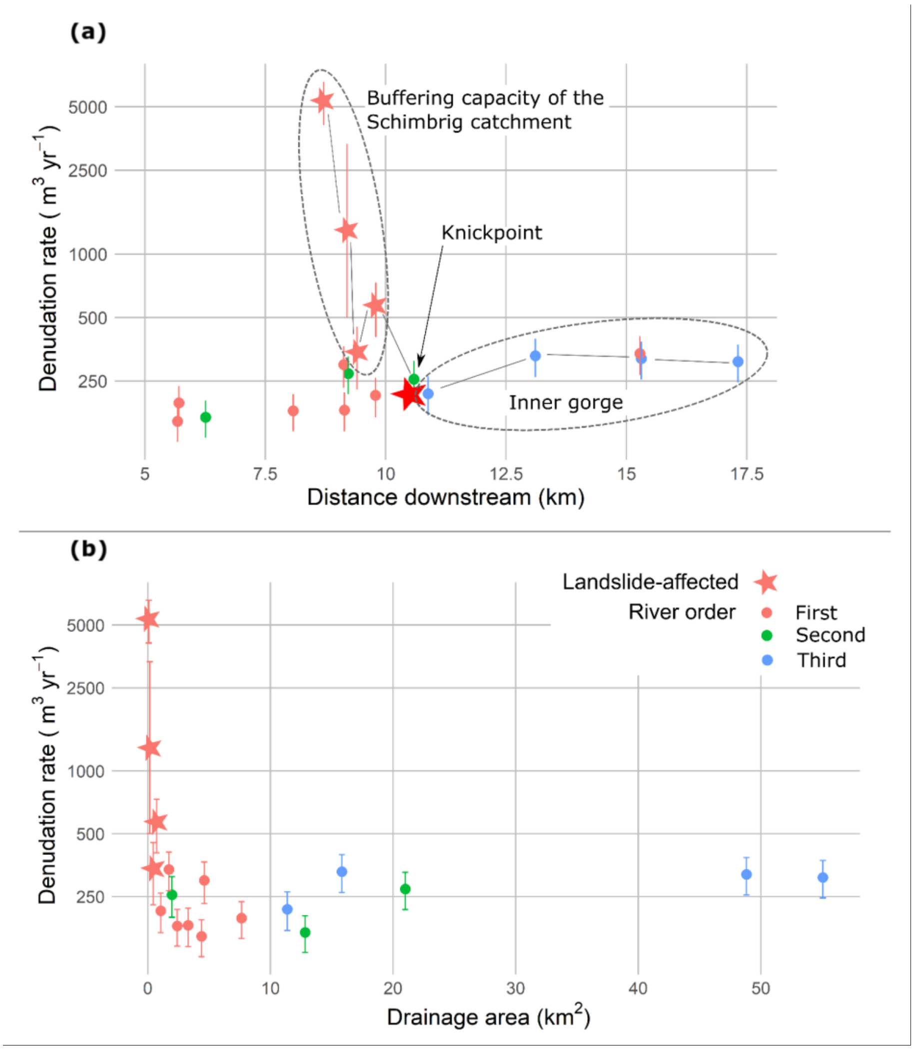

Figure 4.4: Denudation rates in the Entle catchment against (a) downstream distance and (b) drainage area. Downstream distance is computed from river source to outlet of the Entle catchment. Marker *star* represents CRN-derived denudation rate from the landslide-affected Schimbrig catchment. Grey line presents the downstream sequence of denudation rates along the Schimbrig, Rossloch, Kleine Entle and Grosse Entle rivers.

The landslide-affected catchments show a different pattern that deviates from the overall trend of increasing denudation rates with distance downstream and catchment area. In the first-order Schimbrig catchment, long-term denudation rates correlate negatively with downstream distance (Table 4.3; Figure 4.4).

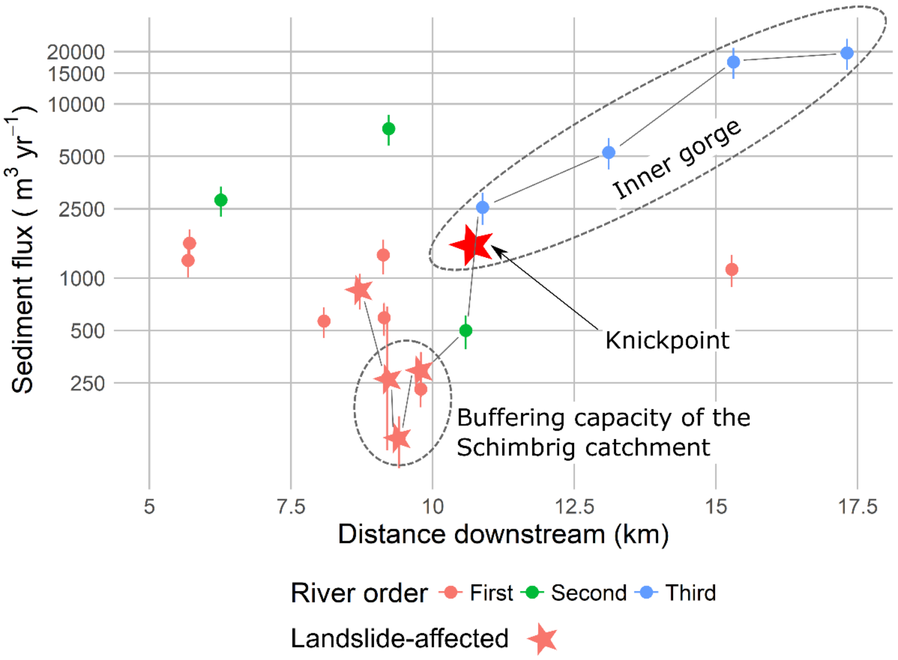

Figure 4.5: Sediment fluxes along the river network of the Entle catchment. Downstream distance is computed from river source to outlet of the Entle catchment. Marker *star* represents sediment flux from the landslide-affected Schimbrig catchment. Grey line presents the downstream sequence of denudation rates along the Schimbrig, Rossloch, Kleine Entle and Grosse Entle rivers.

The denudation rates of the landslide-affected first-order catchment are up-to one order of magnitude higher than the rest of the Entle catchment, with values ranging between 300 ± 100 mm kyr^{-1} in the intermediate part (*CH-ENT-5*) and 5,000 ± 1,000 mm kyr^{-1} (*CH-ENT-3*) in the upper part of the Schimbrig catchment. The variability in denudation rates along the river is very high, with a one-order of magnitude difference between minimum and maximum values, and spatially highly variable. For example, the denudation rate in *CH-ENT-5* is lower than the sites directly up- and down-stream of this sampling location, reflecting the stochastic character of the sediment delivery from the earthflow. The decrease in denudation rates with catchment area suggests that material initially displaced by the earthflow is not directly evacuated to the river network but remains on the slopes, hence accumulating ^{10}Be atoms in sediments.

Given that the catchment area of the first-order landslide-affected catchments is small, the absolute sediment fluxes are low with values ranging between 120 ± 40 m³ yr^{-1} and 900 ± 200 m³ yr^{-1}. These long-term sediment fluxes computed for the Rossloch catchment, i.e. including the Schimbrig area, are one to two orders of magnitude lower than values computed in other parts of the Entle catchment (Figure 4.5).

The impact of landsliding on the long-term sediment dynamics can be evaluated by comparing the denudation rates of the two intersecting catchments at the confluence with the Rossloch river. At the outlet of the Schimbrig catchment, the denudation rate, i.e. 600 ± 200 mm kyr^{-1} (*CH-ENT-8*), is at least two times higher than in the neighbouring catchment, i.e. 210 ± 50 mm kyr^{-1} (*CH-ENT-9*). When accounting for their catchment area, the sediment fluxes are very similar with values of respectively 290 ± 80 m³ yr^{-1} (*CH-ENT-8*) and 230 ± 50 m³ yr^{-1} (*CH-ENT-9*).

5. DISCUSSION

The sediment transfer between the hillslope and fluvial domain controls the propagation of episodic sediment pulses from stochastic hillslope processes to the river channels. Mechanisms and scales of hillslope-channel connectivity are still poorly assessed (e.g. Bracken et al., 2015; Fryirs, 2013; Heckmann and Schwanghart, 2013; Korup et al., 2010). Our conceptual framework (see *Section 2*; Figure 4.1) depicts the patterns of geomorphic connectivity between distinct units of the landscape and their characteristics, i.e. hillslopes and channels, as well as sediment pulse propagation through space and time. We applied this framework on the Entle catchment located in the foothills of the Central Swiss Alps, by quantifying sediment fluxes over 10^0-10^3 years. Characterised by a relatively gentle alpine topography, the millennial geomorphic activity of the study area is moderate in intensity. In comparison, the mean CRN-derived denudation rate is 270 ± 140 mm kyr^{-1} in similar surrounding areas, i.e. in the Alpine foreland but increases to 900 ± 300 mm kyr^{-1} in the high crystalline Alps (Wittmann et al., 2007). The Entle River catchment was affected by an active earthflow over the last 150 years. Given the extent of its active part, i.e. ca. 0.5 km², the Schimbrig earthflow is a larger than average landslide (Stark and Hovius, 2001). Therefore, according to the magnitude-frequency distribution of landslides (e.g. Hovius et al., 1997), this type of occurrence is generally relatively infrequent, i.e. between 10^{-2} km^{-2} yr^{-1} and 10^{-3} km^{-2} yr^{-1}. The mean annual horizontal displacements that we measured within the earthflow, i.e. ca. 6.30 m yr^{-1} for the period 2014-2015, are high in comparison with the decimetric displacements reported in the Western Slovakian Carpathians (Prokešová et al., 2014), < 2 m yr^{-1} for the Eel earthflow in California (Mackey et al., 2009), and metric to decametric displacements for the Super-Sauze landslide in Southern French Alps (Niethammer et al., 2012).

At the annual scale, the Schimbrig earthflow experienced intense sediment redistribution, with a mean horizontal surface displacement of more than 6 m yr^{-1}. The sediment budget of the Schimbrig earthflow is roughly in equilibrium, with very limited sediment evacuation from the hillslope domain to the fluvial domain. Consequently, it implies that the Schimbrig earthflow was not coupled to the channel network for the period 2013-2015. Back to the conceptual framework, this result supports the idea that landslide processes act as stochastic sediment pulses, producing sediments on hillslopes in the landscape. Their impact is attenuated as follows over short time scales: (1) After the principal slope failure, only a small fraction of the mobilised sediment volume is exported to the river network. (2) Subsequently, the internal sediment reorganisation on the hillslopes results in very dynamic topography with very limited sediment evacuation to the channels.

Hence, at the decadal scale, sediment fluxes computed over the entire Schimbrig catchment support the episodic pattern of connection/disconnection between hillslopes and channels. Sediment transfer of landslide colluvial fans to the river network only occurs by superimposed stochastic debris flows, the latter being the main mechanisms of hillslope-channel coupling. Schwab et al. (2008) suggested that this pattern occurs at the decadal scale. They showed that intense geomorphic activity within the Schimbrig catchment is not associated with phases of increased sediment export to the channel network, and resulted in storage of landslide-derived debris on the hillslopes even during extended or intense rainfall episodes. For instance, the large slope failure of 1994, which lowered the ground surface up to 12 m, produced fresh sediments that was temporarily stored as colluvial material on the hillslopes instead of being directly transported to the river network. In contrast, phases of lower hillslope geomorphic activity were coinciding with higher sediment export to the river channel and evacuation of landslide-debris from the hillslope to the fluvial domain. During these periods, mobilised sediments by previous landslides are gradually and/or episodically transported downstream.

At the millennial scale, catchment-wide denudation rates show a positive relationship with downstream distance and drainage area, if landslide-affected catchments are ignored. The latter are characterised by a negative relationship with downstream distance, along with a high variability. Interestingly, the large difference in denudation rates between the Schimbrig (*CH-ENT-8*) and upper Rossloch (*CH-ENT-9*) catchments indicates that the sediment dynamics of both catchments were very different over the last thousands of years. The high variability of denudation rates in headwaters (Figure 4.4a) emphasizes the episodic character of landslides. When accounting for the surface area of the catchments, the difference between the two adjacent streams disappears. As such, the landslide-affected Schimbrig catchment only has a small impact on the overall sediment budget of the Entle River catchment.

In addition to the hillslope-channel connectivity, our database of sediment fluxes also highlights the non-steady character of geomorphic processes. The average decadal sediment flux of the Schimbrig catchment, i.e. 13,000 ± 2,000 $m^3\ yr^{-1}$ between 1962 and 1998 (Table 4.2), is in fact two orders of magnitude higher than sediment fluxes computed at the millennial time scale over the same spatial extent, i.e. 290 ± 80 $m^3\ yr^{-1}$ (*CH-ENT-8*). In other words, the decadal sediment flux is not representative for the long-term, millennial sediment flux of the first-order river catchments (Figure 4.6).

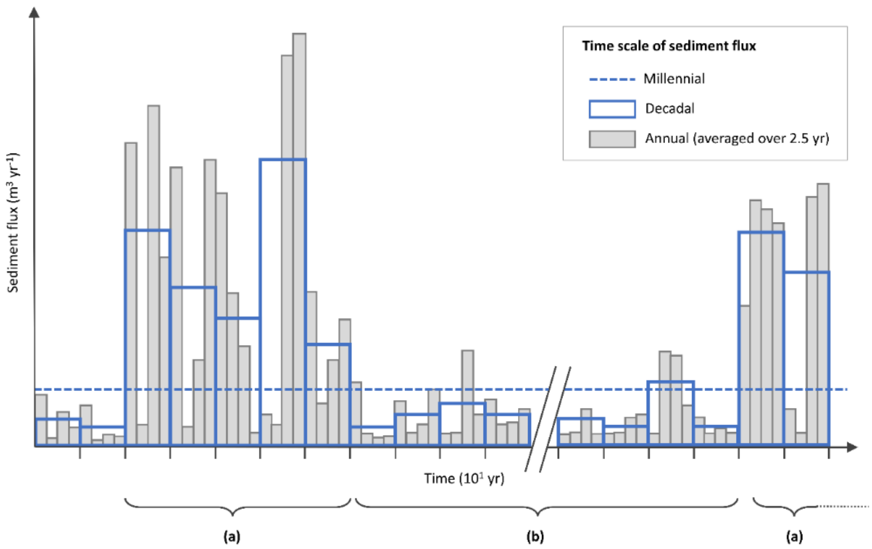

Figure 4.6: Conceptual representation of the sediment fluxes over different time scales at the outlet of a first-order river catchment. (a) Periods of high hillslope activity due to a landslide sediment pulse, resulting in intermittent hillslope-channel connections and in sediment export to the river network at the annual scale. (b) Periods of low hillslope activity both at the annual and decadal scales, due to poor sediment availability on slopes.

Taking benefit of our multi-temporal database, the mismatch between annual, decadal and millennial sediment fluxes is probably caused by the episodic character of sediment fluxes over long time scales. Since the oldest photogrammetric dataset, i.e. 1962, the Schimbrig catchment experienced active landsliding. Dendrogeomorphological data confirmed that slope movements were taking place over the last > 150 years (Lopez-Saez et al., 2017; Savi et al., 2013). However, all other parameters remaining equal, our data suggest that this situation is temporary, and was preceded by a long phase of inactivity. The transient character of the important geomorphic activity in the Schimbrig catchment, i.e. a first-order river, is eventually supported by following observation: its decadal sediment flux, i.e. 13,000 ± 2,000 m^3 yr^{-1} (Table 4.2), is of the same order of magnitude than the background sediment flux going out of the entire Entle River catchment, i.e. 20,000 ± 4,000 m^3 yr^{-1} (*E-7a*; Table 4.3). In other words, it means that over the last 50 years, the Schimbrig catchment, which represent ca. 1% of the entire study area, provides 65 % of the sediments that the entire Entle catchment will supply by over the millennial scale. Subsequently, sediment transport will attenuate the huge sediment pulse from the Schimbrig to the outlet of the Entle catchment. Consequently, the impact of the Schimbrig earthflow is currently important with respect to the rest of the Entle catchment, after an initial major slope failure more than 150 years ago. The higher-order river network, i.e. the Kleine and Grosse Entle rivers, attenuates decadal sediment pulses by sediment transport, during which subsequent erosion and deposition occur over longer time scales. In the future, the slopes of the Schimbrig will find a new equilibrium after the on-going landslide perturbation, leading to a lower geomorphic activity. The final state of equilibrium will be reached when the entire volume of sediments mobilised by the initial failure and its reactivations will be depleted from the hillslope. Somehow, due to the stochastic character of landslides, a new sediment pulse will affect another sub-catchment of the Entle area, inducing a new cycle. Back to our conceptual framework, landslides affecting hillslopes over short time scales are in fact considered as noise over long time scales. They trigger localised sediment pulses, which are subsequently shredded by sediment transport when reaching the channel network. This noise is eventually averaged out when considering longer time scales and larger spatial scales. Consequently, one single landslide has not necessarily an impact on the long-term sediment budget of first-order catchments. Rather, it is the cumulated effect of multiple landslides which are intermittently connected to the channel network at the decadal scale, along with sediment transport, that may regulate sediment fluxes at the regional scale over the millennial time scale.

6. CONCLUSION

To better understand mechanisms and scales of geomorphic connectivity in mountainous environments, we characterised the sediment cascade of the Entle River catchment located in the foothills of the Central Swiss Alps. We quantified (or took benefit from previous studies of) sediment fluxes over annual, decadal and millennial time scales using respectively UAV-SfM-based 3D topographic reconstructions, classic photogrammetry and in-situ ^{10}Be cosmogenic radionuclides.

Our database of sediment fluxes supported three hypotheses about the dynamics of the sediment cascade in first-order catchments and the dynamic feedback between hillslopes and channels: (1) In the landscape, landslides act as local sediment pulses, making them available for further mobilisation and transport when hillslopes and channels are connected. (2) Connection/disconnection cycles occur at the decadal scale. (3) High decadal geomorphic activity at the catchment scale is episodic over the millennial temporal scale. At the annual scale (2013-2015), the mass balance of the Schimbrig earthflow is in equilibrium despite the intense sediment redistribution on hillslopes, which indicates that the latter is disconnected from the channel network. Hillslope-channel connection occurs at the decadal scale (1962-1998) during stochastic rainfall-triggered superimposed debris flows, causing sediment supply to the river network. At the millennial scale, higher-than-average long-term denudation rates characterise the intense geomorphic activity of the Schimbrig catchment. However, the high-magnitude low-frequency character of the Schimbrig earthflow implies that it does not affect the long-term sediment flux pattern. In addition, nothwithstanding the intense sediment activity of the Schimbrig earthflow at the decadal scale, it only affects a small first-order river catchment.

Our data highlight the episodic character of sediment fluxes from first-order river catchments in alpine environments and the attenuation of sediment pulses by sediment transport throughout landscapes. Landslides act as stochastic but discrete sediment sources in the landscape and randomly affect these catchments. During short periods occurring at the decadal scale, when hillslopes geomorphically connect to channels, the sediment flux of the Schimbrig catchment is of the same order of magnitude than the total sediment flux of the Entle catchment. This implies that during these short phases of connection, more than 65 % of the sediment is coming from 1 % of the total catchment area. However, during 90 % of time, hillslope-channel system of the first-order catchment is uncoupled from the lower reaches at the regional scale.

When the sediment source will be depleted, another first-order river catchment will be affected by landslides and will provide enough sediments to match the long-term regional sediment flux. Consequently, one single landslide has not necessarily an impact on the long-term sediment budget of mountainous river catchments at the regional scale. It is the integrated effect of multiple sediment pulses providing sediments to the river network at the decadal scale, which are subsequently attenuated by sediment transport that may regulate sediment fluxes at the regional scale.

CHAPTER 5

MODEL-BASED ASSESSMENT OF THE STOCHASTIC EFFECT OF LANDSLIDES ON COSMOGENICALLY-DERIVED CATCHMENT-AVERAGED DENUDATION RATES

ABSTRACT

In-situ cosmogenic radionuclides (CRN) have become a widely used tool in the geomorphic community to constrain geomorphic process rates. In many applications, catchment-wide denudation rates have been derived from ^{10}Be concentrations in samples of river sand. These applications assume that sediment production and delivery rates within the catchment are reasonably steady and that river sediment is well mixed and all parts of the catchment are represented in proportion to their denudation rates. These assumptions are not necessarily met in active mountain ranges where deep-seated landslides or gully systems are contributing with deeply shielded material to the river network. In this study, we analyse how the impact of these geomorphic events on the CRN-derived denudation rates depends on their magnitude and frequency. We modified the CRN dynamics model of Yanites et al. (2009) to represent landslides as a proper spatial Poisson process and then adapted the code for an open-source programming language, i.e. R. Then, we performed 100 iterations of 24 scenarios exploring landslide-induced variability on CRN-derived denudation rates. Scenarios are depicting landscape and landslide configurations, according to the following variables: drainage area, background

erosion rate, landslide area distribution coefficient and landslide return period. Our results show that the variability of CRN-derived denudation rates, after a time span of 200,000 yr, is strongly driven by the landslide area distribution coefficient and the landslide return period. Background erosion rate, i.e. rate of gradual diffusion-like hillslope processes, also plays a role to reduce the landslide effect on CRN surface and river sediment concentrations. In addition, and more importantly, these parameters also influence the overestimation of CRN-derived erosion compared to actual volumetrically-derived erosion rates. Consequently, we suggest that CRN-derived erosion rates may not be properly representative of the actual erosion in landscapes where landslides act as a dominant erosion process, especially under conditions where the background erosion is significantly lower than landslide erosion.

1. INTRODUCTION

An accurate assessment of Earth's surface changes in active landscapes is crucial to properly understand how geomorphic processes are driving long-term landscape evolution (e.g. Bishop, 2007). Over the last two decades, catchment-averaged denudation rates are increasingly quantified using in-situ cosmogenic radionuclides (CRN), such as ^{10}Be in quartz minerals (e.g. Bierman and Nichols, 2004; von Blanckenburg, 2005; Portenga and Bierman, 2011). These denudation rates average over time scales of 10^3 to 10^5 years (Dunai, 2010). To apply this technique at the catchment scale, two basic assumptions are used (Brown et al., 1995; Dunai, 2010; Granger and Riebe, 2003). (1) A secular equilibrium exists between the production of CRN and the loss by erosion and decay. (2) The river sediment samples are sufficiently well mixed and all parts of the catchment are represented in proportion to their denudation rates. If these assumptions are met, the ^{10}Be isotope concentration measured in river sediments at the outlet of a catchment is inversely proportional to its denudation rate.

Any variation in sediment mixing capacity or delivery from deeply shielded sediment to the river channel, may dilute or increase the concentration in ^{10}Be in river sediments and lead to over- or under-estimation of the catchment-averaged denudation rates. The sediment mixing capacity of the river network can be very efficient and take place over short distances (Binnie et al., 2006). Episodic sediment input from e.g. landslides can disturb proper sediment mixing and ^{10}Be concentrations in river sediments (Kober et al., 2012; Vassallo et al., 2011). Empirical data show that the spatial and temporal variability of CRN concentrations are controlled by catchment area and magnitude-frequency of landslides (Savi et al., 2014; West et al., 2014). Moreover, landslides potentially dilute ^{10}Be concentrations if they are deep enough to bring *shielded* sediments from below the mixed layer, i.e. material characterised by a low ^{10}Be concentration, to the surface (Granger and Riebe, 2003; West et al., 2014).

Theoretical numerical models confirm that the river capacity to attenuate sediment pulses in both space and time varies according to the catchment area and the geomorphic setting (Niemi et al., 2005; Yanites et al., 2009). More recently, Dingle et al. (2018) explored the sensitivity of ^{10}Be concentrations in river sediments to a range of erosion scenarios that may drive variability. They used a simple numerical model to explore the impact of a single landslide on the ^{10}Be concentrations in river sediment. Interestingly, by comparing their numerical findings to empirical data from the Himalaya, they showed that various erosion scenarios can lead to comparable mean ^{10}Be concentrations in river sediments. This shows that equifinality can be an issue when interpreting denudation rates, in landscapes where landslides affect the CRN signal (e.g. Savi et al., 2014). Besides, the stochastic character of landslides also drives the variability in ^{10}Be concentrations in river sediments. By chance, landslides may provide (1) more or (2) less sediments than the average delivery over a given time period, determined by their typical magnitude-frequency distribution. This variability in turn influences the cosmogenically-derived denudation rates. However, the stochastic effect of mass-wasting processes on ^{10}Be concentrations is still poorly constrained, and needs further attention to properly guide CRN field campaigns and increase knowledge.

Previous modelling studies focused on temporal evolution of ^{10}Be concentrations across landscapes (Niemi et al., 2005; Yanites et al., 2009) and explored the relation between CRN-derived denudation rates and landscape characteristics such as the total erosion rate, landslide erosion rate, landslide area distribution exponent, landslide return period, catchment order or area. Both modelling studies performed one simulation per landscape configuration, given a magnitude-frequency distribution characterising landslides. However, landslides are stochastic events with respect to their magnitude and spatial occurrence. The magnitude-frequency distribution is typically following an inverse gamma function (e.g. Hurst et al., 2013; Malamud et al., 2004) while their spatial occurrence is assumed to follow a Poisson probability distribution (Corominas and Moya, 2008; Guzzetti et al., 2005). Consequently, we expect that for some landscape/landslide configurations, iterating the numerical model for a statistically relevant number of times, will induce variability in the final CRN-derived denudation rates. The aim of our study is therefore to identify the parameters of landslide occurrence and landscape configuration that could induce (1) a stochastic effect on CRN-derived denudation rates and (2) an overestimation of CRN-derived denudation rates compared to actual volumetrically-derived erosion rates. First, we further developed the model of Yanites et al. (2009) in order to (1) generate landslides as a random Poisson process point pattern over the entire modelled catchment at each time step, (2) optimised the computation efficiency of the model, and (3) adapted the code for free software environment, i.e. R. Then, we iterated the model one hundred times for various landscape/landslide configurations to assess the stochastic effect of landslides on computed values of CRN-derived denudation rates.

2. PREVIOUS WORK

Despite the recognized importance of the research question, only two independent theoretical studies exist about CRN dynamics in landslide-prone catchments, using spatially-explicit modelling. Niemi et al. (2005) modelled the CRN dynamics of 46 sub-catchments of the San Antonio Creek catchment, located in the eastern San Gabriel Mountains in southern California. They implemented nine different scenarios, varying the bedrock weathering rate, i.e. background erosion rate, and the total erosion rate, to reach a prescribed landslide erosion rate. Volumetrically- and cosmogenically-derived erosion rates were quantified for each sub-catchment order and compared to the total erosion rate. The main advantages of their approach are that (1) the CRN surface production rates are scaled for the sea-level high-latitude production rate and spatially distributed using a digital elevation model (DEM) of the area, and (2) the study area is divided into the actual extent of sub-catchments. However, even though the model time step used, i.e. 100 years, intrinsically allows a certain mixing regime, sediment storage and mixing capacity of catchments are not explicitly considered. Consequently, all eroded material is evacuated from the system after each time step. Following the same approach and governing equations than Niemi et al. (2005), Yanites et al. (2009) modelled the CRN dynamics for a synthetic catchment. They explored a wide range of model parameter combinations and implemented more than 800 different scenarios in total, varying drainage area, landslide characteristics and background erosion rate. Importantly, with a time step of one year, their model includes the sediment mixing and storage capacity of the fluvial network. However, sediment storage is only considered within the fluvial network and not on hillslopes. Consequently, sediment routing for landslides that do not directly enter the fluvial network is ignored. Moreover, inherently to the implementation of an idealized landscape, the CRN surface production rate is constant and the delineation of actual catchments is not possible.

3. MODELLING OF CRN DYNAMICS

Our implementation of a model quantifying the CRN dynamics in landslide-prone landscape is based on the work of Yanites et al. (2009). We used the model code, i.e. Cosmoland, available on the GitHub repository of the Community Surface Dynamics Modeling System (CSDMS) project (CSDMS, 2011), as our starting point. The original version has been improved to meet both our technical and theoretical needs. Technically, the original script, written in the proprietary programming language MATLAB, was adapted to the free and open-source software environment R. In addition, improved input and output management, automation for model iteration and parallel processing were implemented to reduce the model computation time and hence the efficiency of analysing multiple model runs. To address our theoretical objectives, landslides were generated at each time step following a homogeneous Poisson process over the entire catchment area (Corominas and Moya, 2008; Guzzetti et al., 2005).

To explore the stochastic effect of landslides on CRN dynamics, we iterated the model 100 times for 24 different scenarios. Each scenario represent one landscape and landslide configuration, characterised by four parameters: drainage area, background erosion rate, landslide area distribution coefficient and landslide return period. We discussed the model output in terms of the variability of the following model outputs: (1) cosmogenically-derived erosion rate and (2) the volumetrically-derived erosion rate. For the sake of brevity further in the text of this chapter, the term *scenario* is used to describe landscape/landslide configurations. Moreover, we refer to CRN-derived denudation rates as CRN-derived erosion rates. They include mass losses by physical erosion and chemical weathering.

3.1. MODEL IMPLEMENTATION

The CRN dynamics is numerically modelled for a hypothetical catchment of a given area, composed of a grid of cells. For each cell and at each time step, the model simulates (1) the production and the radioactive decay of ^{10}Be cosmogenic nuclides at the surface, (2) the removal of material by background erosion and (3) the removal of material by landslide processes. Background erosion corresponds to diffusive-like erosion processes, which are considered steady and spatially uniform at the catchment scale, in opposition to stochastic and discrete landslide processes.

First, model initialisation brings the landscape to a CRN erosional equilibrium. Equation (1) sets an initial CRN concentration, i.e. N_0 , to each cell of the landscape, resulting from the accumulation of ^{10}Be atoms at the surface for an arbitrary long period, i.e. $t = 5{,}000{,}000\ yr$, and an arbitrary erosion rate, i.e. $E_b = 0.05\ cm\ yr^{-1}$, ignoring inheritance (Lal, 1991):

$$N_0 = \frac{P}{\lambda + \frac{E_b}{z^*}}\left(1 - e^{-\left(\lambda + \frac{E_b}{z^*}\right)\cdot t}\right) \quad (1)$$

where P is the CRN surface production rate (at $g^{-1}\ yr^{-1}$), λ is the ^{10}Be decay constant, i.e. $4.62\times10^{-7}\ yr^{-1}$, and $z^* = \Lambda/\rho$ for which Λ is the neutron attenuation length ($g\ cm^{-2}$) and ρ is the material density ($g\ cm^{-3}$). Then, the CRN surface concentration for each cell is updated at each time step, successively for production and radioactive decay, background erosion and possibly landslide erosion. Equation (2) updates the inherited concentration N_S^{t-1} from the previous time step for production and decay:

$$N_R = \left(N_S^{t-1} + P\cdot\delta t\right)e^{-\lambda\cdot\delta t} \quad (2)$$

where δt is the time step. Subsequently, a layer of material of thickness D, i.e. the background erosion rate E_b multiplied by the time step δt, is removed. Before updating the surface concentration of each cell, both the ^{10}Be concentration and amount of atoms contained within the entire depth of erosion, i.e. respectively $N_{Surface}^{Depth}$ and $atoms_{Surface}^{Depth}$, are computed and stored for further analyses. The CRN concentration is therefore integrated at each depth x from the surface ($z = 0$) to the depth of erosion D using equation (3):

$$N_{Surface}^{Depth} = \int_0^D N_R \cdot e^{\frac{-x}{z^*}} dx = N_R \cdot z^* \cdot \left(1 - e^{\frac{-D}{z^*}}\right) \qquad (3)$$

The amount of atoms within the eroded layer is obtained by multiplying the concentration by the volume of the removed material given by equation (4):

$$atoms_{Surface}^{Depth} = N_{Surface}^{Depth} \cdot \rho \cdot A_{cell} \cdot D_{step} \qquad (4)$$

where A_{cell} is the area of the cell (cm²) and D_{step} is the depth increment related to the integral unit, i.e. 1 cm. Then, the CRN surface concentration of each cell of the landscape is updated according to background erosion rate E_b using equation (5):

$$N_S = N_R \cdot e^{-\left(\frac{E_b}{z^*}\right) \cdot \delta t} \qquad (5)$$

At each time step, according to a spatial Poisson process, the occurrence of landslides over the entire area is modelled using the landslide frequency derived from the return period (yr). If one or more landslides occur, the area A_{LS} of each event is defined based on the power law magnitude-frequency distribution function (Guzzetti et al., 2002; Hovius et al., 1997), scaled for minimum and maximum landslide areas, i.e. respectively $A_{\min}$ and $A_{\max}$, using equation (6):

$$p(A_{LS}) = \left[\frac{1-\alpha}{A_{\max}^{1-\alpha} - A_{\min}^{1-\alpha}} \right] \cdot A_{LS}^{-\alpha} \quad (6)$$

For each occurrence, the ^{10}Be concentration and amount of atoms removed by landslide erosion need to be computed, similarly to background erosion, using equations (3) and (4), where D_{LS} is the actual depth of the landslide, and computed using a simple geometric scaling (Hovius et al., 1997):

$$D_{LS} = \varepsilon \cdot \sqrt{A_{LS}} \quad (7)$$

where ε is an empirical scaling factor. Finally, the CRN concentration of the landslide-affected cells is updated using equation (8), according to the landslide depth:

$$N_S = N_S \cdot e^{-\frac{D_{LS}}{z^*}} \quad (8)$$

During the temporal evolution of the CRN surface concentration, several values are stored for further analyses: the total number of atoms and the volume of material removed from the catchment by background erosion and by landslides, the landslide characteristics (area, depth, spatial extent, and time of occurrence). Based on the eroded atoms and volumes, the sediment mixing module is applied, in order to take the buffering capacity of the catchment into account. As this algorithm was not modified within the model, we refer to *section 3.2* of Yanites et al. (2009).

At the end of the entire model process, volumetrically- and cosmogenically-derived erosion rates are computed to assess both the time-integrated erosion rates spanning the overall simulation time, i.e. *total* erosion rates, and the final state of the system, at the end of the model simulation, i.e. *final* values. Volumetrically-derived erosion rates, i.e. $E_{VOL-TOTAL}$ and $E_{VOL-FINAL}$, are respectively taking into account (1) the total volume of eroded sediments over the entire period and (2) the eroded volume during the last time step only. Mathematically, $E_{VOL-TOTAL}$ (Eq. (9)) is the total mass of sediments eroded by background erosion and by landslides over the entire time span of modelling, divided by the material density, i.e. ρ , the catchment area, i.e. $A_{catchment}$ and the time span, i.e. n.

$$E_{VOL-TOTAL} = \frac{\sum_{i=1}^{n} eroded\ mass_n}{\rho \cdot A_{catchment} \cdot n} \quad (9)$$

$E_{VOL-FINAL}$ (Eq. (10)) is the mass of eroded sediments during the last time step of modelling, divided by the material density and the catchment area.

$$E_{VOL-FINAL} = \frac{eroded\ mass_n}{\rho \cdot A_{catchment} \cdot n} \quad (10)$$

In the same way, *total* and *final* cosmogenically-derived erosion rates, i.e. $E_{CRN-TOTAL}$ and $E_{CRN-FINAL}$, are computed according to Lal et al. (1991), using the concentration of CRN atoms respectively within the total amount of eroded sediments (Eq. (11)) and within the amount of eroded sediment material during the last step of modelling (Eq. (12)).

$$E_{CRN-TOTAL} = z^* \cdot \left[\left(P \middle/ \frac{\sum_{i=1}^{n} atoms\ eroded_n}{\sum_{i=1}^{n} mass\ eroded_n} \right) - \lambda \right] \quad (11)$$

$$E_{CRN-FINAL} = z^* \cdot \left[\left(P \middle/ \frac{atoms\ eroded_n}{mass\ eroded_n} \right) - \lambda \right] \quad (12)$$

3.2. SCENARIOS

In total, 24 scenarios were defined to assess the influence of four different parameters on the CRN dynamics, i.e. the catchment area, the background erosion rate, the landslide return period and the landslide area distribution exponent (Table 5.1).

Table 5.1: Values of the parameters to implement the 24 scenarios of the CRN dynamics modelling. See Table 1 from Yanites et al. (2009) for parameters of the sediment mixing model.

Parameter	Symbol	Unit	Value(s)
Landslide return period	ls_{return}	yr	50 - 500 - 5000
Landslide area distribution exponent	α	1	2.1 – 2.7
Minimum landslide area	A_{min}	m²	100
Maximum landslide area	A_{max}	m²	1,000,000
Landslide depth scaling coefficient	ε	1	0.05
Background erosion rate	E_b	mm yr^{-1}	0.1 - 0.001
Catchment area	$A_{catchment}$	km²	1 - 10
CRN surface production rate	P	at g^{-1} yr^{-1}	6
Attenuation length	Λ	g cm^{-2}	160
Material density	ρ	g cm^{-3}	2

Due to very long computational time, scenarios with catchment areas larger than 10 km² were not implemented in the current study. Each scenario was iterated 100 times to explore the variability caused by the stochastic character of landslides. The time span for each simulation is 200,000 years, and the time increment is one year. The grid cell size is 10 m², and is independent of the catchment area.

The influence of landscape/landslide configurations on simulated erosion rates was assessed using two metrics: (1) the basic summary statistics, i.e. mean, standard deviation and range, and (2) the coefficient of variation, which is defined as the ratio between standard deviation and mean. As a relative metric, the latter allows comparing the variability of scenarios between each other, and is therefore more robust than the range of the distribution. Furthermore, we compared the CRN-derived erosion rates with volumetrically-derived erosion rates that includes physical transport of soil particles and sediment by geomorphic processes. The latter do not include chemical weathering, which is typically below 10% of the total mass losses in landslide-affected terrain (Tenorio et al., 2018).

4. RESULTS

The erosion rate distribution of the 100 simulations were computed for each scenario (Figure 5.1). Cosmogenically-derived erosion rates systematically overestimate volumetrically-derived values, due to landslide occurrence which dilutes ^{10}Be concentrations in river sediments. The simulated differences between erosion rates can be up to one-order of magnitude for scenarios with a landslide return period of 50 yr. In addition, *total* erosion rates, i.e. erosion cumulated over the entire simulation period, are systematically higher than *final* erosion rates, i.e. erosion computed for the last time step only. *Total* erosion rates were computed over the entire simulation time span and therefore encapsulate the entire sediment dynamics history. They are less sensible to single landslide processes occurring (or not) at the end of the modelling period. Consequently, further analyses are done on cosmogenically- and volumetrically-derived *total* erosion rates.

Overall, the background erosion rate, which represents diffusive-like erosion process rates occurring over the entire catchment area, drives the baseline of simulated erosion rates. Mean total erosion rates diverge from background erosion, i.e. from 0.001 and 0.1 mm yr^{-1}, when the landslide return period decreases, i.e. landslide frequency increases. All other parameters being equal, the mismatch is greater for a smaller landslide area distribution exponent, i.e. α, because larger landslides are more likely to occur (Figure 5.2), and landslide erosion is consequently higher. This result holds for both volumetrically- and cosmogenically-derived erosion rates. Catchment area has however a low influence in mean erosion rates, and this is the case for all parameters combinations. While landslide/landscape parameters logically influence the absolute values of simulated erosion rates, the latter are also characterised by range and variability, i.e. the coefficient of variation, when performing 100 iterations of the model using the same set of parameters.

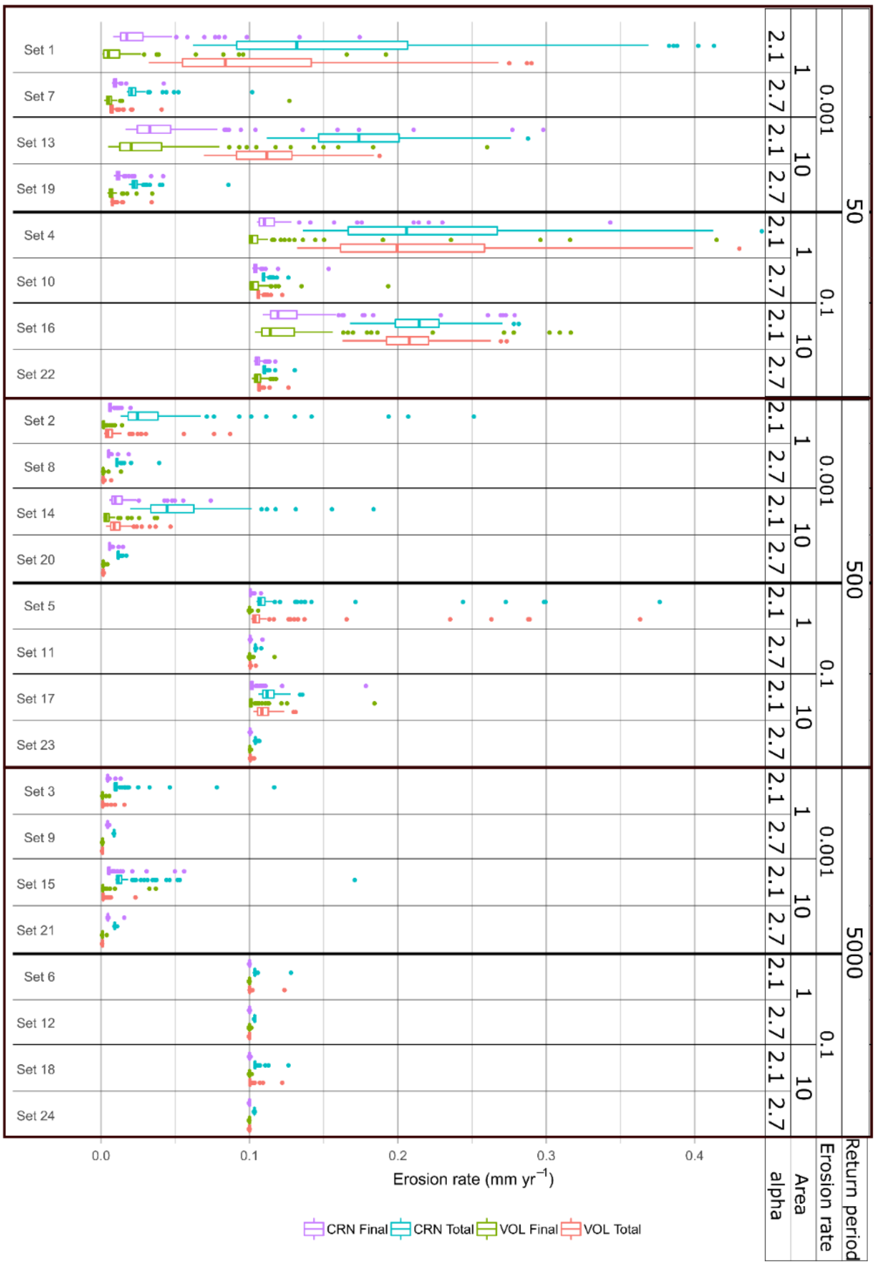

Figure 5.1: Distributions of volumetrically- and cosmogenically-derived erosion rates for the 100 simulations of each set of parameters (note that the y-axis has been slightly truncated because of large outlier simulations, which generate erosion rates up to ca. 5 mm yr^{-1}).

Interestingly, the range of simulated erosion rates is highly variable between scenarios. However, notwithstanding the stochastic effect of landslides on CRN dynamics, our results show that the behaviour of this metric is clearly predictable (Figure 5.3).

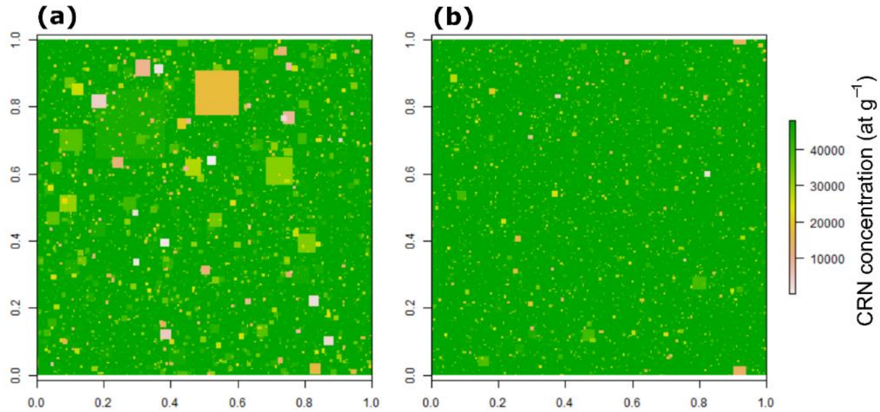

Figure 5.2: Spatialized CRN concentration (at g^{-1}) within a 10km² catchment after 200,000 years under a 0.1 mm yr^{-1} background erosion and landsliding with a return period of 50 years. The landslide area distribution coefficient is (a) 2.1 and (b) 2.7.

The range of simulated erosion rates is negatively correlated individually with the 4 varying parameters. This result also holds for the coefficient of variation (Figure 5.4), which is a relative metric. All other parameters being equal, the increase of one parameter will induce a decrease of the variability, i.e. the coefficient of variation, in erosion rates of about one-order of magnitude on average. Consequently, the variability of CRN-derived erosion rates is lower for large catchments, affected by few small landslides and intensive diffusion-like erosion processes. Moreover, an increase in landslide return period of one-order of magnitude typically leads to a one-order of magnitude decrease of the coefficient of variation. A smaller number of landslides will decrease the perturbation in CRN surface concentrations and subsequent dilution of CRN concentration in river sediments. However, this relation does not hold for scenarios characterised by low background erosion rates, i.e. 0.001 mm yr^{-1}, and small landslide area distribution coefficient, i.e. 2.1.

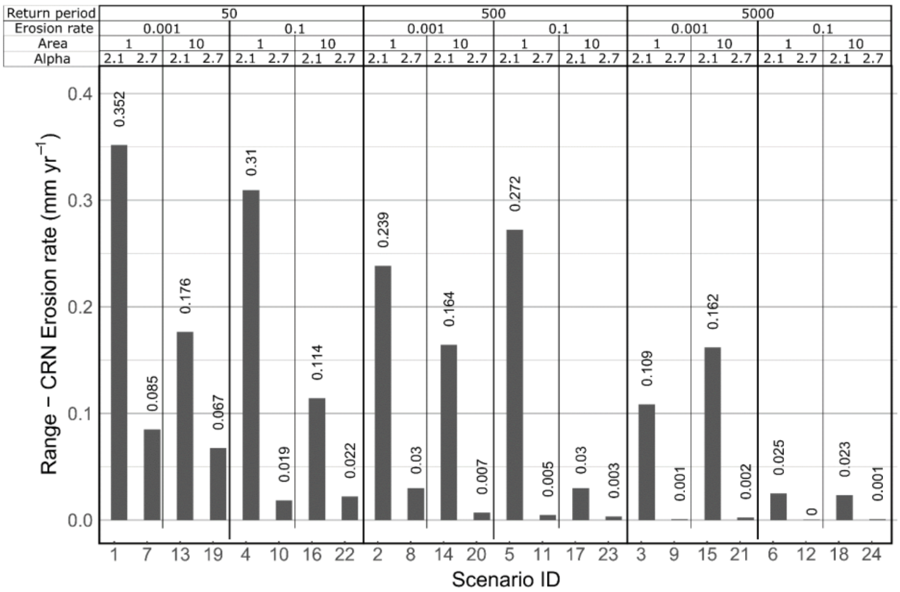

Figure 5.3: Range (mm yr^{-1}) of cosmogenically-derived *total* erosion rate values of 100 simulations for each scenario.

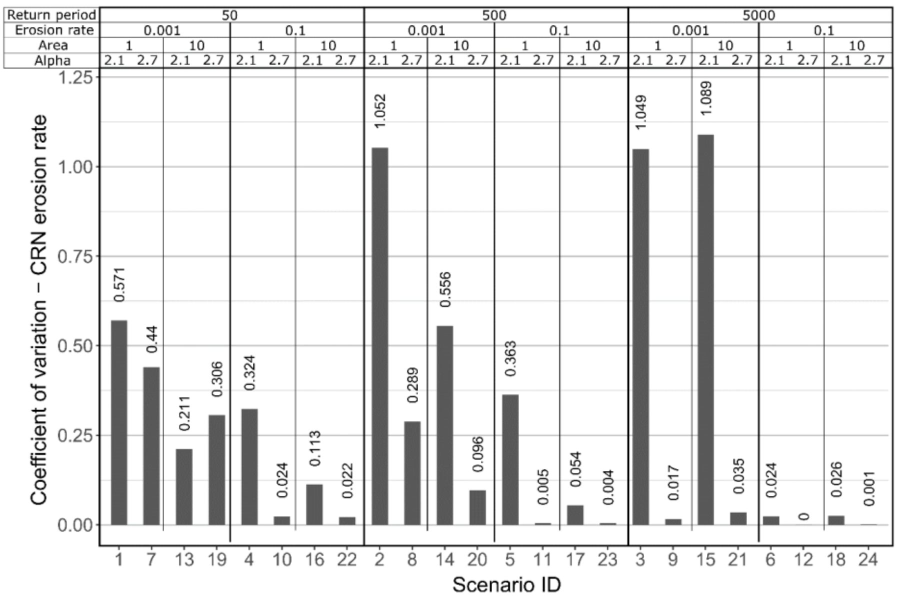

Figure 5.4: Coefficient of variation of cosmogenically-derived *total* erosion rate values of 100 simulations for each scenario.

For these configurations (i.e. scenario ID 1, 2, 3, 13, 14, 15), the variability increases along with landslide return period. This parameter combination is particularly sensitive to outliers because it may generate relatively large landslides while the impact of these events on CRN concentrations is poorly reduced by the background erosion effect.

5. DISCUSSION

The main requirement for a proper use of catchment-averaged cosmogenically-derived denudation rates is that sediment material is supplied at a rate which is proportional to the actual erosion rate in the catchment, during the integration time of cosmogenic nuclides. The occurrence of stochastic erosion processes, such as landslides, and fluvial sedimentation will therefore perturb the millennial scale dynamics of cosmogenic nuclide concentrations in sediment material at Earth surface and in eroded sediments transported in the fluvial system. Consequently, two catchments sharing the exact same characteristics may have a different landslide history on the long term, only due to the stochastic character of this process. It is possible that a succession of larger-than-average landslides occurs over the integration time of cosmogenic radionuclides. These occurrences will strongly dilute the ^{10}Be concentrations in river sediments. Additionally, it will also decrease ^{10}Be surface concentration at the landslide location and affect the subsequent CRN dynamics. Conversely, it is also possible that a succession of smaller-than-average landslides occurs during the last millennia and this will result in the inverse effect on CRN dynamics and ^{10}Be concentrations. These disturbances may therefore result respectively into an over- or underestimation of long-term denudation rates and may lead to biased landscape evolution assessments.

The effect of sediment mixing and landslides on ^{10}Be concentrations has been assessed both empirically (Savi et al., 2014; West et al., 2014) and numerically (Dingle et al., 2018; Niemi et al., 2005; Yanites et al., 2009). Both numerical attempts achieved a 2D model representing the landscape CRN dynamics over time. They mainly focussed on the parameters, which drive cosmogenically-derived erosion rates. Very recently, Dingle et al. (2018) assessed ^{10}Be concentration sensitivity to different parameters: background erosion, buffering capacity of the landscape and landslide depth. However, their numerical analysis is limited to the impact of a single landslide event without stochastic behaviour. Their main finding is that ^{10}Be concentrations are sensible to background and landslide erosion, but also that a variety of erosion scenarios can lead to similar ^{10}Be concentrations in river sediments. Nonetheless, these insights do not consider the stochastic effect of landslides on the CRN dynamics. Based on our simulation results, we argue that modelling the CRN dynamics including the stochastic process of landslides may in fact lead to an important variability in ^{10}Be concentrations and hence in cosmogenically-derived erosion rates. In this study, we further developed the 2D landscape model of Yanites et al. (2009) and iterated it 100 times for 24 exploratory scenarios depicting diverse but arbitrary landslide and landscape configurations. Even though these scenarios do not cover the wide range of landscape configurations which can be found in the nature, performing 100 iterations of these 24 simple scenarios already provided some important insights. Our data show that CRN-derived erosion rates are particularly sensitive to the stochastic effect of landslides in specific landslide/landscape configurations: small catchments affected by deep-seated landslides and low rates of background erosion. In addition to the landslide return period, the landslide area distribution coefficient strongly drives the variability in simulated cosmogenically-derived erosion rates. Because the α coefficient represents the slope of the inverse gamma magnitude frequency distribution of landslides, a small value increases the probability of large landslides. As the depth of landslides is proportional to the area, large occurrences of landslides will bring fresh sediment material to the surface and therefore dilute even more the ^{10}Be concentration of river sediments.

Beside the variability in simulated cosmogenically-derived erosion rates, landslide occurrence is also responsible for the overestimation of cosmogenically-derived erosion rates in comparison with volumetrically-derived erosion rates. Over long time periods, i.e. 10^2-10^6 years, the latter are only inferred using geochronological methods, e.g. cosmogenic nuclides or thermochronology. The bias is assessed by calculating the difference between *total* cosmogenically- and volumetrically-derived erosion rates. Even though *total* and *final* erosion rates show similar trends in our results, the *total* erosion rate metric integrates the CRN dynamics over the entire time span of modelling. Therefore, individual landslide occurrences do not influence *total* erosion rates as is the case for *final* values. Globally, all other parameters being equal, the overestimation of cosmogenically-derived erosion rates is negatively correlated to the landslide return period (Figure 5.5). Consequently, the accuracy of CRN-derived erosion rates increases for landscapes where landslides are not a dominant erosion process. In addition, overestimation is larger when background erosion is low because it poorly reduces the landslide effect on the ^{10}Be surface concentrations. Besides, the variability of the overestimation is logically and negatively correlated with the variability of cosmogenically-derived erosion rates.

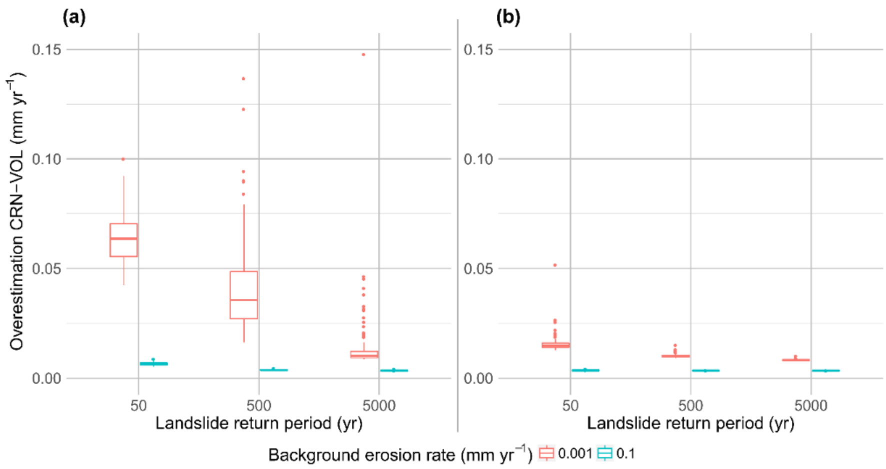

Figure 5.5: Overestimation of cosmogenically-derived erosion rates compared to volumetrically-derived erosion rates. Drainage area is 10 km². The landslide area distribution coefficient is (a) 2.1 and (b) 2.7.

To disentangle the stochastic impact of landslide occurrence on CRN dynamics and the subsequent variability in simulated erosion rates, numerical models are particularly valuable because they allow exploring a wide range of landscape/landslide scenarios. In this study, by modelling the CRN dynamics for a range of 24 scenarios depicting various landscape and landslide configurations, we opened perspectives for further research on the topic. It will require a proper implementation of scenarios, which may better represent real conditions in order to link empirical field data with numerical modelling results. However, our results provide a first quantitative insight on landscape characteristics which could lead to a bias in CRN-derived erosion estimates and therefore lead to misinterpretation of landscape development. Even though it is out of the scope of the current research, it is worth mentioning that current numerical implementations of CRN modelling (this chapter; Niemi et al., 2005; Yanites et al., 2009) leave perspectives for further improvements to overcome current limitations. (1) The landscape topography does not actually evolve through time due to erosion processes. (2) Landslides are randomly distributed, ignoring controlling factors, e.g. lithology or slope. (3) Sediment routing from Yanites et al. (2009) is catchment-averaged and does not account for the topography. Taking into account sediment transport by including a river network in the model would be the first improvement because CRN dilution by landslides is highly sensitive to the rate of landslide surface displacements and to the degree of connectivity between the landslide and river network. In addition to methodological considerations, future research is needed to thoroughly assess the variability of simulated CRN-derived denudation rates, explore the equifinality problem along with the effect of initial surface conditions (Dingle et al., 2018; Hancock et al., 2016), and compare modelling results with field data.

In addition, the scenarios need to represent realistic erosion rates and patterns, derived from field data that are readily and comprehensively available in published literature. Importantly, the theoretical results need to be compared with field data from various landscape and landslide settings (e.g. Codilean et al., 2018). Moreover, based on a selection of the most plausible erosion scenarios, a sensitivity analyses needs to be performed to identify the model parameters that have the largest impact on the CRN variability.

6. CONCLUSION

Building on the work of Niemi et al. (2005) and Yanites et al. (2009), our study explored the stochastic effect of landslides on cosmogenically-derived erosion rates using a numerical model of CRN dynamics. By performing 100 iterations of 24 different scenarios, we assessed the variability in CRN-derived erosion rates and the mismatch between the latter and volumetrically-derived erosion rates. Scenarios here represent a range of landscape/landslide configurations characterised by the following parameters: the catchment area, the background erosion rate, the landslide return period and the landslide area distribution exponent

Our simulations highlight two main conclusions: (1) the stochastic character of landslides induces large variability in cosmogenically-derived erosion rates and (2) cosmogenically-derived erosion rates may largely overestimate actual erosion in landslide-prone landscapes. First, we show that the variability in cosmogenically-derived denudation rates can be high according to landscape configurations. This variability is mainly driven by landslide return period and landslide area distribution coefficient. As a stochastic process, landslides may thus result in higher-than-average erosion estimates because of the occurrence of some large landslides bringing deeply shielded sediment material to the surface. This will dilute ^{10}Be concentrations in river sediments and increase cosmogenically-derived erosion rates. Conversely, the opposite stochastic behaviour will lead to a decrease in erosion rates. In both cases, it will affect surface concentrations for subsequent landscape evolution. Moreover, the overestimation of cosmogenically-derived erosion rates compared to actual erosion, i.e. volumetrically-derived erosion rates, decreases when landslide return period and background erosion increase. Consequently, when landslides act as a dominant sediment source in the landscape, conclusions drawn from cosmogenic radionuclide erosion rates should be considered with caution.

CHAPTER 6

CONCLUSIONS

The movement of sediment from mountainous uplands to continental margins modifies the terrestrial surface and drives the rate of topographic evolution. The pathways of sediment transport from their sources to sinks are nowadays known under the term of *sediment cascade*. Quantifying the patterns and rates of individual processes within the sediment cascade is challenging because geomorphic processes are unsteady across time and space. This behaviour is caused by the inherent stochastic nature of the geomorphic processes involved: sediment production on hillslopes, sediment supply to rivers, transport to and evacuation by the fluvial network, intermediate storage on hillslopes and in channels, and eventually deposition in lower reaches. While the scientific community acknowledges the importance of the sediment cascade to constrain long-term topographic evolution and biogeochemical cycles, the geomorphic response to sediment production and supply forcing is commonly assessed over one given time scale. Only few studies attempted to integrate different spatial and temporal scales to better constrain the timing of the sediment cascade.

In an effort to improve our quantitative understanding of the sediment cascade in landslide-prone mountainous environments, this doctoral dissertation aimed at providing a new insight on the spatio-temporal dynamics of sediment transfer rates between hillslopes and channels over 10^0-10^3 years. We first assessed, in *Chapter II*, the precision of three-dimensional (3D) topographic reconstructions derived using the computer vision structure-from-motion (SfM) algorithm based on aerial photographs acquired with an unmanned aerial vehicle (UAV). This step is mandatory to set the limit of detection of the UAV-SfM methodology for temporal monitoring of geomorphic processes. In *Chapter III*, we used the UAV-SfM framework from *Chapter II* to quantify the annual sediment dynamics of a landslide-affected catchment located in the foothills of the Central Swiss Alps. These data on annual sediment fluxes were used as an input for *Chapter IV*, which constitutes the central piece of this thesis. In this chapter, we characterised the processes controlling hillslope-channel coupling based on a spatial database of sediment fluxes at annual, decadal and millennial time scales. As erosion processes in mountainous terrain are subject to episodic, but large landslides, we explored, in *Chapter V*, the variability of cosmogenic radionuclides (CRN) based denudation rates in landslide-prone landscapes for various erosion scenarios using numerical modelling.

1. MAIN FINDINGS AND CONTRIBUTIONS

The first milestone was to achieve landslide monitoring in mountainous environments using a low-cost and lightweight platform: the unmanned aerial vehicle or drone. At the time of the beginning of this PhD project, the use of the UAV-SfM framework to reconstruct 3D topographic surfaces was still in its early stages. Studies that were published by 2015 used this methodology to acquire topographic data of natural environments. They often assessed the accuracy of their measurements by comparison with independent topographic datasets, such as aerial or terrestrial laser scanning, but never quantified the precision. However, the asset of the UAV-SfM framework is its portability to be deployed on demand and used repeatedly over poorly accessible dynamic environments. As part of temporal analysis of earth surface changes, it is mandatory to account for errors that are inherent to the UAV-SfM framework by assessing its precision or reproducibility. Importantly, this precision sets the limit of detection for topographic changes when monitoring dynamic environments. To fill this gap in the literature, we repeatedly surveyed a study site, which has not experienced topographic changes and compared topographic reconstructions by computing the digital elevation models (DEM) of the differences (DoD). The main finding of *Chapter II* is that the SfM algorithm provides highly reproducible topographic data with high-quality wide-angle camera lenses. The mean absolute differences between identical replications, i.e. the internal precision, is only 0.06 m using a 28 mm lens. The external precision, i.e. the error associated to the location of the ground control points (GCP), is 0.24 m with a low dispersion of values. Importantly, the quality of the global positioning system (GPS) receiver used to perform GCP georeferencing drives the external accuracy. Besides, both the amount and the pattern of GCP regulate the reproducibility of the SfM reconstructions. Based on these results, our recommendation is to scatter GCPs as regularly as possible, even in the case of a limited number of control points.

Building on our experience from *Chapter II*, we were confident about the expected precision of our new low-cost and lightweight topographic tool, i.e. the UAV-SfM framework. Therefore, the aim of *Chapter III* was to perform a proper monitoring of a dynamic, landslide-affected environment in order to assess its sediment dynamics at very-high spatial and temporal resolution. We surveyed the Schimbrig earthflow, located in the Entle River catchment in the foothills of the Central Swiss Alps, in October 2013, June 2014 and October 2015. Based on a temporal database of 3D topographic point clouds, we quantified (1) the volumetric sediment budget by DEM of differences, (2) the horizontal surface displacements using the COSI-Corr image correlation algorithm, and (3) the 3D changes using the multiscale model to model cloud comparison algorithm. The main findings of *Chapter III* are twofold. First, in terms of sediment dynamics, we highlight an intense sediment redistribution within the earthflow, with a mean annual horizontal displacement of ca. 6 m between 2014 and 2015, and a frontal lobe advance of ca. 55 m. However, the mass balance of the earthflow is in equilibrium, meaning that the evacuated sediment is not significant and within error limits. In fact, the earthflow is only readjusting its shape to a new state of equilibrium after a major slope failure, which occurred in 1994. Second, by combining the volumetric sediment budget, the horizontal surface displacements and the 3D changes, we were able to capture the internal mechanisms of the earthflow based on high-resolution aerial imagery. Interestingly, the earthflow structure evolves at the annual scale, from a succession of three to two rotational units, with the entire mass of material slowly moving downslope.

The central piece of the thesis is the *Chapter IV* that aimed to assess the spatio-temporal dynamics of the processes controlling hillslope-channel coupling over 10^0-10^3 years, based on a database of sediment fluxes for the Entle River catchment. At the annual scale, we computed sediment fluxes based on the very high-resolution monitoring of the Schimbrig earthflow. At the decadal scale, we used photogrammetrically-derived sediment fluxes from Schwab et al. (2008) over the entire Schimbrig catchment. At the millennial scale, we quantified cosmogenic nuclide-derived catchment averaged denudation rates in the rivers draining the Schimbrig earthflow and used measurements in the entire Entle River catchment from Van den Berg et al. (2010). Our results show that the decadal sediment flux is at least two orders of magnitude higher than the annual and long-term sediment fluxes. These observations point to the stochasticity of sediment production and geomorphic coupling between hillslopes and channels. While the earthflow can be highly dynamic at annual or decadal time scale, a large portion of the landslide-derived material is stored on the hillslopes. Only during occasional events when hillslopes and river channels are fully coupled, the landslide-derived debris is evacuated by superimposed debris flows to the river network. Unlike the hillslopes that are highly dynamic at annual and decadal time scale, the river channels respond to stochastic sediment supply over longer time periods, i.e. thousands of years. Consequently, the spatio-temporal pattern of the sediment cascade is not so much driven by individual landslide events captured at annual or decadal time scale, but rather by the magnitude and frequency of geomorphic coupling between hillslopes and channel in mountainous catchments.

Denudation rates at millennial time scale are increasingly derived from cosmogenic nuclide concentrations in river sediments. Consequently, *Chapter V* explored the potential variability of millennial denudation rates caused by the stochasticity of landslide events. To this end, we modified the numerical CRN landscape model of Yanites et al. (2009) to properly generate landslide events as a Poisson process. We also enhanced the computation time of simulations, and adapted it to a free and open-source software environment, i.e. R. The main contribution of *Chapter V* is the introduction of stochasticity in the model simulations, as landscape/landslide scenarios were iterated 100 times to assess variability in the cosmogenically- and volumetrically-derived erosion rates. Our results show that the variability in cosmogenically-derived erosion rates is inversely proportional to the landslide return period and landslide area distribution coefficient. Second, potential overestimation of cosmogenically-derived erosion rates compared to volumetric erosion rates is high for shorter return periods and lower landslide area distribution coefficients. The model simulations allow assessing the expected variability and bias in cosmogenically-derived erosion rates in landslide-affected environments.

2. PERSPECTIVES

Constraining the timing of the sediment cascade in mountainous environments is a difficult task because of the stochastic nature of the geomorphic processes involved. As mentioned in *Chapter I*, integrating patterns and rates of individual processes over different spatial and temporal scales could help to unravel the geomorphic response of the landscape to sediment production and supply forcing (Burt and Allison, 2010; Fryirs, 2013; Korup et al., 2010). The multiscale approach used in this thesis shows the benefit of analysing sediment fluxes at various spatio-temporal scales. Our results from *Chapter IV* suggest that annual and/or decadal sediment fluxes are not necessarily reflecting the millennial sediment fluxes. Geomorphic processes such as landslides have an inherent periodicity that depends on the geomorphic system. This episodicity in sediment supply, transfer and export to the river network will control the erosion rate at the catchment scale. Considering that our multi-temporal approach provides results on the stochasticity of the geomorphic processes, and the coupling between hillslopes and river channels, this PhD research opens new perspectives regarding sediment connectivity and geomorphic response to stochastic geomorphic forcing.

We join the conclusion of Bracken et al. (2015) who state that expanding field-based data over a range of processes, environmental conditions and time scales allows to better constrain erosion rates and our understanding of how sediment connectivity plays a role on landscape evolution. Field-based studies are required to validate the results of model-based studies on sediment connectivity and dynamics (Gran and Czuba, 2017; Heckmann and Schwanghart, 2013; Sklar et al., 2017), and to confront results from both approaches.

To join this effort, the construction of spatio-temporal databases of sediment fluxes for other or larger landslide-prone areas would allow widening of our knowledge on the variety of sediment connectivity patterns and rates. The applicability of our conceptual framework presented in *Chapter IV* (Figure 4.1) can be verified and applied in a range of landscape configurations. Whereas the Entle river catchment is a supply-limited system, i.e. sediment are efficiently transported downstream, exploring the propagation of sediment pulses in transport-limited channel systems would enable to enlarge the knowledge about sediment connectivity. The latter are typical for co-seismic landslide-affected regions where earthquakes trigger widespread and simultaneous sediment pulses. Whereas multiple studies assessed the geomorphic recovery from seismic events over a single time scale, a spatially-consistent integration of landslide displacement rates from remote sensing (e.g. Parker et al., 2011), sediment loads (e.g. Dadson et al., 2004; Wang et al., 2015), and long-term sediment dynamics derived from cosmogenic radionuclides (e.g. Wang et al., 2017) would, for instance, be insightful.

A second perspective regarding sediment cascade assessments is the need to enlarge the spatial extent of short-term analyses of sediment dynamics. In this thesis, the assessment of annual sediment fluxes is achieved at very high spatial and temporal resolution, exploiting the low-cost and flexible character of UAVs. However, this methodology is limited in spatial extent to a few km^2. Even though the flight autonomy of UAV platforms never ceases to increase, i.e. up to 45 min as of 2018, it would be difficult to apply this very high-resolution method at the regional scale, e.g. over several hundreds of km^2. A worthwhile trade-off between resolution and spatial extent could be done by exploiting national aerial laser scanning surveys, which are increasingly available in the recent years. For instance, Switzerland updates its 0.50 m resolution digital terrain model every 6 years. This time series of topographic representations could be used to explore earth surface changes at high-resolution for the most active areas of the Swiss Alps. Data processing could be done using one or a combination of methodologies from *Chapter III*, i.e. DEM of differences, image correlation or point cloud comparison. Using this type of data, surface changes smaller than ca. 0.70 m would probably be below the limit of detection inherent to large-scale LiDAR digital terrain models. However, the short-term assessment would be possible over large spatial scale to include all current landslides and associated sediment pulses. Moreover, digital terrain models derived from LiDAR topographic data do not capture vegetation and other man-made features. For further landslide monitoring, it will be mandatory to evaluate regolith bulk density and consider it when computing sediment budget in order to provide final values properly comparable with published literature. In this thesis and especially in *Chapter III*, we assumed that bulk density was constant throughout the earthflow based on visual surface assessment. However, we acknowledge this bias needs to be addressed in future research.

From a methodological point of view, the PhD thesis provides results on (1) the reproducibility of UAV-SfM-based topographic reconstructions and (2) on the influence of the stochastic character of landslides on the variability of CRN-derived denudation rates. First, new technological advances in topography acquisition platforms are allowing us to monitor geomorphic processes at spatial resolutions that were previously impossible to obtain for large areas. Among other solutions, the UAV-SfM framework has high potential for 4D monitoring of the terrestrial environments in settings that are difficult to access. Our results from *Chapter II* show that this method provides centimetric accuracy and precision using GCP georeferencing. In the context of post-catastrophic natural events, such as earthquakes, volcanic eruptions, landslides, floods or inundations, the location of GCPs might be difficult due to accessibility of the terrain. However, we showed that this parameter might affect precision of the 3D reconstructions and lower the signal-to-noise ratio to critical values. To overcome this limitation, the use of real time kinematics (RTK) GPS embedded directly on the UAV platform offers new perspectives, and can enhance the accuracy of point cloud reconstructions (Forlani et al., 2018; Stöcker et al., 2017a). As for GCP georeferencing some years ago, the development of this improved UAV-SfM framework is currently in its early stages. Consequently, both accuracy and precision of should be properly assessed to set the limit of detection of the acquisition method in various environments and topographic settings. The embedded RTK GPS is likely to provide centimetric accuracy, allowing to increase the precision of natural environment monitoring. The sediment budget assessment of the Schimbrig earthflow in *Chapter III* would eventually benefit from these technological advances in a near future.

Second, we explored the potential variability of millennial denudation rates derived from CRN in river sediments caused by the stochastic behaviour of landslide processes using a numerical model. While Niemi et al. (2005) and Yanites et al. (2009) modelled one single iteration of CRN temporal dynamics for many landscape/landslide configurations, Dingle et al. (2018) showed the equifinality of CRN-derived denudation rates from different erosion scenarios. In *Chapter V*, we introduced the stochasticity of geomorphic processes in a CRN model, and iterated 100 times a modified version of the Yanites et al. (2009) model. This allowed us to quantify the variability of CRN concentrations according to various erosion scenarios. The preliminary results of this chapter show the relevance of CRN modelling for erosion studies, and open multiple perspectives for future research: (1) to thoroughly assess the variability of simulated CRN-derived denudation rates, (2) to explore the equifinality problem along with the effect of initial surface conditions (Dingle et al., 2018; Hancock et al., 2016), (3) to compare modelling results with field data, and (4) to tune the model parameters to better match geomorphic process rates in mountainous terrain. To achieve these goals, a more comprehensive range of erosion scenarios should be modelled. An attention must be drawn to define erosion scenarios that depict realistic geomorphic settings, for which field data are readily and comprehensively available in published literature. Importantly, these theoretical results need to be compared with a compilation of field data from various landscape/landslide settings (e.g. Codilean et al., 2018). Moreover, based on a selection of plausible erosion scenarios, the parameters that are most influential on the

CRN variability need to be highlighted by performing a sensitivity analysis. Eventually, the outcome of this research can guide sediment sampling for ^{10}Be quantification in environments characterised by a complex landslide history. Finally, the model can be refined to depict more properly the sediment dynamics and routing on hillslopes and in the fluvial network. This could be done by improving the existing model or including the CRN dynamics component in an existing landscape evolution model (e.g. Barnhart et al., 2018; Tucker and Hancock, 2010).

REFERENCES

Aalto, R., Dunne, T. and Guyot, J. L.: Geomorphic controls on Andean denudation rates, J. Geol., 114(1), 85–99, doi:10.1086/498101, 2006.

Allen, P. A.: Earth surface processes, Wiley., 2009.

Auer, M.: Regionalisierung von Schneeparametern—Eine Methode zur Darstellung von Schneeparametern imRelief., University of Berne., 2003.

Aufdenkampe, A. K., Mayorga, E., Raymond, P. A., Melack, J. M., Doney, S. C., Alin, S. R., Aalto, R. E. and Yoo, K.: Riverine coupling of biogeochemical cycles between land, oceans, and atmosphere, Front. Ecol. Environ., 9(1), 53–60, doi:10.1890/100014, 2011.

Ayoub, F., Leprince, S. and Avouac, J.-P.: Co-registration and correlation of aerial photographs for ground deformation measurements, ISPRS J. Photogramm. Remote Sens., 64(6), 551–560, doi:10.1016/j.isprsjprs.2009.03.005, 2009.

Barnhart, K. R., Glade, R. C., Shobe, C. M. and Tucker, E.: terrainbento 1.0: a Python package for multi-model analysis in long-term drainage basin evolution, Geosci. Model Dev. Discuss., (October), 1–57, doi:10.5194/gmd-2018-204, 2018.

Bellin, N., Vanacker, V., van Wesemael, B., Solé-Benet, A. and Bakker, M. M.: Natural and anthropogenic controls on soil erosion in the internal betic Cordillera (southeast Spain), Catena, 87(2), 190–200, doi:10.1016/j.catena.2011.05.022, 2011.

Benda, L. and Dunne, T.: Stochastic forcing of sediment routing and storage in channel networks, Water Resour. Res., 33(12), 2865–2880, doi:10.1029/97WR02387, 1997a.

Benda, L. and Dunne, T.: Stochastic forcing of sediment supply to channel networks from landsliding and debris flow, Water Resour. Res., 33(12), 2849–2863, doi:10.1029/97WR02388, 1997b.

Bendig, J., Willkomm, M., Tilly, N., Gnyp, M. L., Bennertz, S., Qiang, C., Miao, Y. and Bareth, G.: Very high resolution crop surface models (CSMs) from UAV-based stereo images for rice growth monitoring In Northeast China, Int. Arch. Photogramm. Remote Sens. Spat. Inf. Sci., 40–1/W2(September), 45–50, 2013.

Bennett, G. L., Molnar, P., McArdell, B. W., Schlunegger, F. and Burlando, P.: Patterns and controls of sediment production, transfer and yield in the Illgraben, Geomorphology, 188, 68–82, doi:10.1016/j.geomorph.2012.11.029, 2013.

Bennett, G. L., Molnar, P., McArdell, B. W. and Burlando, P.: A probabilistic sediment cascade model of sediment transfer in the Illgraben, Water Resour. Res., 50, 1225–1244, doi:doi:10.1002/2013WR013806, 2014.

Berger, C., McArdell, B. W. and Schlunegger, F.: Sediment transfer patterns at the Illgraben catchment, Switzerland: Implications for the time scales of debris flow activities, Geomorphology, 125(3), 421–432, doi:10.1016/j.geomorph.2010.10.019, 2011.

Bernet, M., Zattin, M., Garver, J. I., Brandon, M. T. and Vance, J. A.: Steady-state exhumation of the European Alps, Geology, 29(1), 35–38, doi:10.1130/0091-7613(2001)029<0035:SSEOTE>2.0.CO;2, 2001.

Bierman, P. R. and Nichols, K. K.: Rock to sediment - Slope to sea with ^{10}Be - Rates of landscape change, Annu. Rev. Earth Planet. Sci., 32(1), 215–255, doi:10.1146/annurev.earth.32.101802.120539, 2004.

Binnie, S. A., Phillips, W. M., Summerfield, M. A. and Keith Fifield, L.: Sediment mixing and basin-wide cosmogenic nuclide analysis in rapidly eroding mountainous environments, Quat. Geochronol., 1(1), 4–14, doi:10.1016/j.quageo.2006.06.013, 2006.

Binnie, S. A., Phillips, W. M., Summerfield, M. A. and Fifield, L. K.: Tectonic uplift, threshold hillslopes, and denudation rates in a developing mountain range, Geology, 35(8), 743–746, doi:10.1130/G23641A.1, 2007.

Bishop, P.: Long-term landscape evolution: linking tectonics and surface processes, Earth Surf. Process. Landforms, 32, 329–365, doi:10.1002/esp.1493, 2007.

Blasone, G., Cavalli, M., Marchi, L. and Cazorzi, F.: Monitoring sediment source areas in a debris-flow catchment using terrestrial laser scanning, Catena, 123, 23–36, doi:10.1016/j.catena.2014.07.001, 2014.

Bracken, L. J., Turnbull, L., Wainwright, J. and Bogaart, P.: Sediment connectivity: A framework for understanding sediment transfer at multiple scales, Earth Surf. Process. Landforms, 40(2), 177–188, doi:10.1002/esp.3635, 2015.

Brasington, J., Rumsby, B. T. and McVey, R. A.: Monitoring and modelling morphological change in a braided gravel-bed river using high resolution GPS-based survey, Earth Surf. Process. Landforms, 25(9), 973–990, doi:10.1002/1096-9837(200008)25:9<973::AID-ESP111>3.0.CO;2-Y, 2000.

Brasington, J., Vericat, D. and Rychkov, I.: Modeling river bed morphology, roughness, and surface sedimentology using high resolution terrestrial laser scanning, Water Resour. Res., 48(11), doi:10.1029/2012WR012223, 2012.

Braucher, R., Merchel, S., Borgomano, J. and Bourlès, D. L.: Production of cosmogenic radionuclides at great depth: A multi element approach, Earth Planet. Sci. Lett., 309(1–2), 1–9, doi:10.1016/j.epsl.2011.06.036, 2011.

Bridge, J. and Demicco, R.: Earth Surface Processes, Landforms and Sediment Deposits, Cambridge University Press, Cambridge., 2008.

Brown, A. G., Carey, C., Erkens, G., Fuchs, M., Hoffmann, T., Macaire, J.-J., Moldenhauer, K.-M. and Walling, D. E.: From sedimentary records to sediment budgets: Multiple approaches to catchment sediment flux, Geomorphology, 108(1–2), 35–47, doi:10.1016/j.geomorph.2008.01.021, 2009.

Brown, E. T., Stallard, R. F., Larsen, M. C., Raisbeck, G. M. and Yiou, F.: Denudation rates determined from the accumulation of in situ-produced ^{10}Be in the Luquillo experimental forest, Puerto Rico, Earth Planet. Sci. Lett., 129(1–4), 193–202, doi:10.1016/0012-821X(94)00249-X, 1995.

Burt, T. P. and Allison, R. J., Eds.: Sediment Cascades: An integrated approach, John Wiley & Sons, Ltd, Chichester, UK., 2010.

Burtin, A., Hovius, N., McArdell, B. W., Turowski, J. M. and Vergne, J.: Seismic constraints on dynamic links between geomorphic processes and routing of sediment in a steep mountain catchment, Earth Surf. Dyn., 2(1), 21–33, doi:10.5194/esurf-2-21-2014, 2014.

Caduff, R., Schlunegger, F., Kos, A. and Wiesmann, A.: A review of terrestrial radar interferometry for measuring surface change in the geosciences, Earth Surf. Process. Landforms, 40(2), 208–228, doi:10.1002/esp.3656, 2015.

Carbonneau, P. E. and Dietrich, J. T.: Cost-effective non-metric photogrammetry from consumer-grade sUAS: implications for direct georeferencing of structure from motion photogrammetry, Earth Surf. Process. Landforms, 42(3), 473–486, doi:10.1002/esp.4012, 2017.

Casson, B., Delacourt, C., Baratoux, D. and Allemand, P.: Seventeen years of the “La Clapière” landslide evolution analysed from ortho-rectified aerial photographs, Eng. Geol., 68(1–2), 123–139, doi:10.1016/S0013-7952(02)00201-6, 2003.

Christl, M., Vockenhuber, C., Kubik, P. W., Wacker, L., Lachner, J., Alfimov, V. and Synal, H. A.: The ETH Zurich AMS facilities: Performance parameters and reference materials, Nucl. Instruments Methods Phys. Res. Sect. B Beam Interact. with Mater. Atoms, 294, 29–38, doi:10.1016/j.nimb.2012.03.004, 2013.

Codilean, A. T., Munack, H., Cohen, T. J., Saktura, W. M., Gray, A. and Mudd, S. M.: OCTOPUS: An Open Cosmogenic Isotope and Luminescence Database, Earth Syst. Sci. Data Discuss., (March), 1–23, doi:10.5194/essd-2018-32, 2018.

Corominas, J. and Moya, J.: A review of assessing landslide frequency for hazard zoning purposes, Eng. Geol., 102(3–4), 193–213, doi:10.1016/j.enggeo.2008.03.018, 2008.

Crozier, M. J.: Deciphering the effect of climate change on landslide activity: A review, Geomorphology, 124(3–4), 260–267, doi:10.1016/j.geomorph.2010.04.009, 2010.

Crozier, M. J. and Glade, T.: Frequency and magnitude of landsliding: fundamental research issues, Zeitschrift für Geomorphol. Suppl. Vol., 115, 141–155, doi:10.1127/zfgsuppl/115/1999/141, 1999.

CSDMS: Cosmoland repository, [online] Available from: https://github.com/csdms-contrib/cosmoland, 2011.

Cubasch, U., Wuebbles, D., Chen, D., Facchini, M. C., Frame, D., Mahowald, N. and Winther, J.-G.: Introduction in Climate Change 2013, Intergov. Panel Clim. Chang. 2013 Phys. Sci. Basis. Contrib. Work. Gr. I to Fifth Assess. Rep. Intergov. Panel Clim. Chang., 119–158, doi:10.1017/CBO9781107415324.007, 2013.

D'Oleire-Oltmanns, S., Marzolff, I., Peter, K. and Ries, J.: Unmanned Aerial Vehicle (UAV) for Monitoring Soil Erosion in Morocco, Remote Sens., 4(12), 3390–3416, doi:10.3390/rs4113390, 2012.

Dadson, S. J., Hovius, N., Chen, H., Dade, W. B., Lin, J. C., Hsu, M. L., Lin, C. W., Horng, M. J., Chen, T. C., Milliman, J. and Stark, C. P.: Earthquake-triggered increase in sediment delivery from an active mountain belt, Geology, 32(8), 733–736, doi:10.1130/G20639.1, 2004.

Dandois, J. P. and Ellis, E. C.: Remote Sensing of Vegetation Structure Using Computer Vision, Remote Sens., 2(4), 1157–1176, doi:10.3390/rs2041157, 2010.

Delacourt, C., Allemand, P., Casson, B. and Vadon, H.: Velocity field of the "La Clapière" landslide measured by the correlation of aerial and QuickBird satellite images, Geophys. Res. Lett., 31(15), 1–5, doi:10.1029/2004GL020193, 2004.

Delong, S. B., Prentice, C. S., Hilley, G. E. and Ebert, Y.: Multitemporal ALSM change detection, sediment delivery, and process mapping at an active earthflow, Earth Surf. Process. Landforms, 37(3), 262–272, doi:10.1002/esp.2234, 2012.

Dewitte, O., Jasselette, J.-C., Cornet, Y., Van Den Eeckhaut, M., Collignon, A., Poesen, J. and Demoulin, A.: Tracking landslide displacements by multi-temporal DTMs: A combined aerial stereophotogrammetric and LIDAR approach in western Belgium, Eng. Geol., 99(1–2), 11–22, doi:10.1016/j.enggeo.2008.02.006, 2008.

Dibiase, R. A., Heimsath, A. M. and Whipple, K. X.: Hillslope response to tectonic forcing in threshold landscapes, Earth Surf. Process. Landforms, 37(8), 855–865, doi:10.1002/esp.3205, 2012.

DiBiase, R. a., Whipple, K. X., Heimsath, A. M. and Ouimet, W. B.: Landscape form and millennial erosion rates in the San Gabriel Mountains, CA, Earth Planet. Sci. Lett., 289(1–2), 134–144, doi:10.1016/j.epsl.2009.10.036, 2010.

Dietrich, W. E. and Dunne, T.: Sediment budget for a small catchment in a mountainous terrain, Zeitschrift für Geomorphol. Suppl. Band, 29, 191–206, 1978.

Dingle, E. H., Sinclair, H. D., Attal, M., Rodés, Á. and Singh, V.: Temporal variability in detrital ^{10}Be concentrations in large Himalayan catchments, Earth Surf. Dyn. Discuss., 1–51, doi:10.5194/esurf-2017-73, 2018.

Dunai, T. J.: Cosmogenic nuclides: principles, concepts and applications in the earth surface sciences, Cambridge University Press, Cambridge., 2010.

Egholm, D. L., Knudsen, M. F. and Sandiford, M.: Lifespan of mountain ranges scaled by feedbacks between landsliding and erosion by rivers, Nature, 498(7455), 475–478, doi:10.1038/nature12218, 2013.

Eltner, A., Kaiser, A., Castillo, C., Rock, G., Neugirg, F. and Abellan, A.: Image-based surface reconstruction in geomorphometry – merits, limits and developments of a promising tool for geoscientists, Earth Surf. Dyn., 4, 359–389, doi:10.5194/esurf-4-359-2016, 2016.

Fernández, T., Pérez, J. L., Cardenal, J., Gómez, J. M., Colomo, C. and Delgado, J.: Analysis of landslide evolution affecting olive groves using UAV and photogrammetric techniques, Remote Sens., 8(10), doi:10.3390/rs8100837, 2016.

Fonstad, M. A., Dietrich, J. T., Courville, B. C., Jensen, J. L. and Carbonneau, P. E.: Topographic structure from motion: a new development in photogrammetric measurement, Earth Surf. Process. Landforms, 38(4), 421–430, doi:10.1002/esp.3366, 2013.

Forlani, G., Dall'Asta, E., Diotri, F., di Cella, U. M., Roncella, R. and Santise, M.: Quality assessment of DSMs produced from UAV flights georeferenced with on-board RTK positioning, Remote Sens., 10(2), doi:10.3390/rs10020311, 2018.

Fox, M., Herman, F., Kissling, E. and Willett, S. D.: Rapid exhumation in the Western Alps driven by slab detachment and glacial erosion, Geology, 43(5), 379–382, doi:10.1130/G36411.1, 2015.

Fressard, M., Maquaire, O., Thiery, Y., Davidson, R. and Lissak, C.: Geomorphology Multi-method characterisation of an active landslide: Case study in the Pays d'Auge plateau (Normandy, France), Geomorphology, 270, 22–39, doi:10.1016/j.geomorph.2016.07.001, 2016.

Fryirs, K.: (Dis)Connectivity in catchment sediment cascades: A fresh look at the sediment delivery problem, Earth Surf. Process. Landforms, 38(1), 30–46, doi:10.1002/esp.3242, 2013.

Fuller, C. W., Willett, S. D., Hovius, N. and Slingerland, R.: Erosion rates for Taiwan Mountain basins: New determinations from suspended sediment records and a stochastic model of their temporal variation, J. Geol., 111(1), 71–87, doi:10.1086/344665, 2003a.

Fuller, I. C. and Marden, M.: Rapid channel response to variability in sediment supply: Cutting and filling of the Tarndale Fan, Waipaoa catchment, New Zealand, Mar. Geol., 270(1–4), 45–54, doi:10.1016/j.margeo.2009.10.004, 2010.

Fuller, I. C., Large, A. R. G. and Milan, D. J.: Quantifying channel development and sediment transfer following chute cutoff in a wandering gravel-bed river, Geomorphology, 54(3–4), 307–323, doi:10.1016/S0169-555X(02)00374-4, 2003b.

Furukawa, Y. and Ponce, J.: Accurate, dense, and robust multiview stereopsis., Inst. Electr. Electron. Eng. Trans. Pattern Anal. Mach. Intell., 32(8), 1362–1376, doi:10.1109/TPAMI.2009.161, 2010.

Gabet, E. J. and Mudd, S. M.: A theoretical model coupling chemical weathering rates with denudation rates, Geology, 37(2), 151–154, doi:10.1130/G25270A.1, 2009.

Gomez, C.: Digital photogrammetry and GIS-based analysis of the bio-geomorphological evolution of Sakurajima Volcano, diachronic analysis from 1947 to 2006, J. Volcanol. Geotherm. Res., 280, 1–13, doi:10.1016/j.jvolgeores.2014.04.015, 2014.

Gosse, J. C. and Phillips, F. M.: Terrestrial in situ cosmogenic nuclides:theory and application, Quat. Sci. Rev., 20, 1475–1560, doi:10.1016/S0277-3791(00)00171-2, 2001.

Gran, K. B. and Czuba, J. A.: Sediment pulse evolution and the role of network structure, Geomorphology, 277, 17–30, doi:10.1016/j.geomorph.2015.12.015, 2017.

Granger, D. E. and Riebe, C. S.: Cosmogenic Nuclides in Weathering and Erosion, in Treatise on Geochemistry, vol. 5, edited by H. D. Holland and K. K. Turekian, Elsevier, Oxford., 2003.

Guns, M. and Vanacker, V.: Shifts in landslide frequency–area distribution after forest conversion in the tropical Andes, Anthropocene, 6, 75–85, doi:10.1016/j.ancene.2014.08.001, 2014.

Guzzetti, F., Malamud, B. D., Turcotte, D. L. and Reichenbach, P.: Power-law correlations of landslide areas in central Italy, Earth Planet. Sci. Lett., 195, 169–183, doi:10.1016/S0012-821X(01)00589-1, 2002.

Guzzetti, F., Reichenbach, P., Cardinali, M., Galli, M. and Ardizzone, F.: Probabilistic landslide hazard assessment at the basin scale, Geomorphology, 72(1–4), 272–299, doi:10.1016/j.geomorph.2005.06.002, 2005.

Hancock, G. R., Coulthard, T. J. and Lowry, J. B. C.: Predicting uncertainty in sediment transport and landscape evolution - the influence of initial surface conditions, Comput. Geosci., 90, 117–130, doi:10.1016/j.cageo.2015.08.014, 2016.

Harvey, A. M.: Coupling between hillslopes and channels in upland fluvial systems: implications for landscape sensitivity, illustrated from the Howgill Fells, northwest England, Catena, (42), 225–250, 2001.

Harwin, S. and Lucieer, A.: Assessing the Accuracy of Georeferenced Point Clouds Produced via Multi-View Stereopsis from Unmanned Aerial Vehicle (UAV) Imagery, Remote Sens., 4(12), 1573–1599, doi:10.3390/rs4061573, 2012.

Heckmann, T. and Schwanghart, W.: Geomorphic coupling and sediment connectivity in an alpine catchment - Exploring sediment cascades using graph theory, Geomorphology, 182, 89–103, doi:10.1016/j.geomorph.2012.10.033, 2013.

Hervás, J., Barredo, J. I., Rosin, P. L., Pasuto, A., Mantovani, F. and Silvano, S.: Monitoring landslides from optical remotely sensed imagery: The case history of Tessina landslide, Italy, Geomorphology, 54(1–2), 63–75, doi:10.1016/S0169-555X(03)00056-4, 2003.

Hinderer, M., Kastowski, M., Kamelger, A., Bartolini, C. and Schlunegger, F.: River loads and modern denudation of the Alps — A review, Earth-Science Rev., 118, 11–44, doi:10.1016/j.earscirev.2013.01.001, 2013.

Horowitz, A. J.: An evaluation of sediment rating curves for estimating suspended sediment concentrations for subsequent flux calculations, Hydrol. Process., 17(17), 3387–3409, doi:10.1002/hyp.1299, 2003.

Hovius, N., Stark, C. P. and Allen, P. A.: Sediment flux from a mountain belt derived by landslide mapping, Geology, 25, 231–234, doi:10.1130/0091-7613(1997)025<0231, 1997.

Hovius, N., Stark, C., Hao-Tsu, C. and Jiun-Chuan, L.: Supply and Removal of Sediment in a Landslide-Dominated Mountain Belt: Central Range, Taiwan., J. Geol., 108(1), 73–89, doi:10.1086/314387, 2000.

Huang, H., Long, J., Lin, H., Zhang, L., Yi, W. and Lei, B.: Unmanned aerial vehicle based remote sensing method for monitoring a steep mountainous slope in the Three Gorges Reservoir, China, Earth Sci. Informatics, 10(3), 287–301, doi:10.1007/s12145-017-0291-9, 2017.

Hugenholtz, C. H., Whitehead, K., Brown, O. W., Barchyn, T. E., Moorman, B. J., LeClair, A., Riddell, K. and Hamilton, T.: Geomorphological mapping with a small unmanned aircraft system (sUAS): Feature detection and accuracy assessment of a photogrammetrically-derived digital terrain model, Geomorphology, 194, 16–24, doi:10.1016/j.geomorph.2013.03.023, 2013.

Huggel, C., Clague, J. J. and Korup, O.: Is climate change responsible for changing landslide activity in high mountains?, Earth Surf. Process. Landforms, 37(1), 77–91, doi:10.1002/esp.2223, 2012.

Hungr, O., Leroueil, S. and Picarelli, L.: The Varnes classification of landslide types, an update, Landslides, 11(2), 167–194, doi:10.1007/s10346-013-0436-y, 2014.

Hurst, M. D., Ellis, M. a., Royse, K. R., Lee, K. a. and Freeborough, K.: Controls on the magnitude-frequency scaling of an inventory of secular landslides, Earth Surf. Dyn., 1(1), 67–78, doi:10.5194/esurf-1-67-2013, 2013.

Immerzeel, W. W., Kraaijenbrink, P. D. a., Shea, J. M., Shrestha, A. B., Pellicciotti, F., Bierkens, M. F. P. and de Jong, S. M.: High-resolution monitoring of Himalayan glacier dynamics using unmanned aerial vehicles, Remote Sens. Environ., 150, 93–103, doi:10.1016/j.rse.2014.04.025, 2014.

Jaboyedoff, M., Oppikofer, T., Abellán, A., Derron, M.-H., Loye, A., Metzger, R. and Pedrazzini, A.: Use of LIDAR in landslide investigations: a review, Nat. Hazards, 61(1), 5–28, doi:10.1007/s11069-010-9634-2, 2012.

James, M. R. and Robson, S.: Straightforward reconstruction of 3D surfaces and topography with a camera: Accuracy and geoscience application, J. Geophys. Res., 117, F03017, doi:10.1029/2011JF002289, 2012.

James, M. R. and Robson, S.: Mitigating systematic error in topographic models derived from UAV and ground-based image networks, Earth Surf. Process. Landforms, 39, 1413–1420, doi:10.1002/esp.3609, 2014.

James, M. R., Robson, S. and Smith, M. W.: 3-D uncertainty-based topographic change detection with structure-from-motion photogrammetry: Precision maps for ground control and directly georeferenced surveys, Earth Surf. Process. Landforms, 1788(March), 1769–1788, doi:10.1002/esp.4125, 2017a.

James, M. R., Robson, S., d'Oleire-Oltmanns, S. and Niethammer, U.: Optimising UAV topographic surveys processed with structure-from-motion: Ground control quality, quantity and bundle adjustment, Geomorphology, 280, 51–66, doi:10.1016/j.geomorph.2016.11.021, 2017b.

Jerolmack, D. J. and Paola, C.: Shredding of environmental signals by sediment transport, Geophys. Res. Lett., 37(19), 1–5, doi:10.1029/2010GL044638, 2010.

Johnson, K., Nissen, E., Saripalli, S., Arrowsmith, J. R., McGarey, P., Scharer, K., Williams, P. and Blisniuk, K.: Rapid mapping of ultrafine fault zone topography with structure from motion, Geosphere, 10(5), 969–986, doi:10.1130/GES01017.1, 2014.

Jonas, T., Marty, C. and Magnusson, J.: Estimating the snow water equivalent from snow depth measurements in the Swiss Alps, J. Hydrol., 378(1–2), 161–167, doi:10.1016/j.jhydrol.2009.09.021, 2009.

Joyce, K. E., Belliss, S. E., Samsonov, S. V., McNeill, S. J. and Glassey, P. J.: A review of the status of satellite remote sensing and image processing techniques for mapping natural hazards and disasters, Prog. Phys. Geogr., 33(2), 183–207, doi:10.1177/0309133309339563, 2009.

Kääb, A.: Monitoring high-mountain terrain deformation from repeated air-and spaceborne optical data: examples using digital aerial imagery and ASTER data, ISPRS J. Photogramm. Remote Sens., 57(1–2), 39–52, doi:10.1016/S0924-2716(02)00114-4, 2002.

Kirchner, J. W., Finkel, R. C., Riebe, C. S., Granger, D. E., Clayton, J. L., King, J. G., Megahan, W. F. and Sites, F.: Mountain erosion over 10 yr, 10 k.y., and 10 m.y. time scales, Geology, 29(7), 591–594, doi:10.1130/0091-7613(2001)029<0591:MEOYKY>2.0.CO;2, 2001.

Kober, F., Hippe, K., Salcher, B., Ivy-Ochs, S., Kubik, P. W., Wacker, L. and Hählen, N.: Debris-flow-dependent variation of cosmogenically derived catchment-wide denudation rates, Geology, 40(10), 935–938, doi:10.1130/G33406.1, 2012.

Korup, O., McSaveney, M. J. and Davies, T. R. .: Sediment generation and delivery from large historic landslides in the Southern Alps, New Zealand, Geomorphology, 61(1–2), 189–207, doi:10.1016/j.geomorph.2004.01.001, 2004.

Korup, O., Densmore, A. L. and Schlunegger, F.: The role of landslides in mountain range evolution, Geomorphology, 120(1–2), 77–90, doi:10.1016/j.geomorph.2009.09.017, 2010.

Lague, D., Brodu, N. and Leroux, J.: Accurate 3D comparison of complex topography with terrestrial laser scanner: Application to the Rangitikei canyon (N-Z), ISPRS J. Photogramm. Remote Sens., 82, 10–26, doi:10.1016/j.isprsjprs.2013.04.009, 2013.

Lal, D.: Cosmic ray labeling of erosion surfaces: in situ nuclide production rates and erosion models, Earth Planet. Sci. Lett., 104(2–4), 424–439, doi:10.1016/0012-821X(91)90220-C, 1991.

Larsen, I. J., Montgomery, D. R. and Greenberg, H. M.: The contribution of mountains to global denudation, Geology, 42(6), 527–530, doi:10.1130/G35136.1, 2014.

Lateltin, O., Haemmig, C., Raetzo, H. and Bonnard, C.: Landslide risk management in Switzerland, Landslides, 2(4), 313–320, doi:10.1007/s10346-005-0018-8, 2005.

Leprince, S., Barbot, S., Ayoub, F. and Avouac, J.: Automatic and precise orthorectification, coregistration, and subpixel correlation of satellite, images, application to ground deformation measurements, IEEE Trans. Geosci. Remote Sens., 45(6), 1529–1558, 2007.

Lopez-Saez, J., Morel, P., Corona, C., Bommer-Denns, B., Schlunegger, F., Berger, F. and Stoffel, M.: Tree-ring reconstruction of reactivation phases of the Schimbrig landslide (Swiss Alps), Géomorphologie Reli. Process. Environ., 23(3), 265–276, doi:10.4000/geomorphologie.11825, 2017.

Lowe, D. G.: Distinctive image features from scale-invariant keypoints, Int. J. Comput. Vis., 60(2), 91–110, doi:10.1023/B:VISI.0000029664.99615.94, 2004.

Lucieer, A., de Jong, S. M. and Turner, D.: Mapping landslide displacements using Structure from Motion (SfM) and image correlation of multi-temporal UAV photography, Prog. Phys. Geogr., 38(1), 97–116, doi:10.1177/0309133313515293, 2014.

Mackey, B. H., Roering, J. J. and McKean, J. a.: Long-term kinematics and sediment flux of an active earthflow, Eel River, California, Geology, 37(9), 803–806, doi:10.1130/G30136A.1, 2009.

Maher, K. and Chamberlain, C. P.: Hydrologic regulation of chemical weathering and the geologic carbon cycle, Science (80-.)., 343(March), 1502–1504, doi:10.1126/science.1250770, 2014.

Malamud, B. D., Turcotte, D. L., Guzzetti, F. and Reichenbach, P.: Landslide inventories and their statistical properties, Earth Surf. Process. Landforms, 29(6), 687–711, doi:10.1002/esp.1064, 2004.

Mancini, F., Dubbini, M., Gattelli, M., Stecchi, F., Fabbri, S. and Gabbianelli, G.: Using Unmanned Aerial Vehicles (UAV) for High-Resolution Reconstruction of Topography: The Structure from Motion Approach on Coastal Environments, Remote Sens., 5(12), 6880–6898, doi:10.3390/rs5126880, 2013.

McKean, J. and Roering, J.: Objective landslide detection and surface morphology mapping using high-resolution airborne laser altimetry, Geomorphology, 57(3–4), 331–351, doi:10.1016/S0169-555X(03)00164-8, 2004.

Merritt, A. J., Chambers, J. E., Murphy, W., Wilkinson, P. B., West, L. J., Gunn, D. A., Meldrum, P. I., Kirkham, M. and Dixon, N.: 3D ground model development for an active landslide in Lias mudrocks using geophysical, remote sensing and geotechnical methods, Landslides, (11), 537–550, doi:10.1007/s10346-013-0409-1, 2014.

Metternicht, G., Hurni, L. and Gogu, R.: Remote sensing of landslides: An analysis of the potential contribution to geo-spatial systems for hazard assessment in mountainous environments, Remote Sens. Environ., 98(2–3), 284–303, doi:10.1016/j.rse.2005.08.004, 2005.

Meunier, P., Hovius, N. and Haines, A. J.: Regional patterns of earthquake-triggered landslides and their relation to ground motion, Geophys. Res. Lett., 34(20), 1–5, doi:10.1029/2007GL031337, 2007.

Montgomery, D. R.: Predicting landscape-scale erosion rates using digital elevation models, Comptes Rendus Geosci., 335(16), 1121–1130, doi:10.1016/j.crte.2003.10.005, 2003.

Montgomery, D. R. and Brandon, M. T.: Topographic controls on erosion rates in tectonically active mountain ranges, Earth Planet. Sci. Lett., 201(3–4), 481–489, doi:10.1016/S0012-821X(02)00725-2, 2002.

Montgomery, D. R., Balco, G. and Willett, S. D.: Climate, tectonics, and the morphology of the Andes, Geology, 29(7), 579–582, doi:10.1130/0091-7613(2001)029<0579:CTATMO>2.0.CO;2, 2001.

Moss, J. L., McGuire, W. J. and Page, D.: Ground deformation monitoring of a potential landslide at La Palma, Canary Islands, J. Volcanol. Geotherm. Res., 94(1–4), 251–265, doi:10.1016/S0377-0273(99)00106-7, 1999.

Mudd, S. M., Harel, M. A., Hurst, M. D., Grieve, S. W. D. and Marrero, S. M.: The CAIRN method: Automated, reproducible calculation of catchment-averaged denudation rates from cosmogenic nuclide concentrations, Earth Surf. Dyn., 4(3), 655–674, doi:10.5194/esurf-4-655-2016, 2016.

Neitzel, F. and Klonowski, J.: Mobile 3D mapping with a low-cost UAV system, Int. Arch. Photogramm. Remote Sens. Spat. Inf. Sci., 38, 1–6, 2011.

Niemi, N. a., Oskin, M., Burbank, D. W., Heimsath, A. M. and Gabet, E. J.: Effects of bedrock landslides on cosmogenically determined erosion rates, Earth Planet. Sci. Lett., 237(3–4), 480–498, doi:10.1016/j.epsl.2005.07.009, 2005.

Niethammer, U., James, M. R., Rothmund, S., Travelletti, J. and Joswig, M.: UAV-based remote sensing of the Super-Sauze landslide: Evaluation and results, Eng. Geol., 128, 2–11, doi:10.1016/j.enggeo.2011.03.012, 2012.

Norton, K. P., von Blanckenburg, F., Schlunegger, F., Schwab, M. and Kubik, P. W.: Cosmogenic nuclide-based investigation of spatial erosion and hillslope channel coupling in the transient foreland of the Swiss Alps, Geomorphology, 95(3–4), 474–486, doi:10.1016/j.geomorph.2007.07.013, 2008.

Notebaert, B., Verstraeten, G., Govers, G. and Poesen, J.: Qualitative and quantitative applications of LiDAR imagery in fluvial geomorphology, Earth Surf. Process. Landforms, 34(August 2008), 217–231, doi:10.1002/esp, 2009.

O'Connor, J., Smith, M. J. and James, M. R.: Cameras and settings for aerial surveys in the geosciences, Prog. Phys. Geogr., 030913331770309, doi:10.1177/0309133317703092, 2017.

Obanawa, H., Hayakawa, Y., Saito, H. and Gomez, C.: Comparison of DSMs derived from UAV-SfM method and terrestrial laser scanning, J. Japan Soc. Photogramm. Remote Sens., 53(2), 67–74, 2014.

Ouédraogo, M. M., Degré, A., Debouche, C. and Lisein, J.: The evaluation of unmanned aerial system-based photogrammetry and terrestrial laser scanning to generate DEMs of agricultural watersheds, Geomorphology, 214, 339–355, doi:10.1016/j.geomorph.2014.02.016, 2014.

Ouimet, W. B., Whipple, K. X. and Granger, D. E.: Beyond threshold hillslopes: Channel adjustment to base-level fall in tectonically active mountain ranges, Geology, 37(7), 579–582, doi:10.1130/G30013A.1, 2009.

Paola, C., Ganti, V., Mohrig, D., Runkel, A. C. and Straub, K. M.: Time Not Our Time: Physical Controls on the Preservation and Measurement of Geologic Time, Annu. Rev. Earth Planet. Sci., 46(1), annurev-earth-082517-010129, doi:10.1146/annurev-earth-082517-010129, 2018.

Parker, R. N., Densmore, A. L., Rosser, N. J., de Michele, M., Li, Y., Huang, R., Whadcoat, S. and Petley, D. N.: Mass wasting triggered by the 2008 Wenchuan earthquake is greater than orogenic growth, Nat. Geosci., 4, 449–452, doi:10.1038/ngeo1154, 2011.

Passalacqua, P., Belmont, P., Staley, D. M., Simley, J. D., Arrowsmith, J. R., Bode, C. A., Crosby, C., DeLong, S. B., Glenn, N. F., Kelly, S. a., Lague, D., Sangireddy, H., Schaffrath, K., Tarboton, D. G., Wasklewicz, T. and Wheaton, J. M.: Analyzing high resolution topography for advancing the understanding of mass and energy transfer through landscapes: A review, Earth-Science Rev., 148, 174–193, doi:10.1016/j.earscirev.2015.05.012, 2015.

Perrone, A., Lapenna, V. and Piscitelli, S.: Earth-Science Reviews Electrical resistivity tomography technique for landslide investigation : A review, Earth Sci. Rev., 135, 65–82, doi:10.1016/j.earscirev.2014.04.002, 2014.

Peternel, T., Kumelj, Š., Oštir, K. and Komac, M.: Monitoring the Potoška planina landslide (NW Slovenia) using UAV photogrammetry and tachymetric measurements, Landslides, 14(1), 395–406, doi:10.1007/s10346-016-0759-6, 2017.

Portenga, E. W. and Bierman, P. R.: Understanding earth's eroding surface with ^{10}Be, GSA Today, 21(8), 4–10, doi:10.1130/G111A.1, 2011.

Prokešová, R., Kardoš, M. and Medveďová, A.: Landslide dynamics from high-resolution aerial photographs: A case study from the Western Carpathians, Slovakia, Geomorphology, 115(1–2), 90–101, doi:10.1016/j.geomorph.2009.09.033, 2010.

Prokešová, R., Kardoš, M., Tábořík, P., Medveďová, A., Stacke, V. and Chudý, F.: Kinematic behaviour of a large earthflow defined by surface displacement monitoring, DEM differencing, and ERT imaging, Geomorphology, 224, 86–101, doi:10.1016/j.geomorph.2014.06.029, 2014.

Raetzo, H., Lateltin, O., Bollinger, D. and Tripet, J. P.: Hazard assessment in Switzerland - Codes of practice for mass movements, Bull. Eng. Geol. Environ., 61(3), 263–268, doi:10.1007/s10064-002-0163-4, 2002.

Raucoules, D., de Michele, M., Malet, J. P. and Ulrich, P.: Time-variable 3D ground displacements from high-resolution synthetic aperture radar (SAR). application to La Valette landslide (South French Alps), Remote Sens. Environ., 139, 198–204, doi:10.1016/j.rse.2013.08.006, 2013.

Reiners, P. W. and Brandon, M. T.: Using Thermochronology To Understand Orogenic Erosion, Annu. Rev. Earth Planet. Sci., 34(1), 419–466, doi:10.1146/annurev.earth.34.031405.125202, 2006.

Riebe, C. S., Sklar, L. S., Lukens, C. E. and Shuster, D. L.: Climate and topography control the size and flux of sediment produced on steep mountain slopes, Proc. Natl. Acad. Sci., 112(51), 201503567, doi:10.1073/pnas.1503567112, 2015.

Rippin, D. M., Pomfret, A. and King, N.: High resolution mapping of supra-glacial drainage pathways reveals link between micro-channel drainage density, surface roughness and surface reflectance, Earth Surf. Process. Landforms, 40(10), 1279–1290, doi:10.1002/esp.3719, 2015.

Roe, G. H., Whipple, K. X. and Fletcher, J. K.: Feedbacks among climate, erosion, and tectonics in a critical wedge orogen, Am. J. Sci., 308(7), 815–842, doi:10.2475/07.2008.01, 2008.

Roering, J. J., Kirchner, J. W. and Dietrich, W. E.: Evidence for nonlinear, diffusive sediment transport on hillslopes and implications for landscape morphology, Water Resour. Res., 35(3), 853–870, doi:10.1029/1998WR900090, 1999.

Roering, J. J., Kirchner, J. W. and Dietrich, W. E.: Hillslope evolution by nonlinear, slope-dependent transport: Steady state morphology and equilibrium adjustment timescales, J. Geophys. Res. Solid Earth, 106(B8), 16499–16513, doi:10.1029/2001JB000323, 2001.

Roering, J. J., Kirchner, J. W. and Dietrich, W. E.: Characterizing structural and lithologic controls on deep-seated landsliding: Implications for topographic relief and landscape evolution in the Oregon Coast Range, USA, Bull. Geol. Soc. Am., 117(5–6), 654–668, doi:10.1130/B25567.1, 2005.

Sadler, P. M.: Sediment accumulation rates and the completeness of stratigraphic sections, J. Geol., 89(5), 569–584, doi:10.1086/628623, 1981.

Sadler, P. M. and Jerolmack, D. J.: Scaling laws for aggradation, denudation and progradation rates: the case for time-scale invariance at sediment sources and sinks, Geol. Soc. London, Spec. Publ., 404(1), 69–88, doi:10.1144/SP404.7, 2015.

Safran, E. B., Bierman, P. R., Aalto, R., Dunne, T., Whipple, K. X. and Caffee, M.: Erosion rates driven by channel network incision in the Bolivian Andes, Earth Surf. Process. Landforms, 30(8), 1007–1024, doi:10.1002/esp.1259, 2005.

Savi, S., Schneuwly-Bollschweiler, M., Bommer-Denns, B., Stoffel, M. and Schlunegger, F.: Geomorphic coupling between hillslopes and channels in the Swiss Alps, Earth Surf. Process. Landforms, 38(9), 959–969, doi:10.1002/esp.3342, 2013.

Savi, S., Norton, K., Picotti, V., Brardinoni, F., Akçar, N., Kubik, P. W., Delunel, R. and Schlunegger, F.: Effects of sediment mixing on ^{10}Be concentrations in the Zielbach catchment, central-eastern Italian Alps, Quat. Geochronol., 19, 148–162, doi:10.1016/j.quageo.2013.01.006, 2014.

Scaioni, M., Longoni, L., Melillo, V. and Papini, M.: Remote -sensing for landslide investigations: An overview of recent achievements and perspectives, Remote Sens., 6(10), 9600–9652, doi:10.3390/rs6109600, 2014.

Schlögel, R., Doubre, C., Malet, J. P. and Masson, F.: Landslide deformation monitoring with ALOS/PALSAR imagery: A D-InSAR geomorphological interpretation method, Geomorphology, 231, 314–330, doi:10.1016/j.geomorph.2014.11.031, 2015.

Schlunegger, F. and Kissling, E.: Slab rollback orogeny in the Alps and evolution of the Swiss Molasse basin, Nat. Commun., 6, 8605, doi:10.1038/ncomms9605, 2015.

Schlunegger, F., Norton, K. P. and Caduff, R.: Hillslope processes in temperate environments, in Treatise on Geomorphology, edited by J. F. Shroder, pp. 337–354, Academia Press, San Diego., 2013.

Schlunegger, F., Jost, J., Grünig, A. and Trüssel, M.: Erläuterungen, Geologischer Atlas der Schweiz, Kartenblatt 1169 Schüpfheim 1:25’000, Bundesamt für Landestopographie swisstopo, 107pp, 2016a.

Schlunegger, F., Anspach, O., Bieri, B., Böning, P., Kaufmann, Y., Lahl, K., Lonschinski, M., Mollet, H., Sachse, D., Schubert, C., Stöckli, G. and Zander, I.: Geologische Karte der Schweiz, Kartenblatt 1169 Schüpfheim 1:25’000, Bundesamt für Landestopographie swisstopo, 2016b.

Schoonejans, J., Vanacker, V., Opfergelt, S., Ameijeiras-Marino, Y. and Christl, M.: Kinetically limited weathering at low denudation rates in semiarid climatic conditions, J. Geophys. Res. Earth Surf., 121, 336-350–18, doi:10.1002/2015JF003626, 2015.

Schumm, S. A. and Lichty, R. W.: Time, space, and causality in geomorphology, Am. J. Sci., 263(2), 110–119, doi:10.2475/ajs.263.2.110, 1965.

Schwab, M., Läderach, C., Rieke-Zapp, D. and Schlunegger, F.: Slip rates variability and sediment mobilization on a shallow landslide in the northern Swiss Alps, Swiss J. Geosci., 100(2), 281–292, doi:10.1007/s00015-007-1218-0, 2007.

Schwab, M., Rieke-Zapp, D., Schneider, H., Liniger, M. and Schlunegger, F.: Landsliding and sediment flux in the Central Swiss Alps: A photogrammetric study of the Schimbrig landslide, Entlebuch, Geomorphology, 97(3–4), 392–406, doi:10.1016/j.geomorph.2007.08.019, 2008.

Seijmonsbergen, A. C.: The modern geomorphological map, in Treatise on Geomorphology, edited by J. F. Shroder, pp. 35–52, Academic Press, San Diego., 2013.

Seneviratne, S. I., Corti, T., Davin, E. L., Hirschi, M., Jaeger, E. B., Lehner, I., Orlowsky, B. and Teuling, A. J.: Investigating soil moisture-climate interactions in a changing climate: A review, Earth-Science Rev., 99(3–4), 125–161, doi:10.1016/j.earscirev.2010.02.004, 2010.

Service Publique de Wallonie: Modèles numériques de surface des lits majeurs des principaux cours d’eau wallons, [online] Available from: http://geoportail.wallonie.be/cms/render/live/fr/sites/geoportail/contents/metadata/plainData/47d7dce7-d401-4aa5-8407-aee0a99eb584.html (Accessed 19 April 2014), 2004.

Sklar, L. S., Riebe, C. S., Marshall, J. A., Genetti, J., Leclere, S., Lukens, C. L. and Merces, V.: The problem of predicting the size distribution of sediment supplied by hillslopes to rivers, Geomorphology, 277, 31–49, doi:10.1016/j.geomorph.2016.05.005, 2017.

Smith, M. W., Carrivick, J. L. and Quincey, D. J.: Structure from motion photogrammetry in physical geography, Prog. Phys. Geogr., 40(2), 247–275, doi:10.1177/0309133315615805, 2015.

Snavely, N., Seitz, S. M. and Szeliski, R.: Photo tourism: Exploring Photo Collections in 3D, ACM Trans. Graph., 25(3), 835–846, doi:10.1145/1141911.1141964, 2006.

Snavely, N., Seitz, S. M. and Szeliski, R.: Modeling the World from Internet Photo

Collections, Int. J. Comput. Vis., 80(2), 189–210, doi:10.1007/s11263-007-0107-3, 2008.

Squarzoni, C., Delacourt, C. and Allemand, P.: Differential single-frequency GPS monitoring of the La Valette landslide (French Alps), Eng. Geol., 79(3–4), 215–229, doi:10.1016/j.enggeo.2005.01.015, 2005.

Stark, C. P. and Hovius, N.: The characterization of landslide size distribution, Geophys. Res. Lett., 28(6), 1091–1094, 2001.

Stöcker, C., Nex, F. and Gerke, M.: Quality assessment of combined IMU/GNSS data for direct georeferencing in the context of UAV-based mapping, Int. Arch. Photogramm. Remote Sens. Spat. Inf. Sci., XLII-2/W6(August), 4–7, doi:10.5194/isprs-archives-XLII-2-W6-355-2017, 2017a.

Stöcker, C., Bennett, R., Nex, F., Gerke, M. and Zevenbergen, J.: Review of the current state of UAV regulations, Remote Sens., 9(5), 33–35, doi:10.3390/rs9050459, 2017b.

Stumpf, A., Malet, J.-P., Allemand, P., Pierrot-Deseilligny, M. and Skupinski, G.: Ground-based multi-view photogrammetry for the monitoring of landslide deformation and erosion, Geomorphology, 231, 130–145, doi:10.1016/j.geomorph.2014.10.039, 2014.

Stumpf, A., Malet, J. P. and Delacourt, C.: Correlation of satellite image time-series for the detection and monitoring of slow-moving landslides, Remote Sens. Environ., 189, 40–55, doi:10.1016/j.rse.2016.11.007, 2017.

Sutherland, D. G., Ball, M. H., Hilton, S. J. and Lisle, T. E.: Evolution of a landslide-induced sediment wave in the Navarro River, California, Bull. Geol. Soc. Am., 114(8), 1036–1048, doi:10.1130/0016-7606(2002)114<1036:EOALIS>2.0.CO;2, 2002.

Tanteri, L., Rossi, G., Tofani, V., Vannocci, P., Moretti, S. and Casagli, N.: Multitemporal UAV Survey for Mass Movement Detection and Monitoring, in Advancing Culture of Living with Landslides: Volume 2 Advances in Landslide Science, edited by M. Mikos, B. Tiwari, Y. Yin, and K. Sassa, pp. 153–161, Springer International Publishing, Cham., 2017.

Tarolli, P.: High-resolution topography for understanding Earth surface processes: Opportunities and challenges, Geomorphology, 216, 295–312, doi:10.1016/j.geomorph.2014.03.008, 2014.

Tenorio, G. E., Vanacker, V., Campforts, B., Álvarez, L., Zhiminaicela, S., Vercruysse, K., Molina, A. and Govers, G.: Tracking spatial variation in river load from Andean highlands to inter-Andean valleys, Geomorphology, 308, 175–189, doi:10.1016/j.geomorph.2018.02.009, 2018.

Tonkin, T. N., Midgley, N. G., Graham, D. J. and Labadz, J. C.: The potential of small unmanned aircraft systems and structure-from-motion for topographic surveys: A test of emerging integrated approaches at Cwm Idwal, North Wales, Geomorphology, 226, 35–43, doi:10.1016/j.geomorph.2014.07.021, 2014.

Travelletti, J., Oppikofer, T., Delacourt, C., Malet, J. and Jaboyedoff, M.: Monitoring landslide displacements during a controlled rain experiment using a long-range terrestrial laser scanning (TLS), Int. Arch. Photogramm. Remote Sens. Spat. Inf. Sci., 37(July), 485–490, 2008.

Travelletti, J., Malet, J.-P. and Delacourt, C.: Image-based correlation of Laser Scanning point cloud time series for landslide monitoring, Int. J. Appl. Earth Obs. Geoinf., 32(0), 1–18, doi:10.1016/j.jag.2014.03.022, 2014.

Tucker, G. E. and Hancock, G. R.: Modelling landscape evolution, Earth Surf. Process. Landforms, 35, 28–50, doi:10.1002/esp.1952, 2010.

Turner, D., Lucieer, A. and Watson, C.: An Automated Technique for Generating Georectified Mosaics from Ultra-High Resolution Unmanned Aerial Vehicle (UAV) Imagery, Based on Structure from Motion (SfM) Point Clouds, Remote Sens., 4(12), 1392–1410, doi:10.3390/rs4051392, 2012.

Turner, D., Lucieer, A. and de Jong, S. M.: Time series analysis of landslide dynamics using an Unmanned Aerial Vehicle (UAV), Remote Sens., 7(2), 1736–1757, doi:10.3390/rs70201736, 2015.

Turowski, J. M. and Cook, K. L.: Field techniques for measuring bedrock erosion and denudation, Earth Surf. Process. Landforms, 42(1), 109–127, doi:10.1002/esp.4007, 2017.

Vanacker, V., Vanderschaeghe, M., Govers, G., Willems, E., Poesen, J., Deckers, J. and De Bievre, B.: Linking hydrological, infinite slope stability and land-use change models through GIS for assessing the impact of deforestation on slope stability in high Andean watersheds, Geomorphology, 52(3–4), 299–315, doi:10.1016/S0169-555X(02)00263-5, 2003.

Vanacker, V., von Blanckenburg, F., Hewawasam, T. and Kubik, P. W.: Constraining landscape development of the Sri Lankan escarpment with cosmogenic nuclides in river sediment, Earth Planet. Sci. Lett., 253(3–4), 402–414, doi:10.1016/j.epsl.2006.11.003, 2007.

Vanacker, V., von Blanckenburg, F., Govers, G., Molina, A., Campforts, B. and Kubik, P. W.: Transient river response, captured by channel steepness and its concavity, Geomorphology, 228, 234–243, doi:10.1016/j.geomorph.2014.09.013, 2015.

Vanmaercke, M., Poesen, J., Verstraeten, G., de Vente, J. and Ocakoglu, F.: Sediment yield in Europe: Spatial patterns and scale dependency, Geomorphology, 130(3–4), 142–161, doi:10.1016/j.geomorph.2011.03.010, 2011.

Varnes, D. J.: Slope Movement Types and Processes, Transp. Res. Board Spec. Rep., (176), 11–33, doi:In Special report 176: Landslides: Analysis and Control, Transportation Research Board, Washington, D.C., 1978.

Vassallo, R., Ritz, J. F. and Carretier, S.: Control of geomorphic processes on ^{10}Be concentrations in individual clasts: Complexity of the exposure history in Gobi-Altay range (Mongolia), Geomorphology, 135(1–2), 35–47, doi:10.1016/j.geomorph.2011.07.023, 2011.

Ventura, G., Vilardo, G., Terranova, C. and Sessa, E. B.: Tracking and evolution of complex active landslides by multi-temporal airborne LiDAR data: The Montaguto landslide (Southern Italy), Remote Sens. Environ., 115(12), 3237–3248, doi:10.1016/j.rse.2011.07.007, 2011.

Walling, D. E.: The sediment delivery problem, J. Hydrol., 65(1–3), 209–237, doi:10.1016/0022-1694(83)90217-2, 1983.

Wang, J., Jin, Z., Hilton, R. G., Zhang, F., Densmore, A. L., Li, G. and West, A. J.: Controls on fluvial evacuation of sediment from earthquake-triggered landslide, Geology, 43(February), 115–118, doi:10.1130/G36157.1, 2015.

Wang, W., Godard, V., Liu-Zeng, J., Scherler, D., Xu, C., Zhang, J., Xie, K., Bellier, O., Ansberque, C., de Sigoyer, J. and Team, A.: Perturbation of fluvial sediment fluxes following the 2008 Wenchuan earthquake, Earth Surf. Process. Landforms, 42(15), 2611–2622, doi:10.1002/esp.4210, 2017.

West, A. J., Hetzel, R., Li, G., Jin, Z., Zhang, F., Hilton, R. G. and Densmore, A. L.: Dilution of ^{10}Be in detrital quartz by earthquake-induced landslides: Implications for determining denudation rates and potential to provide insights into landslide sediment dynamics, Earth Planet. Sci. Lett., 396, 143–153, doi:10.1016/j.epsl.2014.03.058, 2014.

Van den Berg, F., Schlunegger, F., Akçar, N. and Kubik, P.: ^{10}Be-derived assessment of accelerated erosion in a glacially conditioned inner gorge, Entlebuch, Central Alps of Switzerland, Earth Surf. Process. Landforms, 37(11), 1176–1188, doi:10.1002/esp.3237, 2012.

van Westen, C. J. and Lulie Getahun, F.: Analyzing the evolution of the Tessina landslide using aerial photographs and digital elevation models, Geomorphology, 54(1–2), 77–89, doi:10.1016/S0169-555X(03)00057-6, 2003.

von Blanckenburg, F.: The control mechanisms of erosion and weathering at basin scale from cosmogenic nuclides in river sediment, Earth Planet. Sci. Lett., 237(3–4), 462–479, doi:10.1016/j.epsl.2005.06.030, 2005.

Westoby, M. J., Brasington, J., Glasser, N. F., Hambrey, M. J. and Reynolds, J. M.: 'Structure-from-Motion' photogrammetry: A low-cost, effective tool for geoscience applications, Geomorphology, 179, 300–314, doi:10.1016/j.geomorph.2012.08.021, 2012.

Wheaton, J. M., Brasington, J., Darby, S. E. and Sear, D. a.: Accounting for uncertainty in DEMs from repeat topographic surveys: improved sediment budgets, Earth Surf. Process. Landforms, 35, 136–156, doi:10.1002/esp.1886, 2010.

Whipple, K. X. and Tucker, G. E.: Dynamics of the stream-power river incision model: Implications for height limits of mountain ranges, landscape response timescales, and research needs, J. Geophys. Res., 104(B8), 17661–17674, doi:10.1029/1999JB900120, 1999.

Whipple, K. X., Hancock, G. S. and Anderson, R. S.: River incision into bedrock: Mechanics and relative efficacy of plucking, abrasion, and cavitation, Bull. Geol. Soc. Am., 112(3), 490–503, doi:10.1130/0016-7606(2000)112<490:RIIBMA>2.0.CO;2, 2000.

Willenbring, J. K. and von Blanckenburg, F.: Long-term stability of global erosion rates and weathering during late-Cenozoic cooling, Nature, 465(7295), 211–214, doi:10.1038/nature09044, 2010.

Wittmann, H., von Blanckenburg, F., Kruesmann, T., Norton, K. P. and Kubik, P. W.: Relation between rock uplift and denudation from cosmogenic nuclides in river sediment in the Central Alps of Switzerland, J. Geophys. Res. Earth Surf., 112(4), 1–20, doi:10.1029/2006JF000729, 2007.

Wu, C.: SiftGPU: A GPU implementation of Scale Invariant Feature Transform (SIFT), [online] Available from: http://cs.unc.edu/~ccwu/siftgpu/ (Accessed 20 April 2014), 2007.

Wu, C.: VisualSFM: A visual Structure from Motion system, [online] Available from: http://ccwu.me/vsfm/ (Accessed 20 April 2014), 2011.

Wu, C.: Towards linear-time incremental Structure from Motion, 2013 Int. Conf. 3D Vis., 127–134, doi:10.1109/3DV.2013.25, 2013.

Wu, C., Agarwal, S., Curless, B. and Seitz, S. M.: Multicore bundle adjustment, in Institute of Electrical and Electronics Engineers Computer Vision and Pattern Recognition., 2011.

Yanites, B. J., Tucker, G. E. and Anderson, R. S.: Numerical and analytical models of cosmogenic radionuclide dynamics in landslide-dominated drainage basins, J. Geophys. Res. Earth Surf., 114(1), doi:10.1029/2008JF001088, 2009.

LIST OF FIGURES

LIST OF TABLES